The role of wind waves and sea spray in air–sea interaction

Proefschrift

ter verkrijging van de graad van doctor
aan de Technische Universiteit Delft,
op gezag van de Rector Magnificus prof.dr.ir. J.T. Fokkema,
voorzitter van het College voor Promoties,
in het openbaar te verdedigen

op maandag 13 mei 2002 om 16:00 uur

door

Jan Fokke MEIRINK

wiskundig ingenieur
geboren te Hallum

Dit proefschrift is goedgekeurd door de promotor:
Prof.dr.ir. J.A. Battjes

Samenstelling promotiecommissie:

Rector Magnificus, voorzitter
Prof.dr.ir. J.A. Battjes, Technische Universiteit Delft, promotor
Prof.dr.ir. A.A.M. Holtslag, Wageningen Universiteit
Prof.dr. G.J. Komen, Universiteit Utrecht
Prof.dr.ir. F.T.M. Nieuwstadt, Technische Universiteit Delft
Prof.dr. S.S. Zilitinkevich, Universiteit Uppsala, Zweden
Dr. A.M.J. van Eijk, TNO-FEL, Den Haag
Dr. V.K. Makin, KNMI, De Bilt

Contents

Contents

Contents

Chapter 1

General introduction

1.1   Air–sea interaction

Near the interface of the atmosphere and the oceans, many interesting processes take place. Air–sea interaction involves those processes that influence the transport of momentum, heat, moisture, gaseous chemicals and aerosols across the air–sea interface (Geernaert 1999). Examples are the forcing of surface waves by the wind, turbulent transport, evaporation, bursting of air bubbles with associated gas transports and formation of sea spray.

Since the oceans cover more than 70% of the Earth's surface, it is worthwile to study subjects related to air–sea interaction. Such studies have various applications. Environmental issues such as climate change have brought a demand for improved performance of climate models. Within those (normally coupled ocean–atmosphere) models a correct representation of exchanges (e.g., of CO_2) between atmospheres and oceans is crucial. A second application is in routine weather and wave forecasts. For weather prediction models, the boundary conditions above waters need to be specified. In wave models an accurate description of the energy input due to the wind is needed. Finally, there are many commercial interests, for example: offshore wind energy production, ship routing, design of offshore platforms and support of defensive operations.

In this work some aspects of air–sea interaction are investigated using numerical models. First, we focus on wind–wave momentum exchange. The wind experiences resistance due to the waves, while the waves grow due to the wind. In the second part, attention is given to heat and moisture exchange and, in particular, to the role of sea spray therein. In storm conditions spray has the potential to attribute to the sea–air fluxes. The consequences of this for numerical weather prediction are investigated at the end of this thesis.

1.2   Exchange of momentum

When air flows over a surface, it is slowed down. In the case of a water surface, the air loses momentum to the water, or, in other words, the atmosphere feels a drag force from the water. For a fixed and flat surface the magnitude of the drag is well known. However, a water surface is not fixed and flat but is covered with waves. At sea, we find waves with widely varying lengths. These waves form an additional resistance to the air flowing over them. On the other hand, the waves grow due to the wind. Hence, a loop of wind and waves influencing each other is created, resulting in a strongly coupled system formed by the atmosphere and the waves (see, e.g., Makin et al. 1995). Mostly because of this complex coupling, there is still considerable uncertainty in estimates of the air–sea momentum exchange coefficient, or drag coefficient. From the large amount of experimental work on measuring the drag over the sea, figure 1.1 shows some of the obtained relations between the drag coefficient and the wind speed. It is likely that the drag coefficient does not only depend on the wind speed, but also on the characteristics of the sea surface, reflected, for example, by the wave age (Maat et al. 1991).
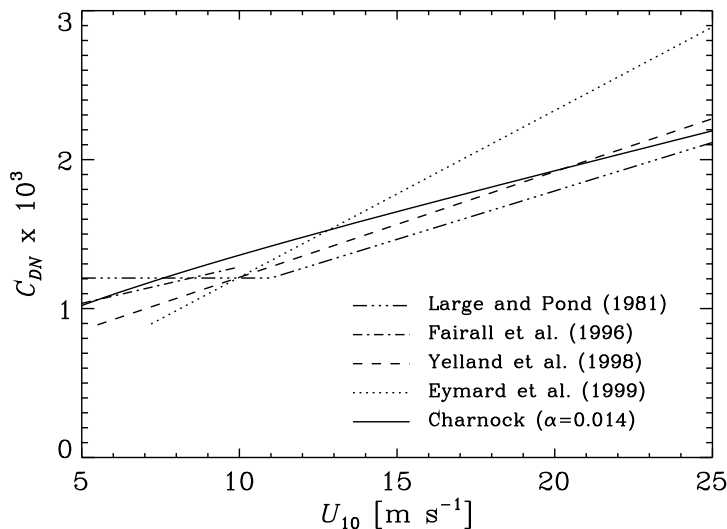
Figure 1.1: Wind speed dependence of the neutral drag coefficient C_{DN}. Experimental fits by Large and Pond (1981), Fairall et al. (1996), Yelland et al. (1998), and Eymard et al. (1999) are shown together with the Charnock relation (Charnock 1955, $\alpha = 0.014$).

The coupled system of wind and waves contains many interactions. Apart from

the fact that waves grow due to the wind, they dissipate due to breaking, and wave components with different lengths interact with each other (Komen et al. 1994). Breaking waves are known to give rise to additional drag (Banner 1990; Kudryavtsev and Makin 2001). Longer waves modulate the air flow and can, indirectly, affect the growth of shorter waves. In turn, these shorter waves determine the roughness of the longer waves, and, thus, influence their growth (Kudryavtsev and Makin 2002).

It is useful to study the different processes in isolation. Many studies have been dedicated to describing the idealized case of the air flow over monochromatic water waves and inferring the energy input of the wind to the waves.

1.2.1 Wave growth
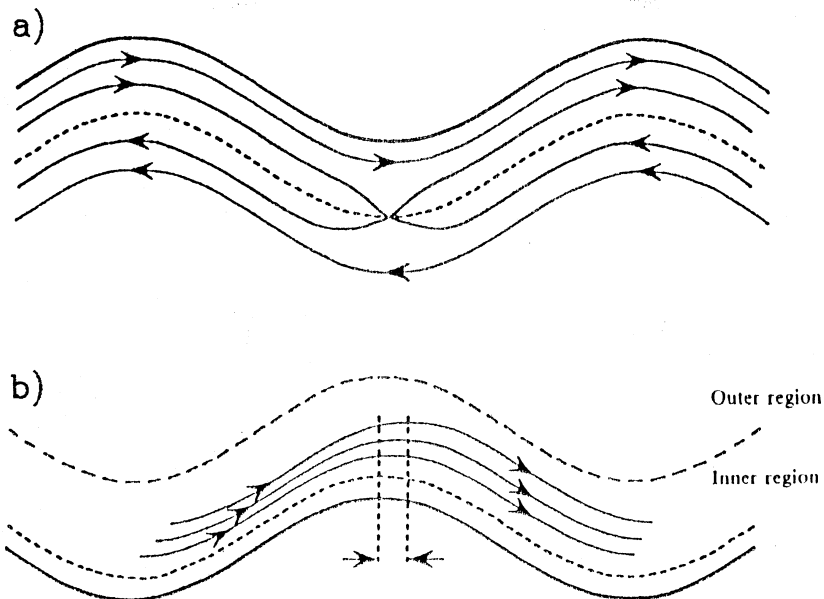
Figure 1.2: Mechanisms for the growth of water waves: (a) the critical-layer mechanism, and (b) the non-separated sheltering mechanism. The short-dashed curves show the critical height, the long-dashed curve in panel b shows the top of the inner region, and the solid lines with arrows are streamlines in a frame of reference in which the wave is steady. From Belcher and Hunt (1993).

Over the years, several mechanisms of wave growth have been proposed in the literature. Jeffreys (1925) assumed that separation of the air flow in the lee of the

wave crest was responsible for the growth. This sheltering hypothesis fails to explain the observed growth rates and, moreover, does not explain the growth of small-amplitude waves, over which no separation takes place. Miles (1957) proposed the so-called critical-layer mechanism (figure 1.2a). At some height above the water surface, the critical height, the wind speed equals the phase velocity of the wave. Singularity of the governing equations of the air flow at this height leads to a phase shift of the pressure, which is responsible for wave growth. A serious assumption in this theory is that the turbulence in the air is not affected by the presence of water waves. When, starting with Townsend (1972), turbulence was taken into account, the critical-layer mechanism was found to be considerably suppressed. Instead, another mechanism was found to be important: the non-separated sheltering (e.g., Belcher and Hunt 1993). Turbulent stresses in the air flow cause a downwind displacement of streamlines (figure 1.2b). This implies a thickening of the boundary layer on the leeside of the wave crest, which leads to the pressure asymmetry required for growth of the waves. The sheltering mechanism is now believed to be the most important cause of growth, while the Miles mechanism supposedly adds to this in certain flow regimes (Belcher and Hunt 1998).

Theoretical and numerical models with turbulence closures of increasing complexity have been used to describe the wave-induced motions in the air flow. Examples of theoretical studies are Jacobs (1987) and Van Duin and Janssen (1992), while numerical investigations include Townsend (1972), Gent and Taylor (1976), Chalikov (1978), and Mastenbroek et al. (1996). Those studies have confirmed the importance of wave-induced turbulence for generating wave growth. They have also made clear that the predicted growth rates depend crucially on the turbulence closure schemes that are employed. A theoretical explanation for this feature was given by Belcher and Hunt (1993), in analogy with the flow over hills (Hunt et al. 1988). They argued that rapid distortion of turbulence at some distance from the wavy surface confines the effects of wave-induced turbulence to a thin layer near the water surface. Experimental evidence for this rapid distortion of turbulence was presented by Mastenbroek et al. (1996).

1.3   Exchange of heat and moisture

In the previous section it was noted that there is still considerable uncertainty concerning the drag over the sea. However, a general feature is clearly visible in figure 1.1, namely the increase of the drag coefficient with wind speed. Intuitively, this can be easily understood: stronger winds cause higher waves which, in turn, form a higher resistance to the air flow. The Charnock relation gives an, at least qualitatively, good description of the general wind-speed dependence.
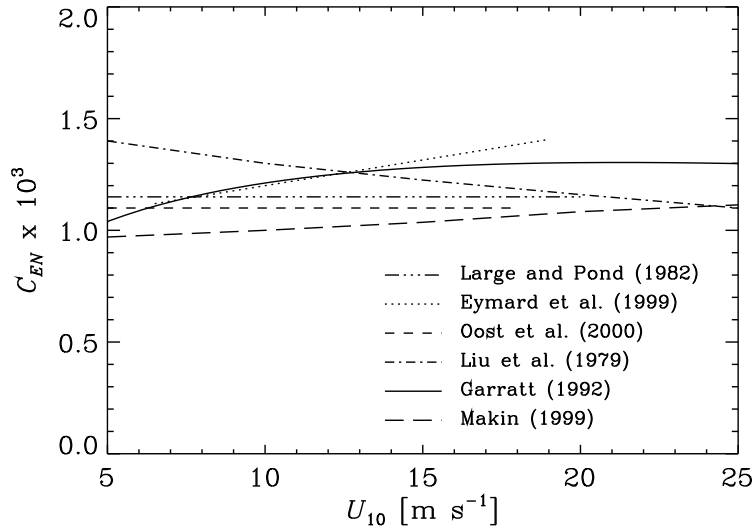
Figure 1.3: Wind speed dependence of the neutral exchange coefficient for moisture C_{EN}. Experimental fits by Large and Pond (1982), Eymard et al. (1999), and Oost et al. (2000) are shown together with theoretical parameterizations by Liu et al. (1979), Garratt (1992), and Makin (1999). The fits and parameterizations shown here are all for unstable conditions.

For the exchange of heat and moisture, the situation appears to be different. The general finding is that the exchange coefficients for heat and moisture hardly depend on the wind speed, as is illustrated in figure 1.3. The underlying reason for this is that the form-drag mechanism, by which momentum is exchanged, is not present for heat and moisture transport. In other words, the presence of waves has only a small effect on this transport.

Nevertheless, waves can have an indirect influence. From wind speeds of $4 \, \mathrm{m \, s^{-1}}$ on, they start to break. With the breaking, sea spray droplets are ejected into the air. Once airborne, the droplets adjust to the ambient atmospheric humidity by evaporation (or condensation), which implies a source (sink) of water vapour, and a sink (source) of sensible heat for the atmosphere. In this way, sea spray may provide an efficient way to influence the balance of heat and moisture over the sea.

1.3.1 Sea spray

Sea spray droplets are generated by different mechanisms, as is illustrated in figure 1.4. The first way is indirect generation via air bubbles (Blanchard 1963). Wave-
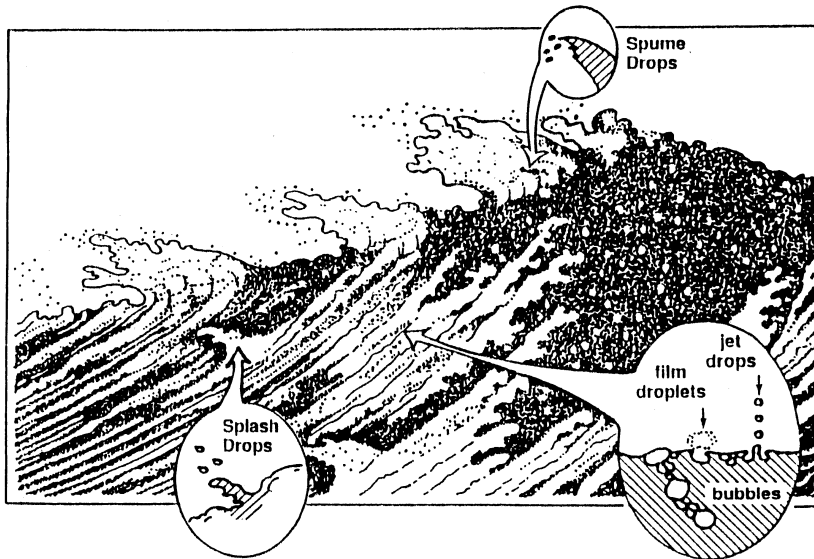
Figure 1.4: Mechanisms for the generation of sea spray. From Andreas et al. (1995).

breaking causes entrainment of air. The resulting bubbles rise into a whitecap and eject droplets into the air. Normally, many film droplets, with typical radii $r < 5 \, \mu$m, and also a few jet droplets ($3 < r < 20 \, \mu$m, typically), are produced from a bursting bubble. Droplets are also formed when wave crests curl over. The associated type is called splash droplets. Finally, spume droplets result from the tearing of droplets from the crests of steep waves by the wind. For this production mechanism the wind speed threshold is around 7–11 m s^{-1}. Splash and spume droplets usually have radii larger than 20 μm (Monahan et al. 1986). Whereas the mechanisms by which droplets are produced are well known, the amount of droplets and their spectral distribution is uncertain. Andreas (1998) collected production functions presented in the literature and showed that the various estimates differ by several orders of magnitudes. What seems to be reasonably known is that the larger part of the spray volume flux is carried by droplets in the range $10 < r < 300 \, \mu$m. It is also certain that the production rate increases very strongly with wind speed.

   After ejection, the spray droplets start to adjust from the conditions at the ocean surface to those in the ambient air. Although most of the larger droplets quickly fall back into the water, the smaller ones can evaporate a substantial part of their

mass until almost-dry salt particles remain. Turbulence can transport these particles upward, where they are a source of cloud condensation nuclei (Blanchard 1969). Hence, by regulating the formation of marine clouds, they may have an important effect on global warming (Latham and Smith 1990). Sea-salt aerosols further play an important role by affecting the electro–optical propagation conditions of the atmosphere. They scatter and absorb radiation and thereby reduce the range of electro-optical surveillance systems (Gathman and Van Eijk 1998). Finally, as was already mentioned, sea spray droplets have the potential to influence the heat and moisture budgets over the ocean, which is what we are interested in in the present thesis.

Spray droplets form elevated sources and sinks of heat and moisture in the marine surface boundary layer. By evaporation, the droplets cool and moisten the air in a layer typically of the order of ten meters. This, in turn, counteracts both direct evaporation from the surface and further evaporation of spray. The surface layer with spray is thus characterized by complicated negative feedbacks. The net effect of spray on the heat budget is then determined by the amount of spray production in combination with the fraction that evaporates, taking into account the feedbacks.

1.4 Goals and modelling approach

Two main aims of the present study are to investigate and develop models for:

- the air flow over waves and the consequential growth of the waves, and

- the effect of evaporating sea spray on the heat budget of the marine boundary layer and the role of the air flow therein.

As was noted before, waves play an important role in air–sea interaction by extracting momentum from the atmosphere. Sea spray is potentially important by contributing to air–sea heat exchange. Hence, modelling wind waves and spray gives the possibility to improve parameterizations of the air-sea fluxes, which serve as boundary (or coupling) conditions in weather and climate models. This brings us to the overall goal of this thesis: to investigate

- the impact of evaporating sea spray in numerical weather prediction.

It will be clear that we have to deal with many different physical processes on various scales. To study these processes, a hierarchy of models is used. After study of a certain process with a detailed model, it is attempted to identify the essential aspects and to make these into a simplified model or a parameterization, which can then be used for applied studies on, normally, larger scales. This approach is termed a multi-scale model approach. Figure 1.5 gives an overview.
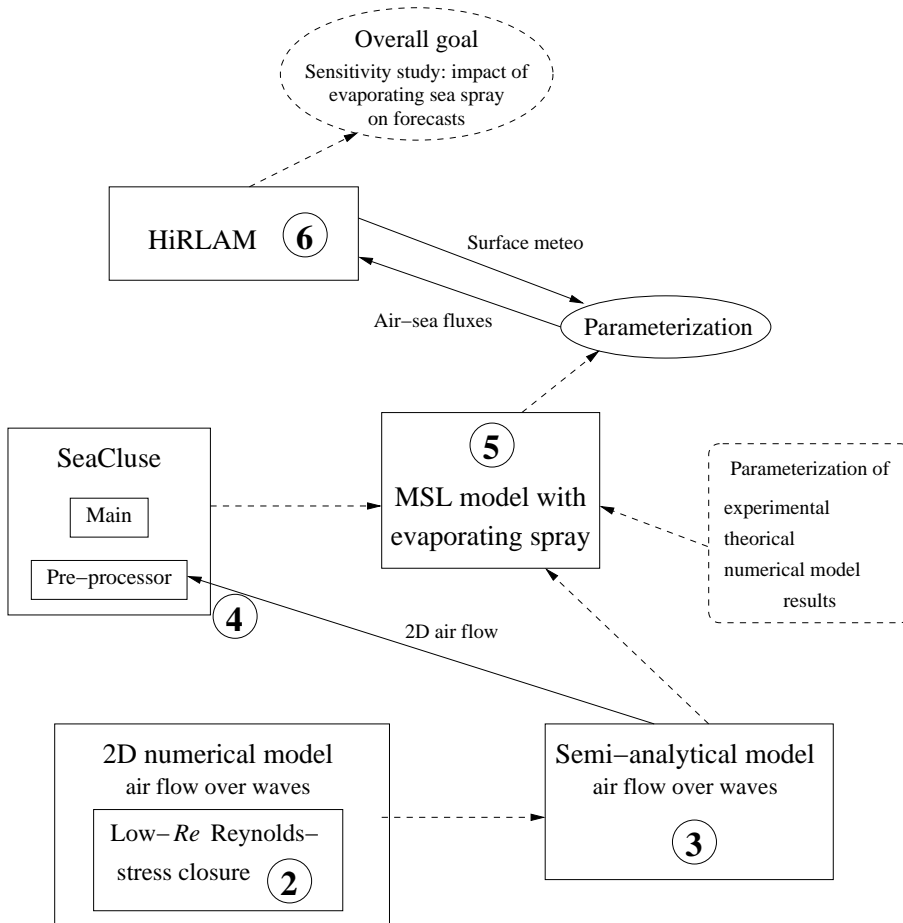
Figure 1.5: Box diagram of the various models used in this thesis and their interrelations. Squared blocks denote models; encircled numbers refer to chapters of this thesis; solid arrows are related to concrete input into models; dashed arrows reflect transfer of knowledge or use of results.

We start with a two-dimensional numerical model of the air flow over water waves, which was originally developed by Chalikov (1978). After a long series of improvements, starting from Makin (1979), Mastenbroek et al. (1996) extended it with a second-order Reynolds-stress turbulence closure scheme. They made detailed comparisons with laboratory observations and concluded that the model was capable of capturing the most important features of the flow over waves. However, the predicted growth rates are consistently lower than those measured both in the laboratory and in the field. A possible reason for this discrepancy is that dynamic effects of viscosity near the water surface are neglected. Such effects may become important at low Reynolds numbers, thus, in particular for short waves. Therefore, the model is adjusted to take into account low Reynolds numbers. Results are presented in chapter 2, which is based on Meirink and Makin (2000).

As was mentioned before, the wave boundary layer is characterized by rapid distortion of turbulence above a certain distance from the water surface. In chapter 3, we present a semi-analytical model that uses this basic feature to give a simplified description of the air flow over waves. The semi-analytical model was published as Kudryavtsev et al. (2001), while a generalization for the case of arbitrary angles between wind and waves has been submitted (Meirink et al. 2002).

Then the attention is turned to sea spray. Chapter 4 gives a detailed review of existing knowledge on sea spray, both from experiments and from models. Some important unresolved issues in the field are stated. One of these is the effect of modifications to the air flow induced by the waves on the transport of spray droplets. This is investigated by applying the wind field predicted by the semi-analytical model in the spray model SeaCluse (Mestayer et al. 1996).

For estimating effects of spray in numerical weather prediction, a simplified model of air–sea heat exchange in the presence of evaporating spray droplets is needed. Such a model was developed by Makin (1998). In this model of the marine surface boundary layer, an equilibrium vertical distribution of sea spray, based on empirical knowledge is imposed. Clearly, this greatly reduces the computational costs. In chapter 5, the model is outlined and extended to describe the characteristics of droplet evaporation more realistically. The model particularly allows to investigate the interactions between the evaporating droplets and the vertical structure of the atmospheric surface layer. The results are compared with the bulk parameterization of the contribution of spray to the air–sea heat fluxes by Fairall et al. (1994) (see the oval box 'Parameterization' in figure 1.5). The latter is extremely useful for applications since it has a negligible calculation time.

In chapter 6, the bulk parameterization is included in the numerical weather prediction (NWP) model HiRLAM, which is used to make the operational weather forecasts at KNMI. Two case studies of intense midlatitude storms are presented,

in which the impact of spray on the forecasts is analyzed. The work described in this chapter was published as Meirink and Makin (2001).

Finally, the thesis is summarized in chapter 7, which also includes some recommendations for future work.

Chapter 2

Numerical modelling of low-Reynolds-number effects in the turbulent air flow over water waves

Since the pioneering work by Miles (1957), the air flow over water waves and the consequential growth of the waves have been a permanent subject of investigation. In the general introduction an overview of the literature on this subject was given. It was argued that correctly modelling turbulence is of crucial importance in order to predict the modification of the air flow due to waves. However, while more and more advanced models were applied to the problem, the predicted growth rates remained consistently lower than indicated by measurements (Mastenbroek et al. 1996; Belcher and Hunt 1998). In this chapter, we investigate a potential cause of this discrepancy, namely the effects of viscosity close to the water surface.

2.1 Introduction

Observed growth rates from many experiments were compiled by Plant (1982) and plotted as a function of c/u_*, where c is the phase velocity of the wave and u_* the friction velocity of the air flow. Considerable scatter is present, which suggests that other parameters may be necessary to explain variations in the growth rate. Such a parameter, which has received little attention so far, is the Reynolds number, $Re = u_*\lambda/\nu$ (here λ is the wavelength and ν the kinematic viscosity of the air). In most studies it is assumed that Re is high enough that dynamic effects of viscosity can

be neglected. However, this assumption breaks down for short waves or low wind speeds.

The purpose of the present chapter is to investigate numerically the influence of the Reynolds number on the structure of the air flow over water waves. This impact is not only important for a proper interpretation of laboratory experiments, but also in the field the assumption that *Re* is high is sometimes violated, as was concluded in an analysis by Harris et al. (1996) of experiments by Snyder et al. (1981). Furthermore, *Re* is especially low for short waves, which are always present on the sea surface. They support a large part of the momentum flux from the atmosphere to the sea (Makin et al. 1995) and are important for remote sensing applications.

In numerical simulations of the air flow above waves, the choice of the turbulence closure scheme is crucial. Belcher and Hunt (1993) applied the theory of rapid distortion of turbulence to the description of the flow over hills and waves. From their work, it follows that turbulence closures based on an eddy-viscosity concept overestimate stress perturbations in the so-called outer region of the flow. Mastenbroek et al. (1996) confirmed this by comparing numerical results from different turbulence models with laboratory observations. They recommended the use of a second-order Reynolds stress closure.

A numerical study taking into account viscous effects was carried out by Harris et al. (1996). They used a linear model with an *e*-ε turbulence closure and performed calculations for both coupled and uncoupled air–water flow. The eddy viscosity was damped in the outer region to avoid overestimation of the stress perturbations. Simulating the flow over hills they found that the form drag increases considerably when *Re* drops below 2×10^4.

In this work we solve full nonlinear equations for the air flow and employ a low-*Re* second-order turbulence closure scheme (Craft and Launder 1996). The numerical model is thought to be general enough to describe the important features of the air flow. In comparison with Harris et al. (1996) our approach has the advantage that no artificial adjustments to the model have to be made. The model computations are compared with laboratory observations of wave-induced velocity profiles performed by Stewart (1970). This experiment is particularly interesting in the context of the present investigation because it was conducted at low Reynolds numbers and covered a wide range of wind-to-wave-speed ratios. The model performance is assessed relative to the high-*Re* model by Mastenbroek et al. (1996). Predictions of the growth rate are compared with experiments, analytical theories and other numerical models. It is concluded that viscous effects are important when $Re < 10^4$ and lead to enhanced wave growth.

2.2   Formulation of the problem

The flow of air over a train of monochromatic water waves is investigated. The waves, propagating in the x_1-direction, give a surface elevation η, which is assumed to be

$$\eta(x_1, x_2, t) = a\cos(kx_1 - \omega t), \tag{2.1}$$

where a is the amplitude of the wave, ω is the angular frequency of the wave, k is the wavenumber and t is time. Since the water surface is taken to be invariant under translations in the x_2-direction, the remaining problem is two-dimensional. For a wave in deep water the dispersion relation gives

$$\omega^2 = gk + \frac{\gamma}{\rho_w}k^3, \tag{2.2}$$

where g is the acceleration due to gravity, γ the surface tension of water, and ρ_w the density of water.

The air flow is considered to be incompressible and neutrally stratified. It is governed by the Reynolds-averaged Navier–Stokes equations:

$$\frac{\partial \bar{u}_j}{\partial x_j} = 0, \tag{2.3}$$

$$\frac{\partial \bar{u}_i}{\partial t} + \bar{u}_j\frac{\partial \bar{u}_i}{\partial x_j} = -\frac{1}{\rho_a}\frac{\partial \bar{p}}{\partial x_i} + \frac{\partial}{\partial x_j}\left(\nu\frac{\partial \bar{u}_i}{\partial x_j} - \overline{u_i'u_j'}\right). \tag{2.4}$$

Here $(u_1, u_2, u_3) \equiv (u, v, w)$ denotes the velocity vector, (x_1, x_2, x_3) is the Cartesian frame of reference, p is the deviation from hydrostatic pressure, ρ_a the density of air, and ν the kinematic viscosity of air. The tensor summation convention applies. Bars represent Reynolds-averaged quantities and primes denote turbulent fluctuations. The correlations between the velocity fluctuations give rise to the Reynolds stresses $-\rho_a\overline{u_i'u_j'}$ $(i, j = 1, 2, 3)$. The viscous stress is normally neglected since its contribution is only important in the thin viscous sublayer close to the water surface. However, in this chapter it is the focus of our attention. In the remainder of this thesis the bars denoting Reynolds averaging will frequently be dropped for notational convenience.

The flow is assumed to be statistically steady in a frame of reference moving with the waves: $x = x_1 - ct$, where $c = \omega/k$ is the wave phase velocity. The flow is taken to be driven by a horizontal velocity (U_h, V_h) at the top, $x_3 = h$, of the wave boundary layer. The latter is the layer in which the velocity field is influenced by the waves. Since wave-induced perturbations to the air flow generally decay as $\exp(-kx_3)$ (see, e.g., chapter 3), h should be of the order of the wavelength $\lambda = 2\pi/k$. Clearly, if

13

$V_h = 0$, that is the angle θ between wind and wave directions equals $0°$ or $180°$, equation (2.4) for v is superfluous. At the water surface, the boundary conditions are given by the orbital velocities of the wave: $u_0 = a\omega\cos(kx_1 - \omega t)$, $v_0 = 0$, and $w_0 = a\omega\sin(kx_1 - \omega t)$.

2.2.1 Representation of air-flow variables

We are interested in effects of the waves on the air flow. Therefore, we will often consider wave-induced perturbations. The wave-induced part $\tilde{\phi}$ of an air-flow variable ϕ is defined by

$$\tilde{\phi} = \phi - \langle\phi\rangle, \tag{2.5}$$

where $\langle\ \rangle$ represents horizontal averaging over a wavelength

$$\langle\phi\rangle(z) = \frac{1}{2\pi}\int_0^{2\pi}\phi(x,z)\mathrm{d}kx. \tag{2.6}$$

Here, z is either the Cartesian or a wave-following vertical coordinate: see, for example, equation (2.16). In the following, the wavelength-averaged velocity is denoted by capitals ($U = \langle u\rangle$).

For the analysis, it is convenient to consider the amplitude $\widehat{\phi}$ of the first harmonic of $\tilde{\phi}$:

$$\tilde{\phi}(x,z) = \tfrac{1}{2}\left[\widehat{\phi}(z)\mathrm{e}^{\mathrm{i}kx} + \widehat{\phi}^*(z)\mathrm{e}^{-\mathrm{i}kx}\right] + \text{harmonics}, \tag{2.7}$$

where $\widehat{\phi}^*$ denotes the complex conjugate of $\widehat{\phi}$. Since the wave elevation was introduced as $\eta = a\cos kx$, we have $\widehat{\eta} = a$. Hence, the real part $\mathrm{Re}[\widehat{\phi}]$ gives the amplitude in phase with the wave elevation; the imaginary part $\mathrm{Im}[\widehat{\phi}]$ gives the amplitude in phase with the wave slope. A positive value of $\mathrm{Im}[\widehat{\phi}]$ corresponds to an enhancement of ϕ above the backward slope of the wave. Performing the analysis in terms of complex amplitudes allows a clearer interpretation of the results and simplifies the comparison with experimental data.

2.2.2 Dimensionless parameters

At this point it is worthwhile to note which dimensionless parameters determine the solution of the problem described above. The first parameter is the steepness of the wave, ak. As was noted, when the steepness is low ($ak < 0.1$), the first-order perturbations induced by the wavy surface are of primary importance, and nonlinear effects are small. In this case, the actual value of ak does not influence the solution for the wave-induced perturbations, as long as these are scaled with ak. We will focus on waves with a low steepness.

The second parameter is the ratio of the phase velocity of the wave to the wind speed, c/U_h. This parameter is sometimes termed the wave age, although, formally, the wave age is related to a spectrum of waves at the sea, and denotes the ratio of the phase velocity of waves at the peak of the spectrum, c_p, to the wind speed. Different versions of this parameter are used throughout this work: e.g., U/c or c/u_*, where u_* is the friction velocity related to the shear stress at the top of the wave boundary layer

$$u_* = \left(\overline{u'w'}_h^2 + \overline{v'w'}_h^2 \right)^{1/4}. \tag{2.8}$$

The third parameter is related to the type of modelling that is applied. Normally, the viscous sublayer close to the water surface is not explicitly modelled and the viscous stress in (2.4) is neglected. In this case, the nature of the surface is represented by the roughness length z_0, non-dimensionalized as kz_0. Alternatively, if the viscous stress is taken into account, the Reynolds number enters as an additional parameter. Here, the Reynolds number is based on the friction velocity and the wavelength: $Re = u_*\lambda/\nu$. In this case, the flow is modelled down to within the viscous sublayer and the water surface is assumed to be smooth so that z_0 vanishes as a parameter.

Additional parameters are the angle θ, in the case that the waves do not propagate in the wind direction (see section 3.7.1), and the ratio of the density of air and water ρ_a/ρ_w, which comes in as a proportionality factor for the calculation of the growth rate of the waves.

2.3 Structure of the wave boundary layer

In this section we briefly repeat the framework of the rapid distortion theory of turbulence, as introduced by Belcher and Hunt (1993) for the flow over water waves. Special attention will be paid to the inclusion of viscosity into their scaling arguments.

2.3.1 Inner and outer regions

For a proper description of how turbulence in the air flow is affected by surface waves, two timescales are relevant. The advection timescale, $T_A \sim k^{-1}/|U(z) - c|$, represents the time it takes for a turbulent eddy to pass over a wave. On this timescale, turbulent eddies feel changes in the velocity gradient of the mean flow. The eddy-turnover timescale, $T_L \sim \kappa z/u_*$, characterizes the time it takes for turbulent eddies to adjust to the local wind shear.

The wave boundary layer is now divided into inner and outer regions, in which $T_A > T_L$ and $T_A < T_L$, respectively. The height of the inner region, l, is given by

$T_L \sim T_A$ and it is defined with a proportionality constant such that:

$$kl = \frac{2\kappa u_*}{|U(l) - c|}.$$

(2.9)

In the inner region (IR), where $z < l$, eddies adjust to local conditions before they are substantially transported. In the outer region (OR), where $z > l$, they have no time to reach equilibrium with the mean shear; they are rapidly distorted. This implies that the turbulent stress is not correlated with the surface wave, so the wave-induced air flow in the OR is largely inviscid. The inner region has an important physical meaning. It is a thin region in the wave boundary layer where disturbances of turbulent stresses, caused by the interaction of the air flow with the surface, are located. In section 2.5, we will see that these shear-stress perturbations produce asymmetries in the air flow, which finally cause growth of the wave. Experimental evidence of the existence of the IR and the OR above waves was presented by Mastenbroek et al. (1996).

The fact that characteristics of turbulence in the inner and outer regions differ, has consequences for turbulence modelling. In the inner region, where production and dissipation of turbulence are locally in balance, the use of an eddy-viscosity closure is appropriate. However, in the outer region advection of turbulent moments has to be taken into account and this can be done by using a second-order scheme. It was shown by Mastenbroek et al. (1996) that, with such a closure, the effects of rapid distortion can be modelled, whereas eddy-viscosity closures fail to correctly reproduce the wave-induced turbulence in the outer region. For this reason, second-order Reynolds stress models are used in this study (see section 2.4).

Figure 2.1 shows the depth of the IR as a function of both U_k/c, where U_k is the wind speed at $z = k^{-1}$, and c/u_*. The IR depth is generally small in comparison with the depth of the wave boundary layer: $kl \sim 0.1$. Only in the range $U_k/c \approx 1$ the IR is deeper and reaches a maximum $kl \sim 1$. The critical height, z_c, is also shown in figure 2.1. It is the height at which the wind speed equals the phase velocity of the wave: $U(z_c) = c$. The critical height plays a crucial role in quasi-laminar models of the air flow over waves. In chapter 3, this role will be discussed in more detail. Here it suffices to say that kz_c increases with increasing wave-age parameter. In the vicinity of $U_k/c = 1$ it equals the inner region depth. For waves that propagate faster than the wind speed, kz_c rapidly grows and becomes irrelevant to the problem. In this range of wave-age parameters, equation (2.9) for the IR depth has three solutions. Since two of these solutions are located near the critical height and are thus not relevant, only the smallest one is plotted in figure 2.1.
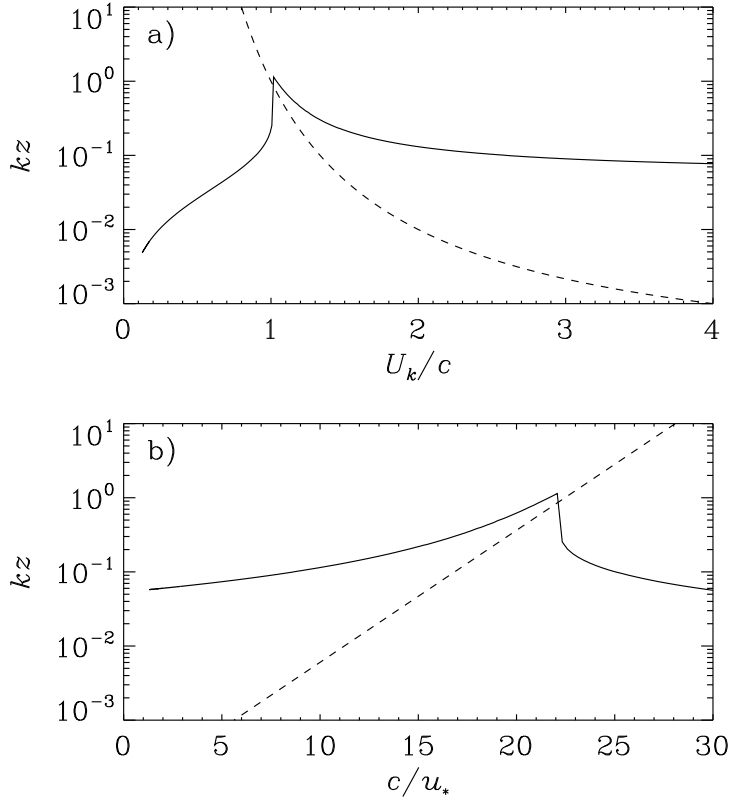
Figure 2.1: Vertical structure of the turbulent boundary layer over a wave as a function of (a) U_k/c, and (b) c/u_*: ——, inner region depth kl; $---$, critical height kz_c. For this plot $kz_0 = 10^{-4}$ was used.

2.3.2 The role of viscosity

In a viscous layer, perturbations to the shear stress decay on a scale

$$z = \left(\frac{2\nu}{k|U(z) - c|} \right)^{1/2}.$$
(2.10)

This fact can be used to generalize (2.9). To this end, we need a rough estimate for the mean horizontal velocity profile, which is obtained by integrating

$$\frac{\mathrm{d}U}{\mathrm{d}z} = \frac{u_*^2}{\nu + \nu_t},$$
(2.11)
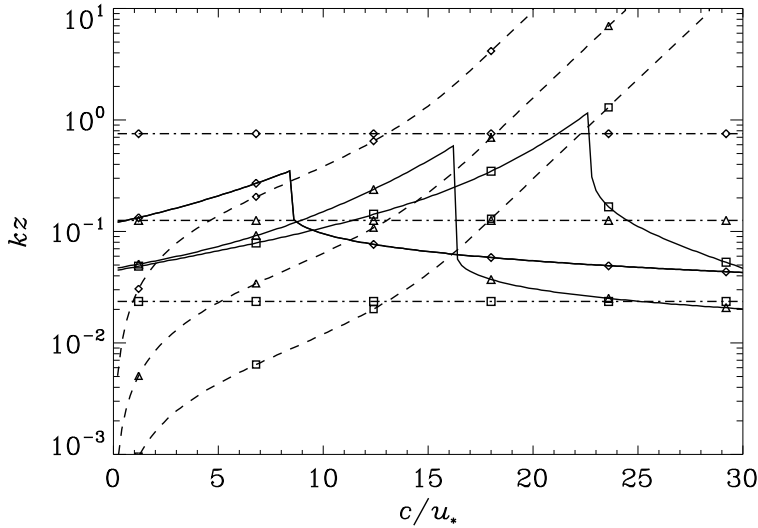
Figure 2.2: Vertical structure of the wave boundary layer for limited Reynolds numbers as a function of c/u_*: ——, inner region depth kl from equation (2.13); — — —, critical height kz_c; — · —, depth of the viscous sublayer kz_v. Symbols represent $Re = 250$ ($\diamond$), $Re = 1500$ ($\triangle$), and $Re = 8000$ ($\square$).

with the turbulent viscosity ν_t defined as

$$\nu_t(z) = \kappa z u_* f_D(z). \tag{2.12}$$

Here $f_D(z) = 1 - \exp(-z^+/A^+)$, with $A^+ = 28$, is the Von Driest damping function (e.g. Baldwin and Lomax 1978). The velocity profile given by (2.11) and (2.12) describes the smooth transition from the viscous sublayer to the turbulent region of the flow in agreement with observations of the turbulent flow over smooth flat plates.

Now the definition of the inner region depth can be generalized to:

$$kl = \left(\frac{2[\nu + \nu_t(l)]k}{|U(l) - c|} \right)^{1/2}. \tag{2.13}$$

This equation represents an estimate of the height at which the combination of viscous and turbulent stress perturbations decays. Note that it assumes a smooth surface.

Figure 2.2 shows the inner region depth following from (2.13) as a function of c/u_* for three different Reynolds numbers. The height of the viscous sublayer, given

here by $z_\nu^+ = 30$, is also shown. For $Re = 8000$, the larger part of the inner region is outside the viscous layer. This means that asymmetry in the flow is mainly created by turbulent stresses. By contrast, when $Re = 250$, the inner region falls completely within the viscous layer and thus molecular forces are responsible for wave growth.

The critical height based on the velocity profile following from (2.11) is also plotted in figure 2.2. With decreasing Reynolds number, the kz_c-curve shifts towards lower values of c/u_*. This is mainly due to the fact that for smooth flow the drag, i.e. the ratio u_*/U_k, increases with decreasing Reynolds number so that $U_k \approx c$ corresponds to a lower value of c/u_*. As a result, the peak of kl shifts in the same direction.

2.4 The numerical model

2.4.1 Turbulence closure

Before the governing equations can be solved, a closure scheme for the Reynolds stresses $\overline{u_i' u_j'}$ has to be chosen. Mastenbroek (1996) compared a number of turbulence closure schemes, ranging from a simple mixing length model to an advanced second-order closure (Launder et al. 1975, henceforth LRR). His conclusion, after comparison with laboratory experiments, was that for a proper description of turbulence above the waves, a second-order closure is needed. Therefore, we will use the LRR model in the present study, which involves solving balance equations for the six components of the Reynolds-stress tensor.

$$\frac{\partial \overline{u_i' u_j'}}{\partial t} + \overline{u}_k \frac{\partial \overline{u_i' u_j'}}{\partial x_k} = P_{ij} + d_{ij} + \phi_{ij} - \varepsilon_{ij}, \tag{2.14}$$

where the terms on the right-hand side denote production, diffusion, pressure–strain correlations, and dissipation, respectively. Additionally, an equation is solved for the dissipation rate, ε, of turbulent kinetic energy, $e = \frac{1}{2} \overline{u_i' u_i'}$,

$$\frac{\partial \varepsilon}{\partial t} + \overline{u}_i \frac{\partial \varepsilon}{\partial x_i} = -\frac{\partial \overline{\varepsilon' u_i'}}{\partial x_i} + \frac{\varepsilon}{e} \left(c_{\varepsilon 1} \frac{P_{ii}}{2} - c_{\varepsilon 2} \varepsilon \right), \tag{2.15}$$

where $c_{\varepsilon 1}$ and $c_{\varepsilon 2}$ are constants. Many terms in these equations require modelling, which is provided by the LRR scheme, described in detail in appendix A.1.

19

2.4.2 Computational setup

For solution of the conservation equations, the coordinates (x_1, x_3) are transformed to wave-following coordinates (x, z), where

$$z = h \frac{x_3 - \eta(x)}{h - \eta(x)}. \tag{2.16}$$

The top of the model domain is taken as $h = \lambda$. The domain is then given by $0 < x, z < \lambda$.

At the up- and downstream boundaries, periodic conditions are applied. At the lower boundary, the orbital velocities of the wave are imposed. Furthermore, the roughness length is specified. Via z_0, the local tangential surface stress along the wave surface is calculated and, subsequently, equilibrium values for the turbulent stresses and the dissipation are imposed. In boundary layers, the dissipation ε is inversely proportional to the distance from the surface. Therefore, Mastenbroek (1996) rewrote the ε-equation in terms of εz to limit the dynamical range of this variable in the model. The equilibrium value for the dissipation rate at the surface is then $\varepsilon z = u_*^3 / \kappa$, where $\kappa = 0.41$ is the von Kármán constant, and u_* is calculated from the local tangential surface stress. At the upper boundary, the horizontal velocity components are specified. The vertical velocity component, as well as the gradient of the turbulent moments and εz are set to zero.

The conservation equations, (2.3), (2.4), (2.14), and (2.15), comprise a set of 11 coupled nonlinear partial differential equations for 11 flow variables, subject to the boundary conditions described above. They are solved in the following way. The momentum equations are rewritten to obtain a Poisson equation for the pressure. This equation is solved using the successive over-relaxation method with Chebyshev acceleration. The conservation equations are then iteratively integrated forward in time with a second-order predictor–corrector method, where, at every timestep, an updated value for the pressure, as obtained by the above method, is used. The difference between integration with a first- and second-order accurate method is used to estimate the optimal size of the next timestep. The calculations start from an initial condition and proceed until a steady state is reached.

For the spatial discretization of the conservation equations, a second-order finite difference method is used. The grid is staggered: the pressure is calculated at cell centres, the other variables at cell edges. To obtain sufficient resolution near the surface, non-uniform meshes are used in which the grid points are closely spaced near the air-water interface and distributed logarithmically away from the surface. The spacing between two subsequent vertical layers increases with a constant factor. A typical mesh has 60–80 points in the vertical and 32 (uniformly spaced) in the horizontal direction. With these grids, the solution is found to be indifferent

20

to a further increase of the resolution. More detailed information on the numerical implementation can be found in Mastenbroek (1996) and Burgers and Makin (1993).

2.4.3 The low-Reynolds-number model

When effects of low Reynolds numbers are to be investigated, the viscous stresses in (2.4) must be retained. Turbulence modelling is again accomplished with a second-order closure scheme, which must now, however, be valid down to the viscous sublayer close to the air–sea interface. Such a closure was presented by Craft and Launder (1996). This low-*Re* model is based on equations (2.14) and (2.15) but includes many modifications, accounting for effects due to inhomogeneity, strong anisotropy, and the damping of the fluctuating vertical velocity component normal to the wall. The final form of the low-*Re* model used for the present study is described in appendix A.2.

The only differences in boundary conditions compared to the high-*Re* model are at the lower boundary. There, the homogeneous dissipation rate ε^* (see appendix) and the Reynolds stresses are simply set to zero. An additional difference is that the equation for ε^* is not rewritten to $\varepsilon^* z$, since this gives numerical problems near the surface. Meshes are chosen such that at least some grid points are within the viscous sublayer, bounded by $z^+ = z u_* / \nu < 5$. At low Reynolds numbers, this can be achieved with 60 grid points and a moderate stretching away from the surface. However, at the largest Reynolds numbers considered, $Re \sim 10^4$, at least 80 grid points and a strong stretching are necessary. This, clearly, leads to an increase in the computational requirements. The same numerical method and discretization as described earlier are used to solve the governing equations.

2.5 Comparison with experiment

In this section, model calculations are compared with the experiment of Stewart (1970). In this experiment, detailed observations of the velocity field above water waves were performed. The observations are particularly suited for comparison with the present model, since the Reynolds numbers are low: $Re = 870$–3000. Additionally, the flow can be considered smooth. An indicator for this is the roughness Reynolds number, $Re_r = z_0 u_* / \nu$, which is approximately $Re_r = 0.24$ in Stewart's experiment, whereas an ideally smooth surface would give $Re_r = 0.11$. A wide range of wave ages is covered, which allows a detailed investigation of wave-age dependence. Other laboratory observations of the air flow over water waves include those by Hsu and Hsu (1983) and Mastenbroek et al. (1996). However, they are less appropriate for the present purposes, because their Reynolds numbers are fairly high

($6000 < Re < 13\,000$ for Hsu and Hsu and $8700 < Re < 13\,000$ for Mastenbroek et al.. In chapter 3, where a simplified model for the air flow over waves is developed, comparisons with the former experiment will be shown.

2.5.1 Experimental setup

Stewart's measurements were carried out in a wind–water tunnel, which was 5.90 m long, 59 cm high and 57 cm wide and contained 21 cm of water. The waves were created by a submerged flat plate, hinged at the bottom. They had a wavelength $\lambda = 40.8$ cm and an amplitude $a = 0.64$ cm (steepness $ak = 0.1$). The waves were short enough not to feel the bottom of the tank, so that the deep-water dispersion relation gives $c = 79.6$ cm s^{-1}. A fan at the downwind end of the tunnel produced a variable wind speed. From the seven reported cases, we pick three to compare with the numerical model. An overview of the free-stream velocities U_∞ for these cases is given in table 2.1. The instruments were located at 3.96 m from the entrance and

Case	U_∞ [m s^{-1}]	u_* [m s^{-1}]	Re	c/u_*	U_λ/c	kl	kz_c	kz_ν
1	2.27	0.117	3015	6.83	3.46	0.11	0.02	0.06
4	1.02	0.058	1487	13.9	1.58	0.49	0.27	0.13
7	0.56	0.036	867	23.8	0.86	0.03	24	0.22

Table 2.1: Parameters for selected cases of Stewart's experiment.

2.74 m from the wave-maker. At this location the boundary-layer depth was about 10 cm. The velocity measurements were performed with hot-wire anemometers.

2.5.2 Error estimation

Stewart gave a detailed estimate of the errors in the observations. The first class of error sources includes the inaccuracy of the electronic measurements, the temperature dependence of the hot wires and the inaccuracy of the calibrations. These lead to an accuracy of the mean velocity within 1.5%. Next, there are geometrical errors in resolving the velocity components, so that part of the horizontal velocity can appear as a vertical velocity. These errors are particularly felt in the wave-induced velocities $\tilde{u}$ and $\tilde{w}$. These quantities are thought to be resolvable to 1% of the mean horizontal velocity. The measurements of the spectra of the wave-induced velocities include contributions from turbulent fluctuations. However, these contributions are found to be small and thus cause little error. The influence of fluctuations in U_∞ on the results was tested by repeating the measurements several times. The magnitude of $\widehat{u}$ and $\widehat{w}$ was found to vary about 20% and the phase about 10$^\text{o}$. Finally, the error

made in retrieving the data from the plots in Stewart is small enough to be ignored. The error bars in figures 2.3 to 2.5 show the largest of the errors above mentioned. However, at the lowest wind speeds, notably in case 7, the accuracy of the hot-wire anemometers is questionable and the error may be larger.

2.5.3 Setup of the simulations

In the simulations we attempt to approximate the experimental conditions as closely as possible. Special care is necessary for the wind speed. In the model, an open boundary layer is simulated and the flow is driven by U_λ, the mean horizontal wind speed at height $z = \lambda$. In contrast, the experiment is in a tunnel and the flow is forced by a pressure gradient. To define the model runs a value for U_λ is obtained by extrapolating the logarithmic part of the mean horizontal velocity profile of the measurements to the height λ. This leads to the values in table 2.1.

Of course caution is needed when comparing confined-flow experiments with open-boundary-layer calculations. However, it can be argued (e.g. Yaglom 1979) that the influence of the pressure gradient in a channel flow may be neglected when $z \ll \delta_p$, where δ_p is the pressure gradient lengthscale, which equals the channel half-width. In the experiment $\delta_p = 19$ cm and measurements were taken at $z < 8$ cm.

Another parameter to be specified in the high-*Re* model is the surface roughness z_0. It is obtained from the logarithmic fit through the mean velocity data.

2.5.4 Results

In figures 2.3 to 2.5 the observed vertical profiles of the amplitudes of the wave-induced velocity are compared with those computed by the numerical model. The amplitudes are scaled with the wave steepness *ak* and the velocity at the centre of the channel U_∞. The vertical axis gives the dimensionless height kx_3 above the mean water level.

Figure 2.3 shows the results for the highest wind speed. This case is typical for a relatively slow wave. The models predict almost the same vertical profiles for the real part of the horizontal, $\mathrm{Re}[\widehat{u}]$, and the imaginary part of the vertical velocity perturbation, $\mathrm{Im}[\widehat{w}]$. These two components form the part of the flow in phase with the wave, i.e. in phase with the orbital movement of the water. Compared to the measurements, $\mathrm{Im}[\widehat{w}]$ is overestimated. The components $\mathrm{Re}[\widehat{w}]$ and $\mathrm{Im}[\widehat{u}]$ are created by the work of viscous and turbulent stresses in the inner region. This can be clarified with the out-of-phase part of the momentum conservation equation (2.4) for the wave-induced perturbations, which reads in Cartesian coordinates:

$$-(U-c)\mathrm{Im}[\widehat{u}] + \mathrm{Re}[\widehat{w}]\frac{\mathrm{d}U}{\mathrm{d}kx_3} = \frac{1}{\rho_a}\left(\mathrm{Im}[\widehat{p}] + \frac{\mathrm{dRe}[\widehat{\tau}]}{\mathrm{d}kx_3}\right), \qquad (2.17)$$

23
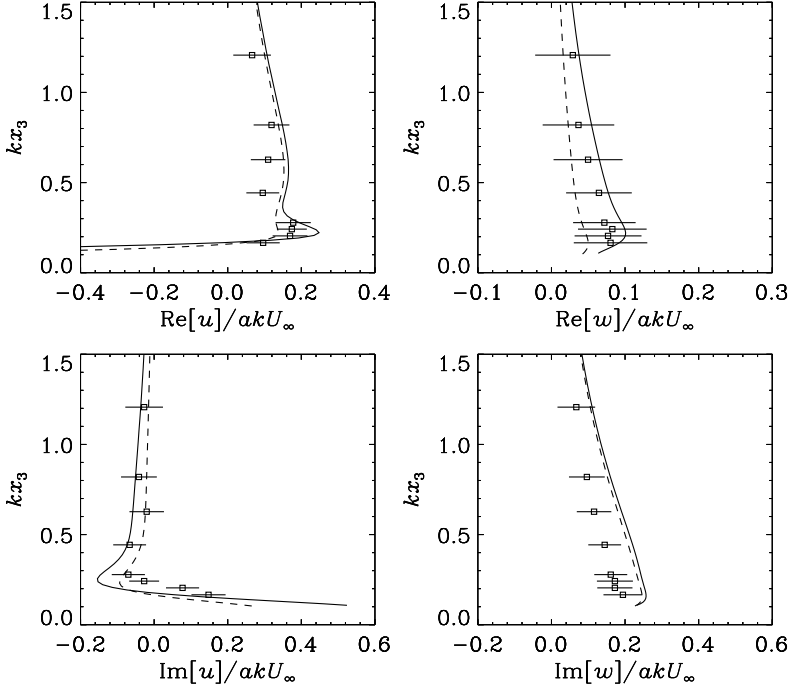
Figure 2.3: Vertical profiles of the wave-induced amplitudes of the horizontal and vertical velocity for case 1: ——, low-*Re* model; – – –, high-*Re* model; □, measurements (Stewart 1970) with error bars.

$$(U - c)\mathrm{Re}[\widehat{w}] = \frac{1}{\rho_a} \left(-\frac{\mathrm{dIm}[\widehat{p}]}{\mathrm{d}kx_3} + \mathrm{Re}[\widehat{\tau}] \right). \qquad (2.18)$$

Here, the shear stress τ is the sum of a viscous and a turbulent contribution:

$$\tau = \rho_a \nu \left(\frac{\partial u}{\partial x_3} + \frac{\partial w}{\partial x_1} \right) - \rho_a \overline{u'w'}. \qquad (2.19)$$

Normal turbulent and viscous stresses have been left out for convenience. If there is no stress perturbation acting as a forcing in these equations, then no $\mathrm{Re}[\widehat{w}]$ and $\mathrm{Im}[\widehat{u}]$ will be formed. This is the case in inviscid flow. However, the shear stress, related to the components $\mathrm{Re}[\widehat{u}]$ and $\mathrm{Im}[\widehat{w}]$, produces asymmetry in the flow. The energy flux from the air to the waves is related to the pressure–slope correlation $\mathrm{Im}[\widehat{p}]$ at the surface (see section 2.6). This component is found by integrating (2.18) from the wave amplitude to infinity:

$$\mathrm{Im}[\widehat{p}]_{x_3=a} = \int_a^\infty \rho_a(U - c)\mathrm{Re}[\widehat{w}]\mathrm{d}kx_3 - \int_a^\infty \mathrm{Re}[\widehat{\tau}]\mathrm{d}kx_3. \qquad (2.20)$$
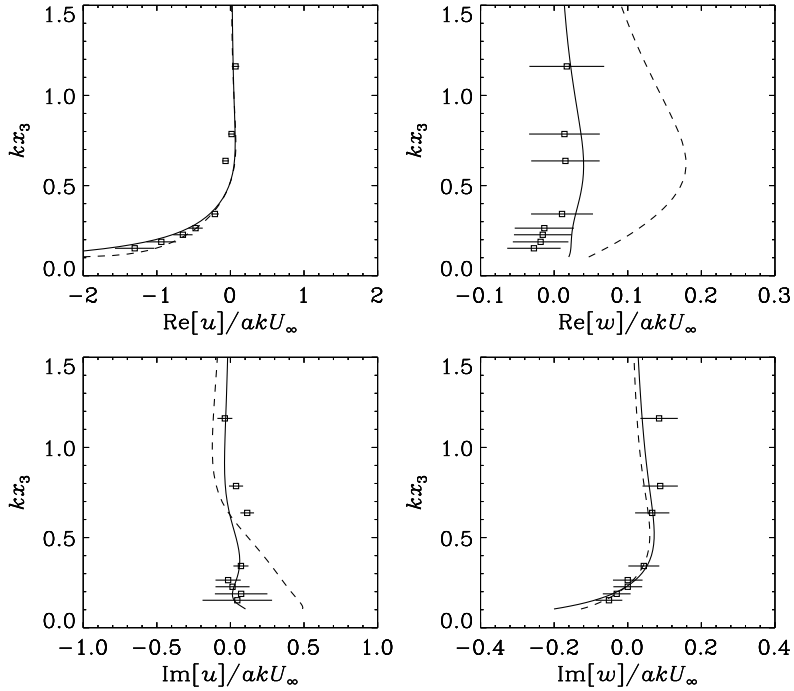
Figure 2.4: As figure 2.3 but for case 4.

The component $\text{Re}[\hat{w}]$, which is formed in the thin inner region, decays exponentially in the outer region, where it contributes to the slope-correlated pressure according to the first integral on the right-hand side of (2.20). As was noted before, the shear-stress perturbations are almost zero in the outer region and thus the contribution of the second integral to the growth rate is normally small. Hence, the magnitude of $\text{Re}[\hat{w}]$ gives a good indication of the growth rate. In figure 2.3 it can be seen that the low-*Re* model predicts a larger $\text{Re}[\hat{w}]$ than the high-*Re* model. This corresponds to a higher growth rate at this Reynolds number ($Re \approx 3000$). The measurements are not precise enough to favour one of the two models.

Case 4, which has $Re \approx 1500$ and $c/u_* \approx 14$, is presented in figure 2.4. The model predictions for the part of the flow in phase with the wave are similar and in agreement with the measurements. The observations further indicate that $\text{Re}[\hat{w}]$ is about zero, which corresponds to hardly any growth. This is clearly reproduced by the low-*Re* model. However, the high-*Re* model predicts large values for this component. According to this model, a wave with $c/u_* \approx 14$ is in the intermediate regime, i.e. it is in the transition range between slow and fast. For these waves, the
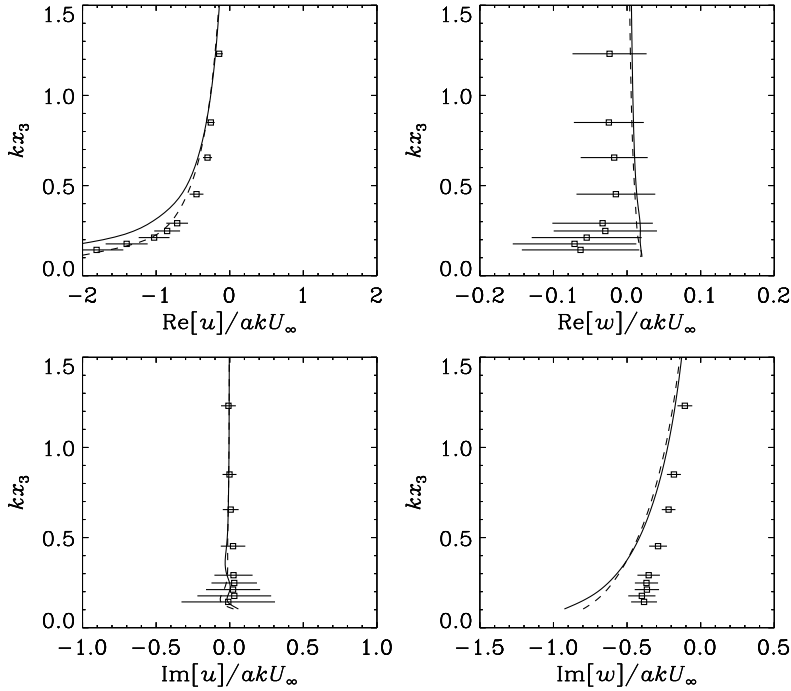
Figure 2.5: As figure 2.3 but for case 7.

highest growth rates are predicted, and thus a large value for $\mathrm{Re}[\widehat{w}]$ is found. From figure 2.2 it can be seen that when Re becomes lower, the region of intermediate waves shifts to lower wave ages. Therefore, the low-Re model treats this wave as a fast wave, meaning no growth and almost zero $\mathrm{Re}[\widehat{w}]$. Notice that the predicted profile of $\mathrm{Im}[\widehat{u}]$ also shows good agreement with the measurements.

In figure 2.5 the wave-induced velocity profiles for case 7 are plotted. This case concerns a fast wave. Here, the wave-induced air flow is practically inviscid. The orbital velocities are dominating, and the part of the flow out of phase with the wave elevation is almost zero. This feature is shown by both models. In this case the way in which stresses are parameterized has hardly any influence on the wave-induced velocity profiles. Therefore, the results from both models are almost the same.

It is unclear why the computations for $\mathrm{Im}[\widehat{w}]$ differ so much from the observations. The measurements seem to violate continuity. This can be observed by regarding the in-phase part of the continuity equation (in Cartesian coordinates):

$$\mathrm{Re}[\widehat{u}] = -\frac{\mathrm{d}\,\mathrm{Im}[\widehat{w}]}{\mathrm{d}kx_3}. \tag{2.21}$$

While the observations show that the derivative of $\text{Im}[\widehat{w}]$ tends to zero near the surface, $\text{Re}[\widehat{u}]$ is large and negative. Possibly, this discrepancy is due to the fact that the wind speed is very low and thus the accuracy of the hot-wire measurements breaks down. The existence of a secondary flow may be a different explanation. Such a secondary flow can arise in the flow over smooth wavy surfaces (Gong et al. 1996). When it is present, continuity in two dimensions is, of course, not obeyed.

2.6 Growth rates

In this section some results will be presented concerning the growth rate. This quantity reflects the energy transfer from wind to waves and is crucial as input in wave models. The energy flux, $\dot{E}$, per square metre of water surface from the air to a wave can be written as:

$$\dot{E} = \langle -p(w - \eta_x u) + \tau(u - \eta_x w)\rangle_{z=0}, \tag{2.22}$$

with $\eta_x = \partial\eta/\partial x$. The shear stress τ, see equation (2.19), contains turbulent as well as viscous contributions. A contribution of normal stresses to the growth is also present but has been omitted here for convenience, as it is small for all wave speeds. For slow waves, the flux is formed mainly by the pressure–slope correlation, while for fast waves the contribution via the shear stress is dominant (see Mastenbroek et al. 1996). The energy flux is normally scaled with the energy, E, of the wave per unit surface area. For a sinusoidal wave, either in the gravity or capillary range, the energy is given by $E = \frac{1}{2}\rho_w k c^2 a^2$.

The growth rate due to the wind is defined as $\gamma = \dot{E}/E$. However, the results will mostly be presented in the form of the growth-rate parameter β, which is defined as (see, e.g., Townsend 1972)

$$\frac{\dot{E}}{\omega E} = \frac{\rho_a}{\rho_w}\left(\frac{u_*}{c}\right)^2 \beta. \tag{2.23}$$

While (2.22), plus the normal stress contribution, is used to calculate β from the model results, for low steepness it provides insight to linearize (2.22), which leads to:

$$\beta = \frac{(\text{Im}[\widehat{p}] + \text{Re}[\widehat{\tau}])_{z=0}}{ak\rho_a u_*^2}. \tag{2.24}$$

2.6.1 Impact of Reynolds number on growth rate

First, attention will be paid to the impact of the Reynolds number on the growth rate of relatively slow waves ($c/u_* < 5$). In figure 2.6 predictions of the low-*Re* model are compared with measurements by Larson and Wright (1975) and with the analytical model of Van Gastel et al. (1985). They presented the growth rates in dimensional
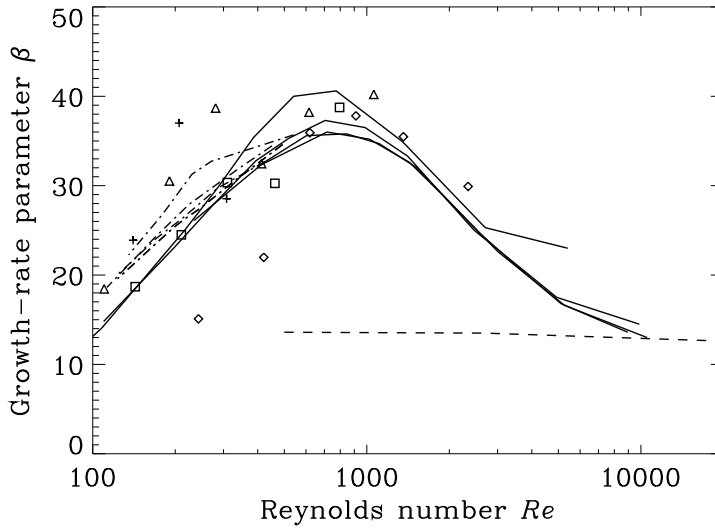
Figure 2.6: Growth rate as a function of Reynolds number. ——, low-*Re* model (various u_*); $---$, high-*Re* model; $-\cdot-$, Van Gastel et al. (1985). Symbols show measurements of Larson and Wright (1975): +, $u_* = 0.12$ m s^{-1}; $\square$, $u_* = 0.18$ m s^{-1}; $\triangle$, $u_* = 0.24$ m s^{-1}; $\diamond$, $u_* = 0.53$ m s^{-1}.

form as a function of k for constant u_*. Then, analysis is complicated because the dimensional growth rate increases quadratically with the friction velocity. We present the data in the non-dimensional form of β, as defined in (2.23). The low-*Re*-model results were obtained for low-steepness waves ($ak = 0.01$). The individual curves show results for a constant u_*. Between the curves, u_* varies from 0.14 to 0.9 m s^{-1}. The fact that they almost coincide indicates that the Reynolds number is indeed the most important explaining parameter; variations in the wave age cause only slight differences for these slow waves.

Van Gastel et al. (1985) described analytically the growth of gravity–capillary waves using linear instability theory. With asymptotic methods, they solved the governing Orr–Sommerfeld equation for the perturbations to a given basic flow, both in the water and in the air. Viscosity was taken into account, but turbulence was neglected. They presented net growth rates; i.e. including dissipation due to the viscosity of the water. To compare with our model, we add to their growth rate results (see their figure 2) the viscous dissipation term $4\nu_w k^2$, where ν_w is the kinematic viscosity of water. The curves, which were obtained for u_* varying between 0.14 and 0.25 m s^{-1}, coincide reasonably. The agreement between our model and their ana-

lytical results is excellent. This confirms the validity of our numerical model in the very low *Re* range. Although Van Gastel et al. neglected turbulence, the agreement is perhaps not so surprising, since at these low Reynolds numbers growth is mainly created by viscosity.

Larson and Wright (1975) measured growth rates in a laboratory wave tank using microwave backscatter. Their radars were aligned to respond to waves with wavelengths in the range 0.7–7 cm. To isolate the growth due to wind, they added to the measured values the viscous dissipation term, as described above. To non-dimensionalize their growth rates we use values of u_* other than those reported. Donelan and Pierson (1987) pointed out that the reported values are too large, since they were measured at steady state after the wave spectrum had attained its fetch limit. The exponential growth of the waves under consideration, though, took place in the first seconds, when the fetch limit had not yet been reached. Therefore, they proposed alternative values, as listed in the figure caption. Although some scatter in the measurements remains, the general agreement between model and observations is good.

The predicted growth rate shows a maximum $\beta \approx 35$ at $Re \approx 800$. Towards higher Reynolds numbers β decreases and at $Re \approx 10^4$ the difference between low- and high-*Re* models disappears. Therefore, we conclude that for $Re > 10^4$ the influence of viscosity near the water surface may be neglected. Note that the high-*Re* model is in principle not dependent on the Reynolds number. However, we used $z_0 = 0.11\nu/u_*$ and thus *Re* influences the calculations indirectly via the roughness length. From figure 2.6 it is clear that this influence is small.

The differences between the high- and low-*Re* models are shown in more detail in figure 2.7. The figure gives vertical profiles of wave-induced perturbations in wave-following coordinates for $Re = 1000$, which is near the peak of the predicted growth rates. The enhanced growth rate of the low-*Re* model can be inferred directly from the imaginary part of the pressure perturbation. The maximum of $\text{Re}[\widehat{w}]$ is also clearly much higher in the low-*Re* model. The reason for the increased growth is not completely clear. The maximum around $Re = 800$ is also observed for the form drag of hills, as is presented in the next section. There we will discuss possible explanations.

2.6.2 Form drag on a smooth hill

We now turn to the limiting case of the flow over smooth stationary rigid waves. In the notation of this article this case is represented by $c = u_0 = w_0 = 0$ m s^{-1}. The form drag, S, on such hills is the equivalent of the growth rate parameter for waves.
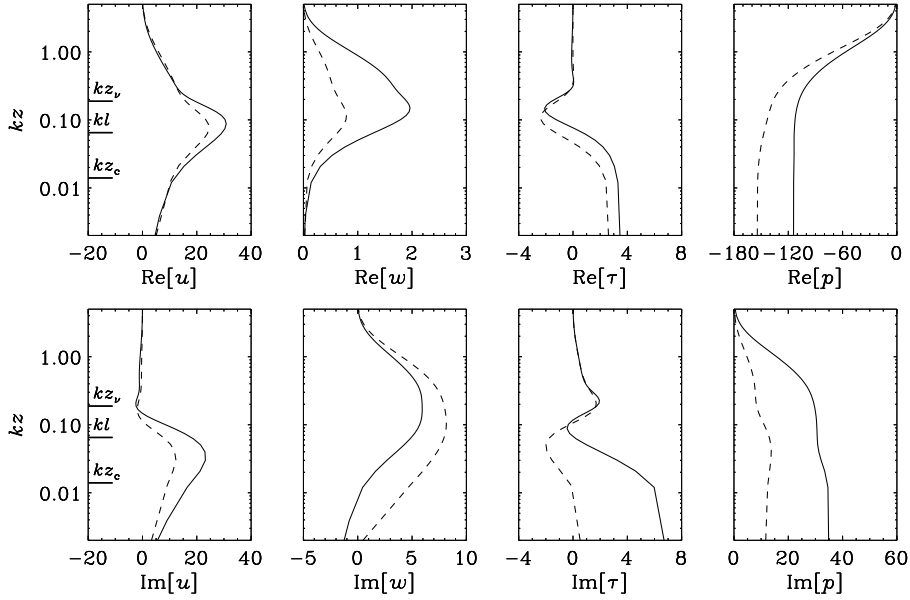
Figure 2.7: Vertical profiles of wave-induced perturbations above a slow wave ($c/u_* = 2$) at $Re = 1000$: ——, low-*Re* model; $---$, high-*Re* model. The heights of the critical layer, inner region, and viscous sublayer ($z_v^+ = 30$) are indicated by horizontal bars. The velocity perturbations $\widehat{u}$ and $\widehat{w}$ are normalized with aku_*; the shear-stress perturbation $\widehat{\tau}$ and pressure perturbation $\widehat{p}$ are normalized with $ak\rho_a u_*^2$.

It is defined as

$$S = \frac{2\pi\langle p\eta_x\rangle_{z=0}}{\rho_a u_*^2(ak)^2}. \tag{2.25}$$

Harris et al. (1996) found that the form drag on a hill increases strongly when the Reynolds number becomes low, as shown in figure 2.8. They solved, apart from the base flow, linearized equations for the wave-induced perturbations. Turbulence was modelled by the e-ε scheme. This closure is based on an eddy viscosity and thus, as was noted before, overestimates Reynolds-stress perturbations in the outer region. To solve this problem Harris et al. damped the eddy viscosity in the outer region. Both the present model and Harris et al. show an increase of *S* for low *Re*. This again gives evidence that viscous effects must be taken into account; the high-*Re* model cannot reproduce the trend of enhanced form drag.

The low-*Re* model predicts a peak of the form drag for $Re \approx 800$; at lower Reynolds numbers *S* decreases again. For β, in the case of a slowly moving wave, this was also noticed and found in experiments (see section 2.6.1). In contrast, Har-

30
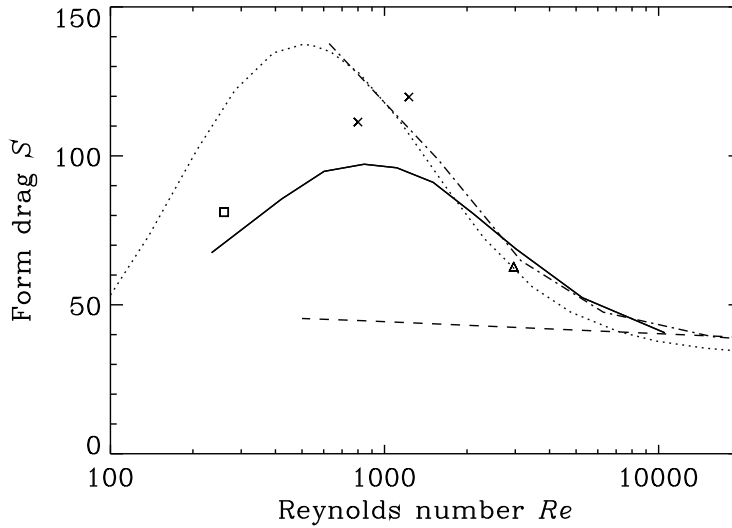
Figure 2.8: Form drag on a smooth hill as a function of Reynolds number: ——, low-*Re* model; − − −, high-*Re* model; − · −, Harris et al. (1996); · · · , Harris (update); △, Zilker and Hanratty (1979); ×, Henn and Sykes (1999); □, Sullivan et al. (2000).

ris et al. (1996) found no reduction of the form drag towards low Reynolds numbers. However, recent calculations, represented by the dotted line in figure 2.8, with their model for $Re < 600$ did lead to such a reduction (J. A. Harris, personal communication). The updated drag values are slightly lower since the definition of their eddy-viscosity damping function was modified to take into account the actual value of the mean velocity profile. Certainly they are considerably higher than predicted by our model, yet a similar trend is found.

In figure 2.8 the form drag from an experiment by Zilker and Hanratty (1979) is also plotted. It is in good agreement with our low-*Re*-model predictions. Recently, Henn and Sykes (1999) presented results of their large-eddy simulations of the flow over hills. They found drag values more than twice as large as Zilker and Hanratty. They then claimed that Zilker and Hanratty's form drag was not consistent with an integration of the measured surface pressure data and should therefore be treated with caution. However, Henn and Sykes performed their simulations at a much lower Reynolds number than Zilker and Hanratty. According to the present model results this explains the discrepancy of the form drag values. Sullivan et al. (2000) conducted direct numerical simulations of the flow over waves at $Re = 260$. The form drag resulting from their model appears to confirm that S decreases towards
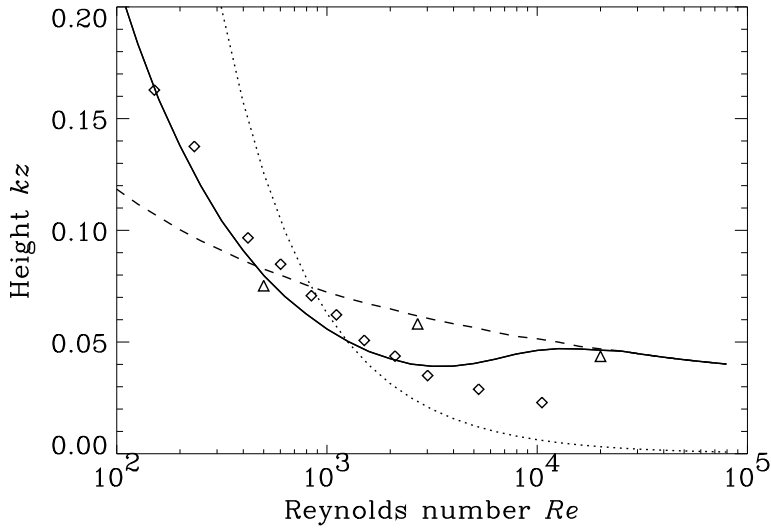
Figure 2.9: Inner region depth in flow over hills: ——, kl from (2.13); − − −, kl from (2.9); $\cdots$, $z^+ = 10$; symbols denote half the height where $\max\left(\text{Re}[\widehat{w}]/u_*\right)$ is located, from the low-Re (⋄) and high-Re (△) models.

very low Reynolds numbers.

An interesting question concerns the existence of a maximum form drag around $Re = 800$. First, we note that a critical layer does not exist over hills, so this can be excluded from our considerations. The depth of the inner region and of the viscous sublayer are expected to be important scales.

The inner region depth is supposed to be related to the height where the maximum of $\text{Re}[\widehat{w}]$ is located, since $\text{Re}[\widehat{w}]$ is formed in the inner region and decays exponentially in the outer region, where the shear-stress perturbations vanish. Thus, it is useful to compare this height with the estimates for kl, (2.9) and (2.13). These estimates were derived from scaling arguments and are fixed except for an $O(1)$ factor. Hence, they are plotted in figure 2.9 together with half the height of the maximum of $\text{Re}[\widehat{w}]$ found in the numerical calculations. A good agreement is found, except at the highest Re. This indicates that the kl-estimates are in general consistent with the numerical calculations.

The scale of the viscous sublayer is also plotted. It is defined here at $z^+ = 10$, where the (continued) linear and logarithmic part of the mean velocity profile intersect. Around $Re = 10^3$ the inner region and the viscous sublayer are of comparable depth. For lower Re the inner region is located inside the viscous layer. This means
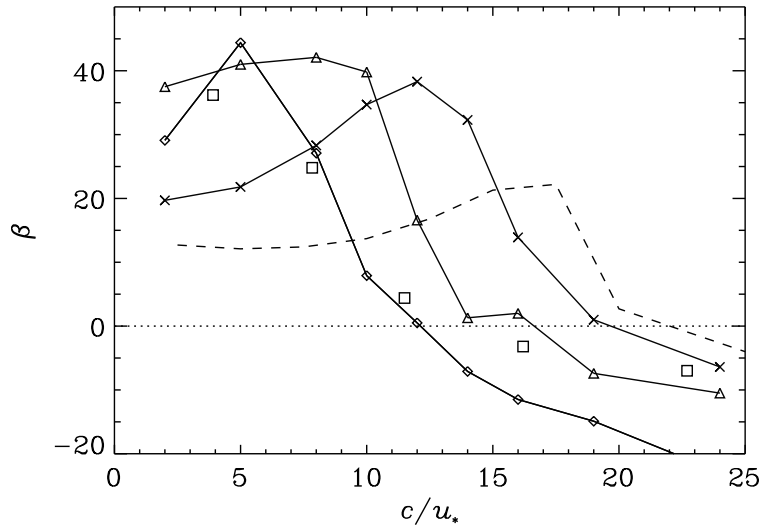
Figure 2.10: Growth rate as a function of wave-age parameter: ——, low-*Re* model for $Re = 260$ ($\diamond$), $Re = 1000$ ($\triangle$) and $Re = 4000$ ($\times$); $---$, high-*Re* model ($kz_0 = 10^{-4}$); $\square$, direct numerical simulation at $Re = 260$ by Sullivan et al. (2000).

that mainly viscous stresses are responsible for creating asymmetry in the flow. In contrast, for higher *Re* the viscous layer is a negligible part of the inner region, so that turbulent stresses cause asymmetry. Around $Re = 10^3$ both mechanisms are active in establishing the form drag. This combination appears to be very effective, leading to a maximum drag.

2.6.3 Impact of wave age on growth rate

So far, we have discussed the flow over hills and slowly moving waves. Now the growth of faster waves is investigated. In figure 2.10 the growth rate is shown as a function of the wave age. The predictions of the high-*Re* model were presented in Mastenbroek et al. (1996). They give rise to the following picture of wave growth (see Belcher and Hunt 1998). For slow waves, with $c/u_* < 10$, the critical layer plays no dynamical role (see also section 3.3.1). Growth is caused by the work of stresses in the inner region. With increasing wave age the inner region thickens and the critical-layer height increases. Apart from the asymmetry created by turbulent stresses, additional asymmetry could be provided by the critical-layer mechanism (Miles 1957). However, the details of the role of the critical layer in the inner region,

which is not inviscid, remain to be clarified. When the wave age increases even further, negative growth from the reverse flow below the critical height becomes important. This explains the sharp drop in β around $c/u_* = 19$. In (2.20) this effect is seen in the Re$[\widehat{w}]$ term: below z_c its contribution is negative. Finally, fast waves, with $c/u_* > 20$, have effectively a reverse air flow, which damps the wave. The critical height is so large that it plays no role.

The same picture also seems to be valid for the low-*Re*-model results. There are two differences, however. First, the growth rate curves shift to lower wave ages, when the Reynolds number decreases. This shift must be related to the fact that the critical-layer height increases when *Re* becomes lower (see figure 2.2). Thus, the definition of slow, intermediate and fast wave regimes, should be altered like-wise. Secondly, the magnitude of β for slow waves is higher according to the low-*Re* model, as was pointed out before. This result is in agreement with the parameterization of Plant (1982), who concluded, on the basis of various experimental data, that for slow waves $β = 32 \pm 16$.

In figure 2.10 the growth-rate values found in the direct numerical simulations of Sullivan et al. (2000) are represented by squares. They are in excellent agreement with our calculations at $Re = 260$, except that, for unclear reasons, we predict a much stronger damping of fast waves.

2.7   Conclusions

Laboratory observations of the air flow above water waves show that high-*Re* turbulence models cannot correctly reproduce this air flow when its Reynolds number is low. Therefore, corrections are necessary to include effects of viscosity close to the water surface. In this paper a turbulence closure scheme (Craft and Launder 1996) is applied that takes into account such effects.

In comparison with laboratory observations of the wave-induced velocity field above waves by Stewart (1970) the low-Reynolds model in general leads to im-proved agreement. In the case with the highest wind speed, the high-*Re* and low-*Re* models perform similarly. In an intermediate case, observations show that the veloc-ity components out of phase with the wave are suppressed. In contrast to the high-*Re* model this is reproduced by the low-*Re* version. Finally, a case with a very low wind speed, and a relatively fast wave, again leads to similar predictions by both models. Here, the wave-induced air flow is practically inviscid, and, thus, the way in which stresses are parameterized is not so important for the velocity perturbation profiles.

A quantity directly following from the velocity, stress, and pressure distributions above waves is the growth rate. It is shown that the growth rate of slowly moving waves increases when the Reynolds number becomes smaller than 10^4, with up to

almost a factor 3 for $Re \approx 800$. For smaller Re, the growth rate drops again. A similar maximum is also found for the form drag on smooth stationary waves. It seems to be related to the relative depths of the inner region and the viscous sublayer. These are comparable near the location of the maximum, meaning that viscous and turbulent stresses both play a role in creating growth.

Observed growth rates, e.g. those compiled by Plant (1982), are larger than predicted by advanced turbulence models and exhibit an amount of scatter that is not taken away by a wave age dependence. The present modelling work indicates that the Reynolds number is necessary to explain the growth rates of short laboratory waves. This is confirmed by a comparison with the microwave-backscatter experiments of Larson and Wright (1975). In the field, the enhanced growth also has an impact. If, for example, the wind speed is around 10 m s^{-1}, corresponding to $u_* \approx 0.4$ m s^{-1}, then viscous effects will be important for the waves in the spectrum with $\lambda < 40$ cm. The waves in this range support most of the momentum flux from the atmosphere to the sea and are important for remote sensing applications.

Chapter 3

A semi-analytical model for the air flow over waves

In the previous chapter, numerical models with advanced turbulence closure schemes have been used to simulate the air flow over waves. While such models are capable of accurately predicting typical features of the wave-induced flow, their disadvantage is that they are computationally expensive. In this chapter it is argued that for many applications an explicit description of the air flow over waves is needed. To this end a simplified model is developed, which is shown to give a good representation of the wave boundary layer in a negligible calculation time. In the next chapter this simplified model is used for modelling the transport of spray droplets above the waves.

3.1 Introduction

Physical phenomena occurring close to the air–sea interface are determined or strongly influenced by the air-flow dynamics over water waves. To understand and parameterize these phenomena, e.g., the modulation of short wind waves by the air flow and the vertical transport of spray droplets, an explicit description of the air flow over waves is needed. Since Miles (1957), numerous studies have been dedicated to the problem, and brought the understanding that the modulation of the Reynolds stress close to the wave surface is responsible for the peculiarities of the wind–wave interaction (see, e.g., the review by Belcher and Hunt 1998). In the previous chapter, the framework of rapid distortion of turbulence, with which the observed features can be explained theoretically, was outlined. Using this framework, Belcher and Hunt (1993) found an analytical solution for the case of slowly moving waves (as compared to the wind velocity), while Cohen (1997) and Cohen and Belcher (1999)

extended the theory to fast moving waves. Harris et al. (1996) developed a numerical model with an *e*-ε turbulence closure, in which the eddy viscosity was damped exponentially in the outer region.

In the present chapter, a simplified model of the wave boundary layer is presented, which is considered a convenient tool for applied studies that require a detailed description of the structure of the air flow over waves. Examples of such applications are the study of the modulation of short waves by long waves (Kudryavtsev et al. 1997) and the calculation of the transport of sea spray in the air. The latter is illustrated in the next chapter. The simplified model can further be useful to support experimental studies, both in the preparation and measurement stage, whenever the use of computationally expensive numerical models, as described in the previous chapter, is not feasible.

The model calculates the linear perturbations to an undisturbed basic flow, caused by propagating small-amplitude water waves. Waves propagating with arbitrary phase velocity as compared to the wind speed, that is from slow- to fast-moving waves, are treated. As such it differs from the models by Belcher and Hunt (1993) and Cohen and Belcher (1999), in which the air flow over slow- and fast-moving waves was analyzed separately. Following Belcher and Hunt (1993), the main simplification of the problem is achieved by dividing the turbulent air flow into outer and inner regions.

In the outer region (OR), the wave-induced motion experiences an undulation typical for inviscid flow. The description of the OR in the present model is based on the approximate solution of the Rayleigh equation for the vertical velocity suggested by Miles (1957) and Lighthill (1957). The amplitude of the vertical velocity perturbation is proportional to the mean wind speed and decays exponentially with height. The horizontal velocity is found with the same accuracy from the vorticity conservation equation, once the vertical velocity is known. Using this approximate solution in the description of the OR considerably simplifies its analysis compared to the asymptotic solutions by Belcher and Hunt (1993) and Cohen and Belcher (1999).

In the inner region (IR), the dynamics of the wave-induced motion is strongly affected by the turbulent stresses. These stresses are parameterized using eddy-viscosity theory, where the eddy viscosity is obtained from a local balance between production and dissipation of turbulent kinetic energy. The stress is damped exponentially with height, which describes phenomenologically the basic feature of the wave boundary layer: the rapid distortion of turbulence in the OR. Unlike Harris et al. (1996), who introduced damping of the eddy viscosity, we apply damping directly on the stresses (see, also, Cohen and Belcher 1999). The description of the IR is based on the solution of the vorticity equation, in which the existence of the critical layer and the Reynolds stresses is taken into account. In Kudryavtsev et al.

(1999), this equation was solved analytically and explicit equations for the velocity and shear-stress perturbations were obtained. However, these equations appeared to be cumbersome. Aiming at using the model in applied studies, we here solve the vorticity equation in the IR numerically by iterations. Since the numerics is only used as a convenient alternative to the analytical solution method, the model is termed semi-analytical.

The solution of the semi-analytical model is compared in detail with that of the numerical model presented in the previous chapter (the high-*Re* version). The model results are also compared with the laboratory observations performed by Hsu and Hsu (1983). Subsequently, the semi-analytical model is used to investigate the influence of a non-zero angle between wind and wave directions. Note that, unlike in the previous chapter, viscous effects are neglected here. However, at the end of the chapter, an extension that takes into account such effects is presented.

3.2 Linearization of the governing equations

The semi-analytical model uses a wave-following vertical coordinate z defined by $z = x_3 - f(x, x_3)$, where

$$f(x, x_3) = \eta(x) \exp(-kx_3). \tag{3.1}$$

This transformation is chosen such that lines $z = $ const are streamlines of the irrotational flow over the waves. In the coordinate system (x, z), the governing equations, (2.3) and (2.4), can be written as

$$(u - c)(\frac{\partial}{\partial x} - f_1 \frac{\partial}{\partial z})u + w(1 - f_3)\frac{\partial u}{\partial z} = -(\frac{\partial}{\partial x} - f_1 \frac{\partial}{\partial z})P + (1 - f_3)\frac{\partial \tau_{13}}{\partial z}$$
$$+ (\frac{\partial}{\partial x} - f_1 \frac{\partial}{\partial z})(\tau_{11} - \tau_{33}), \tag{3.2}$$

$$(u - c)(\frac{\partial}{\partial x} - f_1 \frac{\partial}{\partial z})v + w(1 - f_3)\frac{\partial v}{\partial z} = (1 - f_3)\frac{\partial \tau_{23}}{\partial z} + (\frac{\partial}{\partial x} - f_1 \frac{\partial}{\partial z})\tau_{12}, \tag{3.3}$$

$$(u - c)(\frac{\partial}{\partial x} - f_1 \frac{\partial}{\partial z})w + w(1 - f_3)\frac{\partial w}{\partial z} = -(1 - f_3)\frac{\partial P}{\partial z} + (\frac{\partial}{\partial x} - f_1 \frac{\partial}{\partial z})\tau_{13}, \tag{3.4}$$

$$(\frac{\partial}{\partial x} - f_1 \frac{\partial}{\partial z})u + (1 - f_3)\frac{\partial w}{\partial z} = 0, \tag{3.5}$$

where $P = p/\rho_a - \tau_{33}$, $f_1 = \partial f/\partial x$, and $f_3 = \partial f/\partial x_3$. Note that the bars above the Reynolds-averaged quantities have been dropped and that, in this chapter, $\tau_{ij} = -\overline{u_i' u_j'}$ is the Reynolds-stress tensor divided by ρ_a.

Since the slope ak of the surface waves is assumed to be small, the air flow can be split into an undisturbed mean flow, or basic flow, and wave-induced perturbations

as expressed in (2.5). In this chapter, the wave-induced perturbations are divided by *ak* for notational convenience. The basic flow velocity field is denoted by capitals: $(U,V,W) = (\langle u \rangle, \langle v \rangle, \langle w \rangle)$. Note that horizontal averaging of the continuity equation gives $W(z) = 0$. For the horizontal components the usual logarithmic profile is assumed:

$$(U(z), V(z)) = \frac{u_*}{\kappa} \ln \frac{z}{z_0} (\cos \theta, \sin \theta), \tag{3.6}$$

where u_* is the friction velocity related to the basic flow. In this chapter, the roughness length z_0 will, unless specified otherwise, be calculated from the Charnock relation (Charnock 1955)

$$z_0 = \alpha_c u_*^2 / g, \tag{3.7}$$

where the Charnock constant α_c is here taken to be 0.014. The idea is then that simulation of the flow over monochromatic waves with phase velocity c resembles the flow over a spectrum of waves for which the phase speed at the spectral peak, c_p, equals c. The roughness length for the latter flow is well described by (3.7). Using the Charnock relation implies that the roughness length indirectly follows from the wind speed, which is often specified at 10-m height and then denoted as U_{10}.

The Reynolds equations can be linearized around the basic flow and take the form

$$U^c \frac{\partial \tilde{u}}{\partial x} + (\tilde{w} - f_1 U^c) U' = -\frac{\partial \tilde{P}}{\partial x} + \frac{\partial \tilde{\tau}_{13}}{\partial z} + \frac{\partial}{\partial x} (\tilde{\tau}_{11} - \tilde{\tau}_{33}), \tag{3.8}$$

$$U^c \frac{\partial \tilde{v}}{\partial x} + (\tilde{w} - f_1 U^c) V' = \frac{\partial \tilde{\tau}_{23}}{\partial z} + \frac{\partial \tilde{\tau}_{12}}{\partial x}, \tag{3.9}$$

$$U^c \frac{\partial \tilde{w}}{\partial x} = -\frac{\partial \tilde{P}}{\partial z} + \frac{\partial \tilde{\tau}_{13}}{\partial x}, \tag{3.10}$$

$$\frac{\partial \tilde{u}}{\partial x} + \frac{\partial}{\partial z} (\tilde{w} - f_1 U^c) = -f_{13} U^c, \tag{3.11}$$

where $U^c = U - c$, $U' = dU/dz$, $V' = dV/dz$, and $f_{13} = \partial^2 f / \partial x \partial x_3$. The boundary conditions of (3.8)–(3.11), written in terms of the wave-induced quantities, are

$$z = z_0: \quad \tilde{u} = kc\eta, \tilde{v} = 0, \tilde{w} = -c\eta_x, \tag{3.12}$$

$$z \to \infty: \quad \tilde{u}, \tilde{v}, \tilde{w} \to 0. \tag{3.13}$$

Vorticity equations, for $\tilde{\Omega}_1 = -\partial \tilde{v}/\partial z$ and $\tilde{\Omega}_2 = \partial \tilde{u}/\partial z - \partial \tilde{w}/\partial x$, can be obtained by eliminating $\tilde{P}$ from (3.8)–(3.11):

$$-U^c \frac{\partial \tilde{\Omega}_1}{\partial x} + (\tilde{w} - f_1 U^c) V'' - f_{13} U^c V' + U' \frac{\partial \tilde{v}}{\partial x} - V' \frac{\partial \tilde{u}}{\partial x} = \frac{\partial^2 \tau_{23}}{\partial z^2} + \frac{\partial^2 \tilde{\tau}_{12}}{\partial x \partial z}, \tag{3.14}$$

$$U^c\frac{\partial\tilde{\Omega}_2}{\partial x} + (\tilde{w} - f_1 U^c)U'' - f_{13}U^c U' = (\frac{\partial^2}{\partial z^2} - \frac{\partial^2}{\partial x^2})\tilde{\tau}_{13} + \frac{\partial^2}{\partial x\partial z}(\tilde{\tau}_{11} - \tilde{\tau}_{33}), \quad (3.15)$$

where $U'' = \mathrm{d}^2 U/\mathrm{d}z^2$, $V'' = \mathrm{d}^2 V/\mathrm{d}z^2$. The vorticity equation (3.15) can be rewritten in the form of the Rayleigh equation for the vertical velocity using the continuity equation (3.11)

$$U^c(\frac{\partial^2 w}{\partial z^2} + \frac{\partial^2 w}{\partial x^2}) - wU'' = -(\frac{\partial^2}{\partial z^2} - \frac{\partial^2}{\partial x^2})\tau_{13} - \frac{\partial^2}{\partial x\partial z}(\tau_{11} - \tau_{33}). \quad (3.16)$$

The governing equations can be solved after the Reynolds stresses have been expressed in terms of the independent variables; that is: a turbulence scheme has to be introduced.

3.3 Simplification of the flow structure

The division of the wave boundary layer into inner and outer regions as described in section 2.3.1 is used to reach the main simplification in the present model. Before it is discussed how this is done, we first pay attention to the role of the critical layer in the turbulent air flow over waves.

3.3.1 The critical layer

The critical layer plays a crucial role in quasi-laminar models of the air flow above waves (Miles 1957). In this type of models it is assumed that the turbulent stresses can be neglected. In the terminology of the rapid distortion theory above waves this assumption is only valid when the height of the critical layer is situated in the outer region. The height z_c of the critical layer was shown in figure 2.1. In the range $U_k/c > 1$, the critical layer is located inside the inner region, so turbulence should influence its dynamics.

Miles (1962) indicated that viscous effects become important and violate the assumption of the quasi-laminar model when the viscous scale of the critical layer,

$$\delta_c = \left(\frac{\nu\kappa z_c}{u_* k}\right)^{1/3}, \quad (3.17)$$

is of order z_c or more, i.e. $\delta_c \geq z_c$. If the critical layer is situated inside the IR, the eddy viscosity takes the role of molecular viscosity in (3.17). In this case an estimate of the height δ_c can be obtained by replacing ν in equation (3.17) by the effective wave-induced eddy viscosity $\widehat{K}_{\mathrm{eff}} = 2\kappa u_* z$ at $z = z_c$ (see equation (3.42), with $\theta = 0$, below). Then equation (3.17) can be written as

$$\delta_c = (2\kappa^2 z_c^2/k)^{1/3}, \quad (3.18)$$

41

and the condition $\delta_c \geq z_c$ is equivalent to

$$kz_c \leq 2\kappa^2. \tag{3.19}$$

Figure 2.1 shows that the conditions $z_c < l$ and $kz_c \leq 2\kappa^2$ are satisfied in the range $U_k/c > 1.3$. It means that in this range turbulence dominates the dynamics of the air flow in the vicinity of the critical height. On the other hand, for $U_k/c < 1$, the critical height rapidly grows and, hence, cannot affect the air-flow dynamics. Thus, it is concluded that the applicability of the quasi-laminar model in the description of the air-flow dynamics is restricted to a narrow range $1 < U_k/c < 1.3$, although in this range the singular behaviour of the critical height will still be suppressed by the weakened turbulence at the top of the inner region.

3.3.2   Outline of the simplified model

The subdivision of the wave boundary layer into inner and outer regions allows considerable simplification of the parameterization of the Reynolds stresses. In the OR the turbulent stresses are simply neglected, and the air flow experiences inviscid undulation. In the IR a simple local eddy-viscosity scheme is used. In this region the air flow is strongly affected by wave-induced variations of the turbulent stresses. The OR and IR were introduced in section 2.3.1 via asymptotic regimes of the wave-induced dynamics. Hence, the height of the boundary, h_{IR}, separating these regions is defined up to an order of magnitude only, i.e. $h_{\mathrm{IR}} \sim l$. In the present model, $h_{\mathrm{IR}} = nl$, where n is a (fixed) constant of $O(1)$. In the following sections, the solution methods for the outer and inner regions are outlined. The solutions in these two regions are constrained by the requirement that the vertical profile of any air-flow variable is continuous at the height $z = h_{\mathrm{IR}}$.

The analysis will be continued in the form of complex amplitudes of the wave-induced perturbations as introduced in equation (2.7). We note that, in this chapter, the complex amplitudes are divided by the (small) slope ak of the wave, in view of the fact that only perturbations of first order in ak are considered. The second small parameter of the problem is the dimensionless depth of the IR, kl. The variable $\widehat{\phi}$ is expanded in powers of kl (for details see Belcher and Hunt 1993; Cohen and Belcher 1999)

$$\widehat{\phi}(z) = \widehat{\phi}_0(z) + kl\widehat{\phi}_1(z) + O(k^2l^2). \tag{3.20}$$

This expansion is valid if $kl \ll 1$. Figure 2.1 shows that this requirement is generally satisfied except for those waves that propagate with a velocity close to the wind speed.

The analysis is done to zero order in kl; this solution will be called the zero-order solution. For the vertical velocity the first-order kl-correction of the zero-

order solution has a significant physical meaning (see section 3.5.4), and will be considered additionally.

3.4 The outer region

3.4.1 Inviscid air flow

When the air flow experiences inviscid undulation over the surface waves, equation (3.16) reduces to the Rayleigh equation

$$U^c \left(\frac{\partial^2 \widehat{w}_0}{\partial z^2} - k^2 \widehat{w}_0 \right) - \widehat{w}_0 U'' = 0, \tag{3.21}$$

with the boundary conditions for the vertical velocity (3.12) and (3.13). This equation was studied in detail in numerous papers starting from Miles (1957). Miles (1957) and Lighthill (1957) suggested an approximate solution of the Rayleigh equation of the form

$$\widehat{w}_0(z) = \gamma U^c(z) e^{-kz}, \tag{3.22}$$

where γ is a constant of proportionality. As was mentioned by Phillips (1977), this constant should have a different value above and below the critical height. At $z < z_c$ the constant must be equal to i to satisfy the boundary condition (3.12). At $z > z_c$ the constant should differ from i due to the expected influence of the critical layer. A direct substitution of (3.22) into equation (3.21) shows that this solution satisfies the Rayleigh equation with the accuracy of $(kz \ln (kz/kz_c))^{-1}$ at large distance from the surface ($kz \sim 1$), and with the accuracy of kz close to the surface ($kz \ll 1$).

The applicability of the estimate (3.22) can be checked through direct comparison of the approximate solution with the 'exact' numerical solution of the Rayleigh equation. Approximation (3.22) is valid with accuracy $a^2 k^2$ in both the wave-following and the Cartesian coordinate systems. In the latter case, z in (3.21) and (3.22) should be replaced by x_3. To test the approximate solution we used a code solving the Rayleigh equation in the Cartesian coordinate system. More detailed results of this numerical model can be found in Komen et al. (1999). In figure 3.1, the approximate and numerical solutions are compared for inverse wave-age parameters $U_{10}/c = 5$ and 2. To fit (3.22) to the numerical solution, the tuning constant γ is chosen as

$$\gamma = \text{i}, \qquad \text{if } x_3 < z_c, \tag{3.23}$$

$$\gamma = \tfrac{1}{2}(1 + \text{i}), \text{ if } x_3 > z_c. \tag{3.24}$$

This choice gives a reasonable agreement between the approximate solution (3.22) and the numerical solution.

43
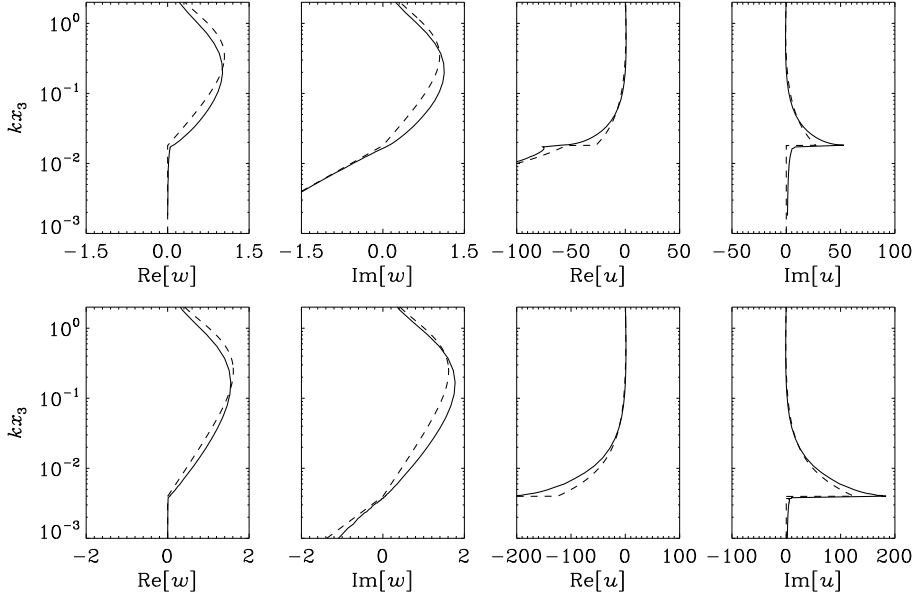
Figure 3.1: Inviscid shear flow: vertical profiles of the real and imaginary parts of the vertical velocity $\widehat{w}$ and the horizontal velocity $\widehat{u}$. ——, numerical solution of the Rayleigh equation (3.21) with the horizontal velocity defined through the continuity equation (2.3); – – –, approximate solution, equations (3.22) and (3.26). The wind speed is $U_{10} = 15$ m s^{-1}. The inverse wave-age parameter is $U_{10}/c = 2$ (upper row), and $U_{10}/c = 5$ (lower row). The velocities are normalized with $aku_*\kappa^{-1}$. The critical height is $kz_c = 0.018$ for $U_{10}/c = 2$, and $kz_c = 0.004$ for $U_{10}/c = 5$.

Notice that, at the critical height, equation (3.22) gives $\mathrm{Re}[\widehat{w}_0](z_c) = 0$. However, in fact $\mathrm{Re}[\widehat{w}_0](z_c)$ is slightly positive. Its value defines the energy transfer from the shear flow to waves in the quasi-laminar theory of Miles (1957). He estimated the magnitude of the vertical velocity at the critical height through the approximate solution (3.22) by integrating equation (3.10) from infinity to z_c, and substituting the resulting relation for the imaginary part of $\widehat{P}$ into equation (3.8)

$$\widehat{w}_0(z_c) = \mathrm{Re}[\gamma]\frac{\kappa kz_c}{u_*}\int_{z_c}^{\infty}(U^c)^2 e^{-kx_3}\mathrm{d}(kx_3). \qquad (3.25)$$

Figure 3.1 also shows the approximate solution for the horizontal velocity in the Cartesian coordinate system, which can be obtained via $\widehat{w}_0$ from the continuity equation 2.3.

$$\widehat{u}_0(x_3) = \mathrm{i}\gamma\left(-U^c + k^{-1}U'\right)e^{-kx_3}. \qquad (3.26)$$

The approximate solution for the horizontal and vertical velocities compares reasonably well with the numerical solution. This comparison illustrates the possibility to describe the structure of the wave-induced velocity field in the inviscid air flow by the approximate solution (3.22).

3.4.2 Approximate solution for the outer region

The turbulent stresses in the outer region are not correlated with the surface waves. Hence the vertical wave-induced motion in the outer region should be close to that of the inviscid air flow. That gives us the possibility to apply approximation (3.22) of $\widehat{w}_0$ for the description of the OR in the turbulent boundary layer. However, in section 3.3.1, it was argued that the singular behaviour of the critical layer dynamics is significantly suppressed by turbulence. This means that the constant γ in the approximate solution (3.22) should be uniform throughout the whole wave boundary layer, without a singularity at z_c. Taking into account the boundary condition (3.12), we suggest that the vertical motion in the OR is described by equation (3.22) throughout the whole wave boundary layer, i.e.:

$$\widehat{w}_0(z) = iU^c(z)e^{-kz}. \tag{3.27}$$

This solution describes the basic behaviour of the wave-induced vertical motion, namely its decay with height, in the turbulent wave boundary layer. It can be shown that this solution is correct only in zero order while the Reynolds stresses inside the IR induce a vertical velocity that is of kl-order (Belcher and Hunt 1993). To obtain the solution of $\widehat{u}_0$ with the same accuracy as $\widehat{w}_0$, we use the inviscid form of the vorticity equation (3.15). In terms of normal modes this equation has the form

$$ikU^c\left(\frac{\partial\widehat{u}_0}{\partial z} - ik\widehat{w}_0\right) + (\widehat{w}_0 - iU^c e^{-kz})U'' + ike^{-kz}U^cU' = 0. \tag{3.28}$$

Substituting (3.27) for $\widehat{w}_0$ into the vorticity equation and integrating the obtained expression for $\partial\widehat{u}_0/\partial z$ from ∞ to z with the boundary condition $\widehat{u}_0(\infty) = 0$, we obtain the following approximate solution for the horizontal velocity

$$\widehat{u}_0(z) = U^c e^{-kz} + 2\int_z^\infty e^{-kz'}U'\mathrm{d}z'. \tag{3.29}$$

Likewise, substitution of (3.27) into the inviscid form of (3.14) with application of the boundary conditions gives

$$\widehat{v}_0(z) = 0. \tag{3.30}$$

Thus, the general features of the wave-induced motion in the outer region are described by equations (3.27), (3.29), and (3.30). This is the zero-order solution

in the sense of expansion (3.20). The *kl*-order correction of the solution for the horizontal motion does not introduce new essential elements in the description of the horizontal velocity in the OR. However, the *kl*-order correction of the vertical velocity is important as $\text{Re}[\widehat{w}]$ determines the energy transfer from wind to waves, and will be considered later.

3.5 The inner region

3.5.1 Reynolds stresses

In the IR the Reynolds stresses are in equilibrium with the local velocity gradient. Consequently, they can be described by the local eddy-viscosity closure scheme

$$\tau_{13} = K\left(\frac{\partial u}{\partial z} + \frac{\partial w}{\partial x}\right), \tag{3.31}$$

$$\tau_{23} = K\frac{\partial v}{\partial z}, \tag{3.32}$$

$$\tau_{12} = K\frac{\partial v}{\partial x}. \tag{3.33}$$

Here, K is the eddy-viscosity, which is expressed via the square root of the turbulent kinetic energy (TKE), e, and the turbulence length scale, which is proportional to the distance from the surface

$$K = \kappa z e^{1/2}. \tag{3.34}$$

The normal Reynolds stresses in the IR are assumed to be proportional to the shear stress:

$$\tau_{11} = -\alpha_u\left(\tau_{13}^2 + \tau_{23}^2\right)^{1/2}, \tag{3.35}$$

$$\tau_{22} = -(\alpha_v/\alpha_u)\tau_{11}, \tag{3.36}$$

$$\tau_{33} = -(\alpha_w/\alpha_u)\tau_{11}, \tag{3.37}$$

where α_u, α_v, and α_w are empirical constants (Townsend 1972). The shear stress can be found from the TKE conservation equation, in which a local balance between the production and dissipation of TKE is assumed

$$\tau_{13}\frac{\partial u}{\partial z} + \tau_{23}\frac{\partial v}{\partial z} = \frac{e^{3/2}}{\kappa z}. \tag{3.38}$$

Inside the IR, the wave-induced variation of the vertical gradient of the horizontal velocity components is $(kl)^{-1}$ times larger than the variation of the horizontal gradient of the vertical velocity. In *kl*-order, the linearized equation (3.38) written in

terms of normal modes is

$$\widehat{K}\left[(U')^2 + (V')^2\right] + 2\langle K \rangle \left(U'\frac{\partial \widehat{u}}{\partial z} + V'\frac{\partial \widehat{v}}{\partial z}\right) = \frac{3\langle K \rangle^2 \widehat{K}}{(\kappa z)^4}. \tag{3.39}$$

The solution of this equation with $\langle K \rangle = \kappa u_* z$ is

$$\widehat{K} = (\kappa z)^2 \left(\frac{\partial \widehat{u}}{\partial z}\cos\theta + \frac{\partial \widehat{v}}{\partial z}\sin\theta\right). \tag{3.40}$$

Subsequently, the complex amplitude of the shear stress, $\widehat{\tau}_{13}$, can be derived from (3.31) and (3.40) by

$$\widehat{\tau}_{13} = \widehat{K}U' + \langle K \rangle \frac{\partial \widehat{u}}{\partial z}, \tag{3.41}$$

and similarly for $\widehat{\tau}_{23}$ (note that $\widehat{\tau}_{12}$ is a kl-order smaller). This leads to relations that are valid well inside the IR (at $z < l$). According to rapid distortion theory, the shear stress attenuates towards the outer region. To take this effect into account we introduce a vertical damping, $\exp(-z/l)$, of the shear stresses. This, finally, gives

$$\widehat{\tau}_{13} = \kappa z u_* \left(\frac{\partial \widehat{u}}{\partial z}(1 + \cos^2\theta) + \frac{\partial \widehat{v}}{\partial z}\cos\theta\sin\theta\right)e^{-z/l}, \tag{3.42}$$

$$\widehat{\tau}_{23} = \kappa z u_* \left(\frac{\partial \widehat{v}}{\partial z}(1 + \sin^2\theta) + \frac{\partial \widehat{u}}{\partial z}\cos\theta\sin\theta\right)e^{-z/l}. \tag{3.43}$$

3.5.2 Vorticity equation in the IR

The vorticity equations (3.14) and (3.15) are the basis of the semi-analytical model in the IR. These equations will be simplified and rewritten in a more tractable form. The procedure is illustrated here for the case that the wind blows in wave direction, i.e. $\theta = 0°$, so that equation (3.14) does not have to be considered. First, the dimensionless vertical coordinate ζ is introduced,

$$\zeta = z/l, \tag{3.44}$$

and (3.15) is rewritten in terms of normal modes, accounting for the shear and normal stresses:

$$\mathrm{i}U^c\left(\frac{\partial \widehat{u}}{\partial \zeta} - \mathrm{i}kl\widehat{w}\right) + \frac{1}{kl}(\widehat{w} - \mathrm{i}e^{-kl\zeta}U^c)U''_{\zeta\zeta} + \mathrm{i}e^{-kl\zeta}U^c U'_\zeta =$$
$$|U^c_l|\left[\frac{\partial^2}{\partial \zeta^2} + (kl)^2 - \mathrm{i}kl(\alpha_u - \alpha_w)\frac{\partial}{\partial \zeta}\right]\left(\zeta e^{-\zeta}\frac{\partial \widehat{u}}{\partial \zeta}\right), \tag{3.45}$$

47

where $U'_\zeta = \mathrm{d}U/\mathrm{d}\zeta$ and $U''_{\zeta\zeta} = \mathrm{d}^2U/\mathrm{d}\zeta^2$. The continuity equation (3.11) in the ζ-coordinate reads

$$\mathrm{i}kl\widehat{u} + \frac{\partial \widehat{w}}{\partial \zeta} - \mathrm{i}\mathrm{e}^{-kl\zeta}U'_\zeta = 0. \tag{3.46}$$

Figure 2.1 shows that kl is small except in a narrow range around $U_k/c \approx 1$. Outside this narrow range, the terms of kl-order can be neglected in equation (3.45), which then takes the form

$$\frac{\partial^2}{\partial \zeta^2}\left(\zeta \mathrm{e}^{-\zeta}\frac{\partial \widehat{u}_0}{\partial \zeta}\right) - \mathrm{i}\frac{U^c}{|U^c_l|}\frac{\partial \widehat{u}_0}{\partial \zeta} = S(\zeta), \tag{3.47}$$

where the function $S(\zeta)$ describes the source of vorticity caused by the vertical motion in the shear flow:

$$\begin{aligned}
S(\zeta) &= |U^c_l|^{-1}\left[(kl)^{-1}(\widehat{w} - \mathrm{i}\mathrm{e}^{-kl\zeta}U^c)U''_{\zeta\zeta} + \mathrm{i}\mathrm{e}^{-kl\zeta}U^cU'_\zeta\right] \\
&= |U^c_l|^{-1}\left[\widehat{w}_1 U''_{\zeta\zeta} + \mathrm{i}\mathrm{e}^{-kl\zeta}U^cU'_\zeta\right].
\end{aligned} \tag{3.48}$$

To obtain the second equality, the expansion (3.20) in powers of kl for the vertical velocity is used, where $\widehat{w}_0$ is defined by (3.27) and $\widehat{w}_1$ is the kl-order correction, which can be found from the continuity equation (3.46) given the zero-order solution $\widehat{u}_0$ for the horizontal velocity:

$$\widehat{w}_1(\zeta) = -\mathrm{i}\int_{\zeta_0}^{\zeta}(\widehat{u}_0 - U^c\mathrm{e}^{-kl\zeta'})\mathrm{d}\zeta'. \tag{3.49}$$

3.5.3 Solution for the inner region

It is more convenient to rewrite equation (3.47) as

$$\frac{\partial^2\widehat{\tau}_0}{\partial \zeta^2} - \mathrm{i}\frac{U^c}{|U^c_l|}\frac{\mathrm{e}^\zeta}{\zeta}\widehat{\tau}_0 = 2\kappa u_* S(\zeta), \tag{3.50}$$

where $\widehat{\tau}_0 = 2\kappa u_* \zeta \mathrm{e}^{-\zeta}\partial\widehat{u}_0/\partial\zeta$ is the shear stress variation in the case of $\theta = 0°$. Equation (3.50) is an ordinary non-uniform differential equation of the second order with respect to the shear stress $\widehat{\tau}_0$, or of the third order with respect to the horizontal velocity $\widehat{u}_0$. The boundary conditions have to be specified. At the upper boundary of the IR, $\zeta = n$ (in the present study we adopt $n = 3$), the solution of the equation has to match the horizontal velocity $\widehat{u}_n$ and its vertical gradient in the OR, i.e.:

$$\widehat{u}_0(n) = \widehat{u}_n, \tag{3.51}$$

$$\widehat{\tau}_0(n) = 2\kappa u_* n\mathrm{e}^{-n}\left.\frac{\partial \widehat{u}}{\partial \zeta}\right|_{\zeta=n}. \tag{3.52}$$

At the lower boundary, $\zeta = \zeta_0 \equiv z_0/l$, the solution of (3.50) has to match the horizontal component of the orbital velocity of the surface wave, $\widehat{u}_s = c$,

$$\widehat{u}_0(\zeta_0) = \widehat{u}_s. \tag{3.53}$$

Accounting for the boundary condition (3.53), the relation between the wave-induced variation of the shear stress, $\widehat{\tau}_0$, and the wind velocity $\widehat{u}_0$ is

$$\widehat{u}_0(\zeta) = \widehat{u}_s + \frac{1}{2\kappa u_*} \int_{\zeta_0}^{\zeta} \widehat{\tau}_0(\zeta') e^{\zeta'} d\ln\zeta'. \tag{3.54}$$

At small ζ, in the lower part of the IR, the shear stress is approximately constant with height (for example, see figure 3.4). Hence, the profile of the velocity variation has a logarithmic shape according to (3.54). This thin sublayer adjacent to the surface is usually referred to as the inner surface layer (Belcher and Hunt 1993). The magnitude of the shear stress at the surface, $\widehat{\tau}_0(\zeta_0)$, is unknown, and should be found so that the solution of equation (3.50) with the upper boundary condition (3.52) obeys the condition

$$\widehat{u}_n - \widehat{u}_s = \frac{1}{2\kappa u_*} \int_{\zeta_0}^{n} \widehat{\tau}_0(\zeta') e^{\zeta'} d\ln\zeta'. \tag{3.55}$$

Equation (3.50), with the upper boundary condition (3.52) and integral condition (3.55), forms a coupled system with equation (3.49) for the *kl*-order correction of the vertical velocity, $\widehat{w}_1$, which is present in the vorticity source S, given by (3.48). These coupled equations can be solved analytically, as was presented by Kudryavtsev et al. (1999). However, the simplest way to obtain the solution is to use an iterative method, which is done in the present study. We note that both procedures give exactly the same solutions. The following procedure is applied here: (1) a first guess for $\widehat{\tau}_0$ at $\zeta = \zeta_0$ is made; (2) equation (3.50) with the upper boundary condition (3.52) and lower boundary condition $\widehat{\tau}_0(\zeta_0)$ is solved numerically; (3) the resulting shear-stress profile is integrated over the IR according to the right hand side of (3.55), which results in an estimate of the horizontal velocity difference over the IR, $\Delta\widehat{u}_0$; (4) depending on the difference between $\Delta\widehat{u}_0$ and the true value $(\widehat{u}_n - \widehat{u}_s)$, $\widehat{\tau}_0$ is corrected and the iteration is repeated from step (2). The iterations are continued until $|\Delta\widehat{u}_0 - (\widehat{u}_n - \widehat{u}_s)| / |\widehat{u}_n - \widehat{u}_s|$ is small enough. Then $\widehat{w}_1(\zeta)$ in (3.49) is updated with the new $\widehat{u}_0$ and the iteration starts again. The profile of the horizontal velocity is found from (3.54).

3.5.4 Vertical velocity

The *kl*-order correction of the vertical velocity, $\widehat{w}_1$, has an important physical meaning. It gives the real part of the vertical velocity, which determines the energy flux

to the waves. The vertical velocity correlated with the wave elevation produces the slope-correlated variation of the pressure. The pressure correlated with the wave slope finally provides the energy transfer from the air flow to the waves.

The first-order solution for $\widehat{w}_1$ inside the IR follows from equation (3.49) with $\widehat{u}_0$ defined by (3.54). However, this solution does not provide the attenuation of the vertical velocity above the IR. It is clear that such a behaviour of the vertical velocity is not physical, which is explained by the fact that the solution for $\widehat{u}_0$ used in (3.49) is valid for small kz only, i.e. inside the IR. Outside the IR, all wave-induced variables of the air flow decay exponentially with height. To account for this fact, an exponential decay is introduced in equation (3.49), which then takes the form

$$\widehat{w}_1(\zeta) = -\mathrm{i}\mathrm{e}^{-kl\zeta} \int_{\zeta_0}^{\zeta}(\widehat{u}_0 - U^c\mathrm{e}^{-kl\zeta'})\mathrm{d}\zeta'. \tag{3.56}$$

Equation (3.56) helps to understand the mechanism of wave generation (see a review by Belcher and Hunt 1998). The imaginary part of the horizontal velocity, produced by the action of the shear stress inside the IR, generates the real part of the vertical velocity, which is in phase with the wave elevation. This velocity penetrates into the inviscid OR and generates the slope-correlated pressure. The pressure then penetrates the thin IR and forms, at the surface, the energy flux from the air flow to the waves.

3.5.5   The case of arbitrary angle

Above, the solution procedure has been outlined for the case $\theta = 0°$. When the wind and wave directions are not the same, the equations become more extensive, but the same procedure can be applied. Inserting the relations for the shear stress, (3.42) and (3.43), in the vorticity equations (3.15) and (3.14) yields

$$\frac{1+\cos^2\theta}{2} \frac{\partial^2}{\partial\zeta^2}\left(\zeta\mathrm{e}^{-\zeta}\frac{\partial\widehat{u}_0}{\partial\zeta}\right) - \mathrm{i}\frac{U^c}{|U_l^c|}\frac{\mathrm{e}^{\zeta}}{\zeta}\left(\zeta\mathrm{e}^{-\zeta}\frac{\partial\widehat{u}_0}{\partial\zeta}\right) =$$

$$\frac{1}{|U_l^c|}\left(\widehat{w}_1 U_{\zeta\zeta}'' + \mathrm{i}\mathrm{e}^{-kl\zeta}U^c U_\zeta'\right) - \frac{\cos\theta\sin\theta}{2}\frac{\partial^2}{\partial\zeta^2}\left(\zeta\mathrm{e}^{-\zeta}\frac{\partial\widehat{v}_0}{\partial\zeta}\right), \tag{3.57}$$

and

$$\frac{1+\sin^2\theta}{2} \frac{\partial^2}{\partial\zeta^2}\left(\zeta\mathrm{e}^{-\zeta}\frac{\partial\widehat{v}_0}{\partial\zeta}\right) - \mathrm{i}\frac{U^c}{|U_l^c|}\frac{\mathrm{e}^{\zeta}}{\zeta}\left(\zeta\mathrm{e}^{-\zeta}\frac{\partial\widehat{v}_0}{\partial\zeta}\right) =$$

$$\frac{1}{|U_l^c|}\left(\widehat{w}_1 V_{\zeta\zeta}'' + \mathrm{i}(\mathrm{e}^{-kl\zeta}U^c - \widehat{u}_0)V_\zeta' + \mathrm{i}U_\zeta'\widehat{v}_0\right) - \frac{\cos\theta\sin\theta}{2}\frac{\partial^2}{\partial\zeta^2}\left(\zeta\mathrm{e}^{-\zeta}\frac{\partial\widehat{u}_0}{\partial\zeta}\right), \tag{3.58}$$

where $V'_\zeta = \mathrm{d}V/\mathrm{d}\zeta$ and $V''_{\zeta\zeta} = \mathrm{d}^2V/\mathrm{d}\zeta^2$. The term $\mathrm{i}U'_\zeta \widehat{v}_0$ in (3.58) appears to be small and can thus be retained in the right-hand side of this equation. The procedure to solve the equations is essentially the same as described above. Equations (3.57) and (3.58) are solved by turns, and every turn $\widehat{w}_0$ is updated using equation (3.56). The boundary conditions for (3.58) are given by: $\widehat{v}_0(\zeta_0) = \widehat{v}_0|_{\zeta=n} = \partial\widehat{v}_0/\partial\zeta|_{\zeta=n} = 0$.

3.6 Results

3.6.1 Velocity and shear-stress profiles

In this section we present a comparison of the wave-induced velocity and the Reynolds stress calculated by the semi-analytical model with those calculated by the numerical model presented in the previous chapter (the high-*Re* version). A

Run	U_{10}/c	c/u_*	kz_c	kl	kz_0
1	0.83	36.6	32.8	0.05	1.4×10^{-6}
2	1.66	18.3	8.5×10^{-2}	0.28	5.5×10^{-5}
3	5	6.1	5.7×10^{-3}	0.11	5.0×10^{-4}
4	1.5	15.9	–	0.03	5.6×10^{-5}

Table 3.1: Parameters of four representative runs.

comparison is made for four cases specified by the parameters listed in table 3.1. Here, we consider only cases in which the wind and wave directions are aligned; in section 3.7.1, the case of an arbitrary angle between the directions is investigated. For the first three runs, the wave propagates in the wind direction, while, in run four, the wave propagates against the wind.

To enable the comparison, the numerical-model results have been transformed to the present *z*-coordinate. Figures 3.2–3.5 show the vertical profiles of the velocity and the Reynolds shear stress. The IR depth and the critical height are also indicated in these figures.

In the outer region $(z > l)$, the wave-induced motion is defined mainly by the elevation-correlated (real part) component of the horizontal velocity and the slope-correlated (imaginary part) component of the vertical velocity, which characterize the inviscid nature of the flow above the wavy surface. Their quadrature components $(\mathrm{Im}[\widehat{u}]$ and $\mathrm{Re}[\widehat{w}]$, respectively) are small. Notice that in the OR the approximate solution of the semi-analytical model, based on equations (3.27) and (3.29), is in excellent agreement with the numerical model for all four runs.
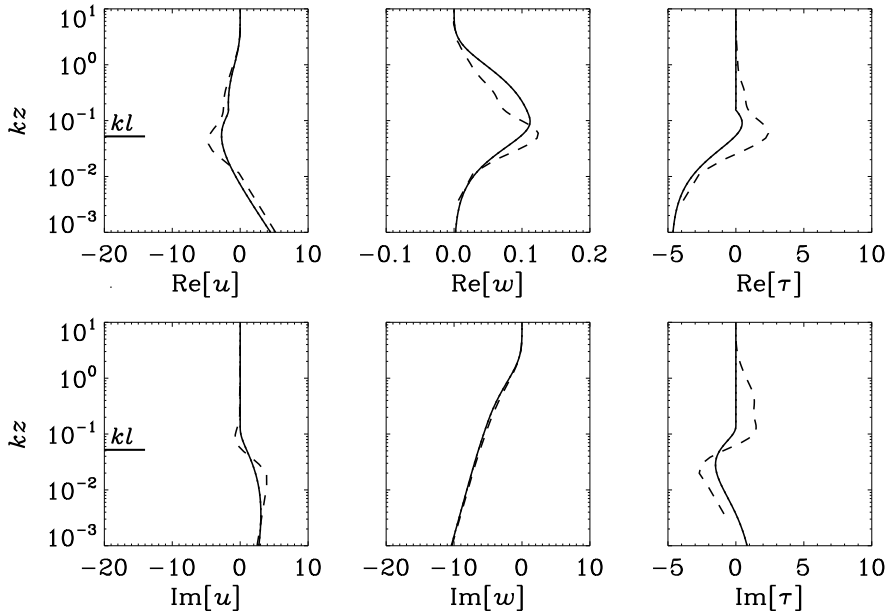
Figure 3.2: Vertical profiles of the real and imaginary parts of the horizontal velocity $\widehat{u}$ (left column), the vertical velocity $\widehat{w}$ (middle column), and the shear stress $\widehat{\tau}$ (right column): ——, semi-analytical model; $---$, numerical model. The inverse wave age is $U_{10}/c = 0.83$. The velocities are normalized with $aku_*\kappa^{-1}$ and the shear stress is normalized with aku_*^2.

Run 1 (figure 3.2) is related to waves in the vicinity of the spectral peak of a fully developed sea (inverse wave age $U_{10}/c = 0.83$). In this case the critical height is located outside the wave boundary layer, so that the influence of the critical layer on the air-flow dynamics is absent. The dynamics of the OR is mainly defined by the inviscid undulations over the wavy surface, while the structure of the IR is fully determined by the action of the shear stress. At the surface, the stress provides the matching of the air-flow velocities to the orbital velocities of the wave. This results in the generation of the slope-correlated horizontal velocity inside the IR, and hence, through the continuity equation, the elevation-correlated component of the vertical velocity. The latter is of *kl*-order and small but plays a crucial role in the energy exchange between wind and waves. The vertical profiles of the shear stress obtained by the semi-analytical and the numerical models are in qualitative and quantitative agreement. Both models predict a strong enhancement of the surface stress in the region of the wave trough.

Run 2 (figure 3.3) corresponds to a case where the frequency of the wave is
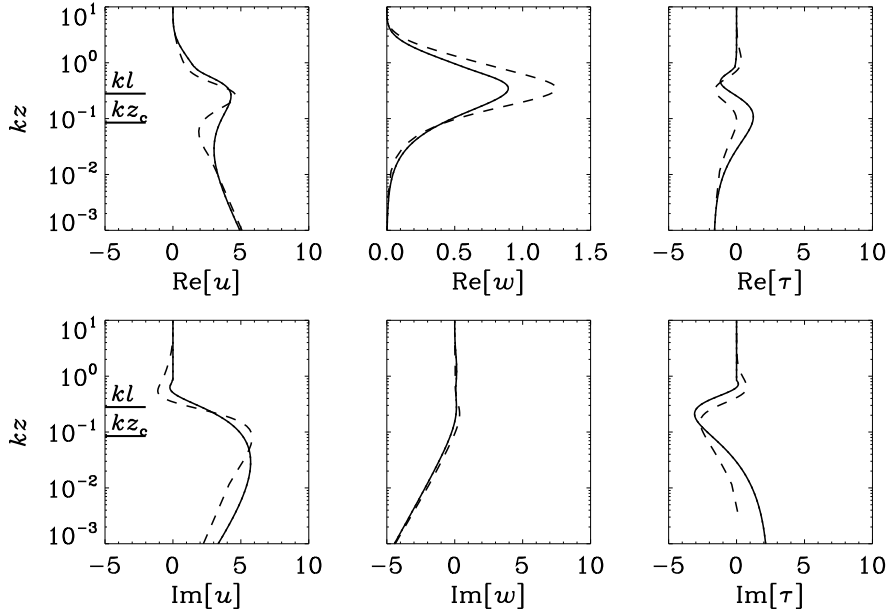
Figure 3.3: The same as in figure 3.2 but for $U_{10}/c = 1.66$.

twice the frequency of the spectral peak of a fully developed sea (inverse wave age is $U_{10}/c = 1.66$). In this case the height of the IR is $kl = 0.28$, which is close to its maximal value, as follows from figure 2.1. The height of the critical layer is $kz_c = 0.085$. This is comparable to the IR height, which could give rise to complication. The accuracy of our approximation is of kl-order, and one could anticipate a significant deviation of the semi-analytical solution from the numerical-model solution. However, the comparison is encouraging. The local maximum in $\mathrm{Re}[\widehat{u}]$ and the local minimum in $\mathrm{Re}[\widehat{\tau}]$, both occurring in the vicinity of the critical layer, are well reproduced by the semi-analytical model. Notice that, since the critical layer is located inside the IR, the singular behavior of the air-flow dynamics, which is clearly visible in the upper row of figure 3.1, is significantly blurred by turbulent stresses.

Run 3 (figure 3.4) corresponds to the case of a slow wave (inverse wave age $U_{10}/c = 5$). Again a good agreement of the velocity distribution between the models is found. The structure of the IR is characterized by a speed-up of the horizontal velocity over the crest. The action of the shear stress shifts the maximum of the horizontal velocity upwind of the crest (positive $\mathrm{Im}[\widehat{u}]$). Both models predict the maxima of $\mathrm{Re}[\widehat{u}]$, $\mathrm{Im}[\widehat{u}]$, and $\mathrm{Re}[\widehat{w}]$ in the vicinity of the IR height. The numerical model gives a somewhat stronger acceleration of the flow than the semi-analytical
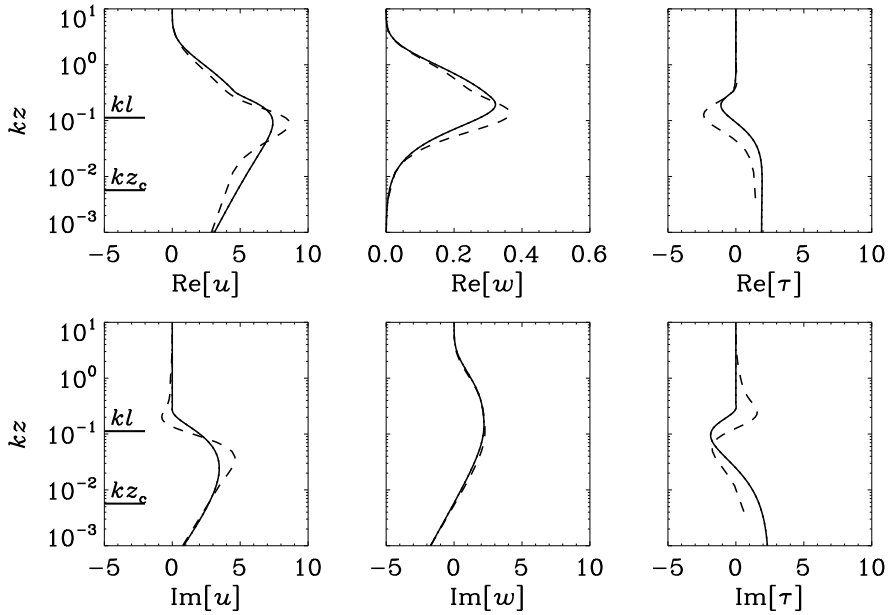
Figure 3.4: The same as in figure 3.2 but for $U_{10}/c = 5$.

model. The vertical profile of the shear stress is in qualitative agreement, though the local extremum in $\text{Re}[\hat{\tau}]$ seems to be underestimated by the semi-analytical model. Furthermore, unlike the semi-analytical model, the numerical model predicts the existence of the slope-correlated stress $\text{Im}[\hat{\tau}]$ in the OR. The critical layer for this run is located in the lower part of the IR, where the shear stress dominates the air-flow dynamics, and there is no manifestation of the singular behavior of the air flow at the critical height.

Finally, run 4 (figure 3.5) is related to a case of swell propagating against the wind. In this case, there is again a speed-up of the horizontal velocity over the crest but, because this speed-up is relative to the mean wind direction, it appears as a maximum over the trough of the wave (negative $\text{Re}[\hat{u}]$). The shift of the horizontal velocity maximum towards the upwind side of the crest now appears as a positive $\text{Im}[\hat{u}]$, and the maximum of the shear stress is located in the vicinity of the wave trough. The simplified description of the turbulent wave boundary layer agrees well with the one obtained by the numerical model.

The results presented above show that the semi-analytical model correctly reproduces the general peculiarities of the air-flow dynamics over surface waves in a wide range of wind–wave conditions as compared to the numerical model.
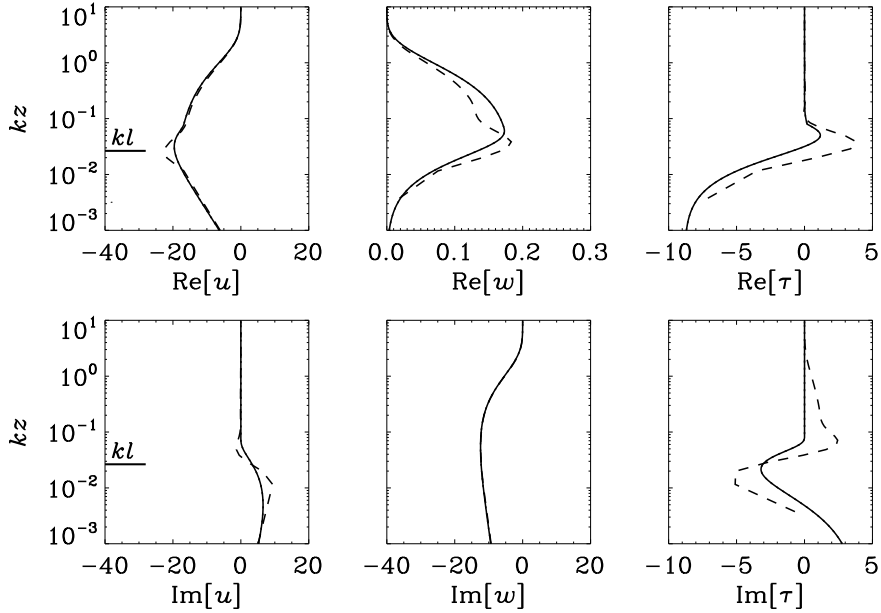
54

Figure 3.5: The same as in figure 3.2 but for a wave propagating against the wind ($\theta = 180°$). The inverse wave age is $U_{10}/c = 1.5$.

3.6.2 Growth-rate parameter

The growth-rate parameter β is found from equation (2.24), in which the imaginary part of the pressure at the surface is calculated using

$$\mathrm{Im}[\widehat{P}(z_0)] = \int_{kz_0}^{\infty} (U^c \mathrm{Re}[\widehat{w}_1] - \mathrm{Re}[\widehat{\tau}_{13}]) \, dkz. \tag{3.59}$$

In figure 3.6, a comparison of the growth-rate parameter resulting from the semi-analytical and the numerical models is shown.

Qualitatively, the semi-analytical model reproduces well the growth rate dependence on c/u_* resulting from the numerical model. Quantitatively, the former model gives somewhat lower values of β for waves moving slower than the wind speed. This is explained by the fact that the semi-analytical model predicts a smaller magnitude of the vertical velocity $\mathrm{Re}[\widehat{w}]$ (see figures 3.3 and 3.4) and hence $\mathrm{Im}[\widehat{P}(z_0)]$ than the numerical model. In the range $15 < c/u_* < 22$, the growth-rate parameter has a peak. Its origin can be explained by the fact that the critical height here approaches the upper boundary of the IR, and peculiarities of the critical layer dynamics, though still suppressed by weakened turbulence, become important. In the
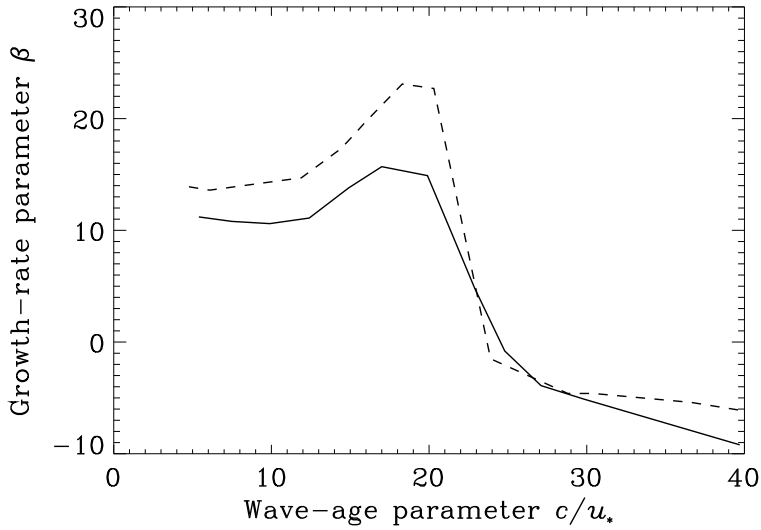
Figure 3.6: The growth-rate parameter as a function of c/u_*: ———, semi-analytical model; $---$, numerical model.

range of fast waves the growth rate parameter is negative, which means that the energy flux is from the waves to the air. Note that the simplified model predicts a higher damping rate, corresponding with a larger amplitude of $\mathrm{Re}[\widehat{w}]$ (see figure 3.2).

3.6.3 Comparison with measurements

In this section, the model results are compared with the laboratory observations of velocity and stress profiles over a mechanically generated wave performed by Hsu and Hsu (1983). The air velocity was measured with X-wires mounted on a vertically moving wave follower to enable observations very close to the surface. The wave phase velocity was $c = 1.6$ m s^{-1} and the steepness $ak \approx 0.11$. Other param-

Run	U_∞ [m s^{-1}]	$u_{*,\mathrm{exp}}$ [m s^{-1}]	U_k [m s^{-1}]	u_* [m s^{-1}]	U_k/c
1	1.37	0.043	1.4	0.06	0.87
2	2.12	0.073	2.0	0.08	1.28
3	2.92	0.110	2.9	0.13	1.84

Table 3.2: Parameters of three runs of the experiment by Hsu and Hsu (1983).

eters of three runs of this experiment are shown in table 3.2. Mastenbroek (1996) already compared his numerical model results with these experimental data. For the comparison, values of U_k (the mean horizontal wind speed at $z = k^{-1}$) and u_* were determined by fitting a logarithmic profile to the observed mean wind speed. The resulting values for the friction velocity are somewhat higher than the values $u_{*,\mathrm{exp}}$ presented by Hsu and Hsu.
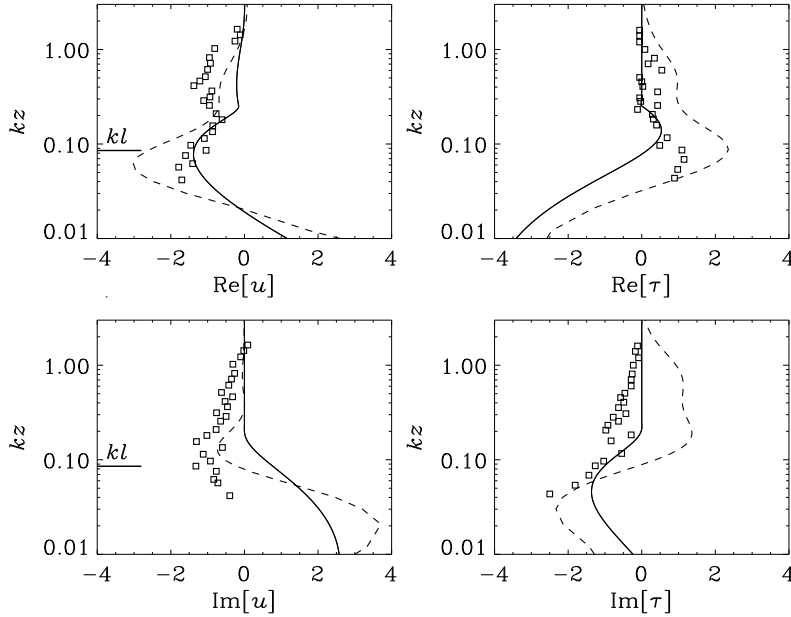
Figure 3.7: Vertical profiles of the real and imaginary parts of the horizontal velocity $\hat{u}$ (left column) and the shear stress $\hat{\tau}$ (right column) as measured by Hsu and Hsu (1983), run 1 ($U_k = 1.4$ m s^{-1}; $U_k/c = 0.87$): □, observations; ———, semi-analytical model; $---$, numerical model. The horizontal velocity is normalized with $aku_*\kappa^{-1}$ and the shear stress with aku_*^2.

Figures 3.7–3.9 show the vertical profiles of the wave-induced horizontal velocity and the shear stress. The model results are presented in the vertical coordinate z of the semi-analytical model, which is very similar to the vertical coordinate of the wave follower. The vertical velocity is not shown in the figures as there is an apparent bias in these data of which the cause is unknown (Mastenbroek 1996).

In runs 1 and 2 the wave moves somewhat slower and faster than the wind, respectively; run 3 represents a slowly propagating wave. In runs 1 and 3 the measurements were done both in the outer and the inner regions, while in run 2 the IR
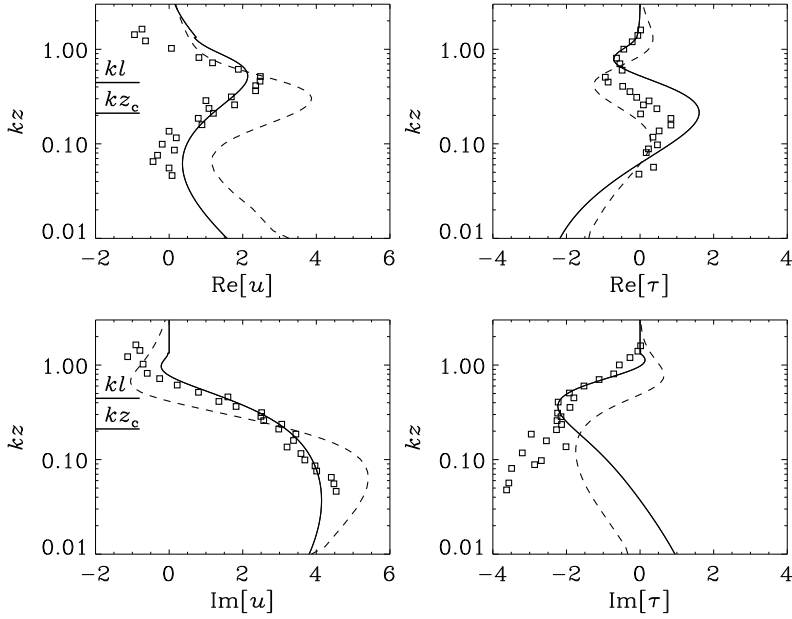
Figure 3.8: The same as in figure 3.7 but for run 2: $U_k = 2.0$ m s^{-1}, $U_k/c = 1.28$.

depth is large, and most of the data are confined to the inner region. The experimental data confirm the existence of the outer and the inner regions. For runs 1 and 3 no significant variation of the shear stress is observed inside the OR, while inside the IR a systematic trend in the shear stress is clearly seen. In run 2 the shear stress varies throughout the whole domain. Peculiarities of the wave-induced horizontal velocity are dependent on the ratio of the wind speed to the wave phase velocity. If the wave runs faster than the wind, then the air flow accelerates over the trough (run 1). Otherwise, the air flow accelerates over the crest (runs 2 and 3). The larger the speed difference between wind and wave, the stronger the acceleration.

The semi-analytical model reproduces the behavior of the wave-induced velocity and stress perturbations above the wave well, except for the lower part of the vertical profile of Im$[\hat{\tau}]$. The reason for this is unclear. However, the numerical model suffers from the same deficiency. In fact, it is not possible to judge which of the two models behaves better as compared to the measurements.

Figure 3.9: The same as in figure 3.7 but for run 3: $U_k = 2.9$ m s^{-1}; $U_k/c = 1.84$.

3.7 Influence of specific parameters

In this section, the semi-analytical model is used in order to assess the impact of two specific parameters on the flow. First, the dependence on the angle between the wind and wave directions is investigated. The model as described so far is general enough for this purpose. Second, the case of low Reynolds numbers is considered, which requires some modifications.

3.7.1 Angle between wind and waves

So far we have focussed on cases in which the wind and wave directions are aligned. Now, attention will be paid to the more general case of an arbitrary angle, θ, between wind and wave directions. Knowledge about the dependence of the growth rate on θ for a wide range of wave lengths is relevant for different applications. In wave prediction models this largely determines the angular spreading of the energy containing waves. In wind–wave coupling models, the angular distribution of short waves influences the resulting sea drag.

In most existing parameterizations, $\gamma = \dot{E}/E$ is proportional to $\cos\theta$ (e.g., Plant

1982; Snyder et al. 1981). These are, however, based on experimental data with limited variation in wind–wave angle. Numerical calculations of the angular dependence of air flow over waves have been reported by Townsend (1972), Burgers and Makin (1993), Mastenbroek (1996), and, recently, Li et al. (2000). These studies contrast with the above mentioned parameterizations and point towards a $\cos^2 \theta$-dependence of the growth rate.
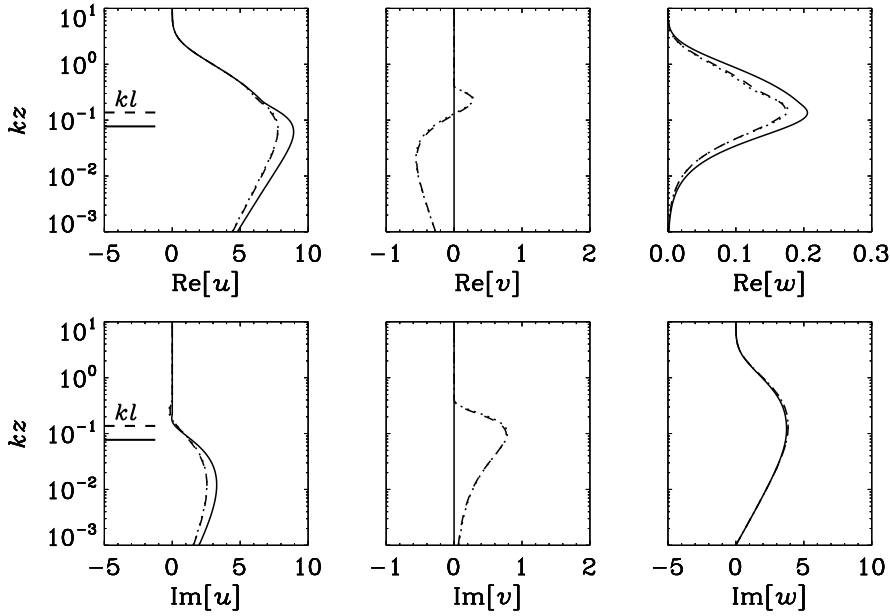
Figure 3.10: Vertical profiles of the real and imaginary parts of the wave-induced amplitudes of $\widehat{u}$ (left panels), $\widehat{v}$ (middle panels), and $\widehat{w}$ (right panels). The amplitudes are scaled with $aku_* \kappa^{-1} \cos \theta$. The inverse wave age parameter is: $u_* \cos \theta / c = 0.18$ ($U_k/c = 4$). The meaning of the lines is: ———, $\theta = 0°$, $- - -$, $\theta = 60°$, and $\cdots$, $\theta = 60°$ but no $\widehat{v}$ term in equation (3.57). A fixed dimensionless roughness length, $kz_0 = 10^{-4}$, is employed.

Figure 3.10 shows results of model simulations for a relatively slowly moving wave ($U_k/c = 4$). Plotted are the vertical profiles of the wave-induced amplitudes of the three velocity components. The solid line represents a run with $\theta = 0°$. The typical features of the flow over a slow wave were outlined in section (see figure 3.4).

The dashed line shows a run with the same value of U_k/c but with $\theta = 60°$; this corresponds to adding a transverse component to the mean wind speed. It is observed that a transverse wave-induced flow develops, but the amplitude $\widehat{v}$ is very small compared to $\widehat{u}$. The flow in wave direction is affected by the presence of a transverse mean wind. However, when the wave-induced amplitudes are properly

scaled, that is with $u_* \cos\theta$, the vertical velocity profiles for $\theta = 0°$ and $\theta = 60°$ look similar. For the flow at an angle, the enhancement of the horizontal velocity over the crest of the wave is somewhat smaller. Also, the real part of the vertical velocity perturbation is reduced, which is equivalent to a lower growth rate.

The differences between the dashed and solid lines are due to the angular factor $(1 + \cos^2\theta)/2$ in the left-hand side of (3.57) and changes in the IR depth kl. Another potential cause is the additional forcing term, related to the transverse motions $\widehat{v}$, in the right-hand side of (3.57). The solution with this term omitted is represented by the dotted line in figure 3.10. The dotted lines are hardly visible since they lie on top of the dashed lines, meaning that the $\widehat{v}$ term can be neglected. This appears to be the case for arbitrary wave-age parameter and angle. Hence, the wave-induced motions in transverse direction do not have to be calculated if one is only interested in the flow in wave direction, thus, for example, in the growth rate. The vorticity equation (3.58) may then be solved after the flow in wave direction has been computed.

Considering the small impact of θ on the vertical velocity profiles, provided these are properly scaled, we expect that the influence on the growth rate is also limited. For the case of non-zero θ the definition of β, equation (2.23), is generalized to

$$\frac{\dot{E}}{\omega E} = \frac{\rho_a}{\rho_w} \left(\frac{u_* \cos\theta}{c} \right)^2 \beta, \tag{3.60}$$

The angular dependence of β is assessed in figure 3.11a, which shows the growth-rate parameter as a function of the inverse wave-age parameter. The simulations with $\theta = 0°$ and $180°$ are connected by the solid line. These solid lines correspond to those in figure 3.6, where now the case of waves moving against the wind has been added. Such waves have a negative growth rate, meaning that they are damped by the wind, just as fast waves.

Predictions of β for non-zero angles are represented by the symbols in figure 3.11. In good approximation, the symbols collapse on the solid lines, both for the semi-analytical and the numerical model. This means that the component of the wind in wave direction to a large extent determines the growth rate, and contributions from the transverse wind component are small. There is some influence of the angle: in general, β appears to decrease somewhat with increasing θ. Only when θ becomes close to $90°$ (the plus symbols in figure 3.11), the deviations start to be significant. This is due to the scaling in (3.60), which becomes singular for $\theta = 90°$. Figure 3.11 suggests that the growth-rate parameter for arbitrary angle (except when θ is close to $90°$) can be described by

$$\beta\left(\frac{u_*}{c}, \theta \right) = \beta\left(\frac{u_* \cos\theta}{c}, 0° \right), \tag{3.61}$$
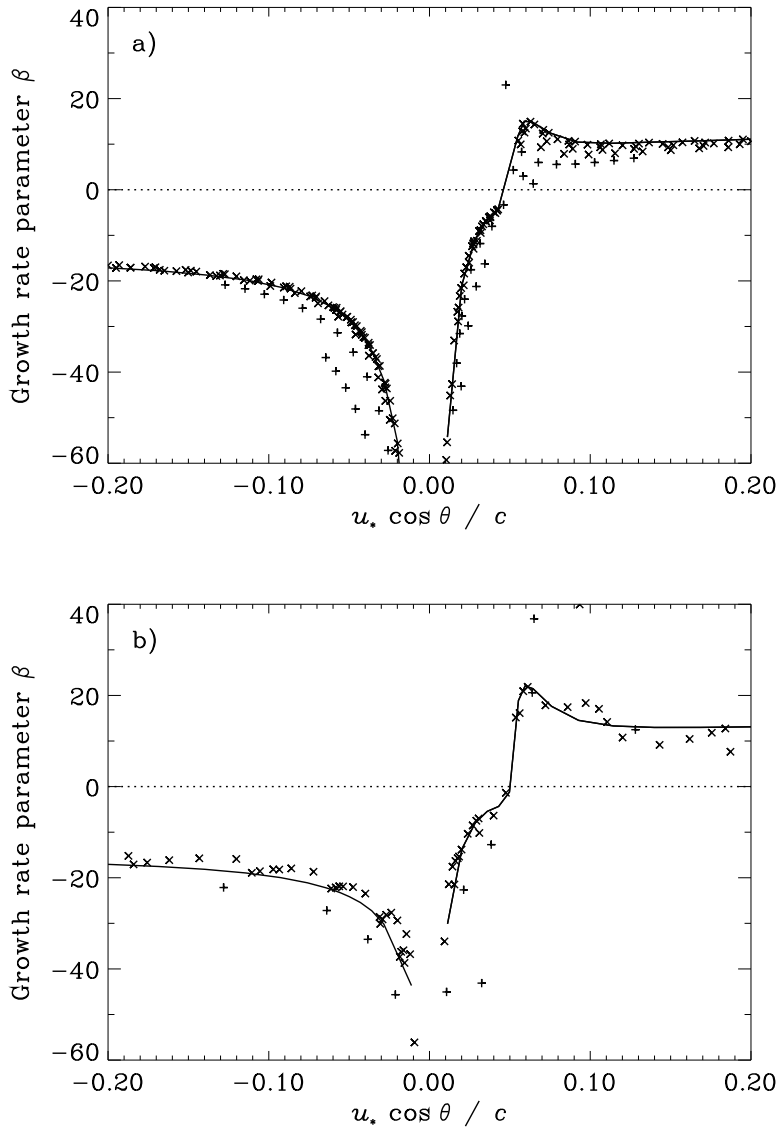
Figure 3.11: Growth-rate parameter as a function of $u_* \cos\theta/c$: (a) semi-analytical model and (b) numerical model with second-order turbulence scheme. The solid lines connect runs with $\theta = 0°$ and $180°$. The crosses represent runs with $0° < \theta < 70°$ and $110° < \theta < 180°$. The pluses are runs with $70° \leq \theta \leq 110°$. Simulations have been performed for various u_*/c with steps of $10°$ for θ. A fixed dimensionless roughness length, $kz_0 = 10^{-4}$, is employed.

which effectively removes its angular dependence. The right-hand side of (3.61) can be evaluated using the solid curves in figure 3.11.
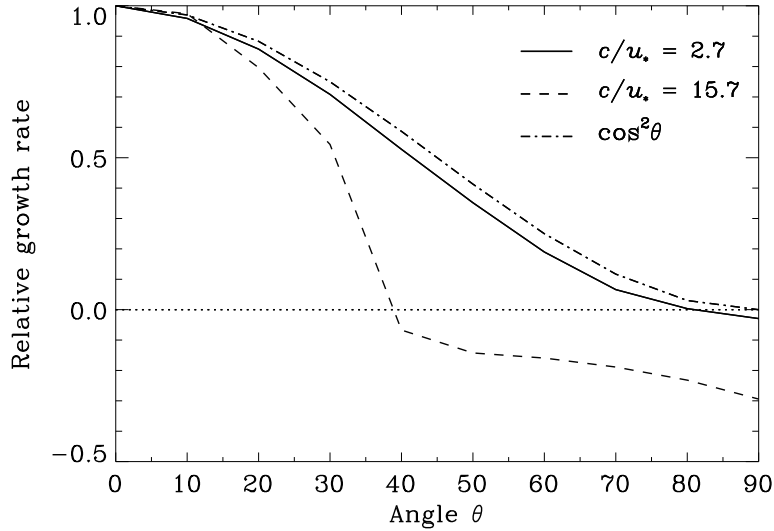
Figure 3.12: Angular dependence of the growth rate for two different ratios of wind and wave speed, according to the semi-analytical model for $kz_0 = 10^{-4}$. The growth rate is divided by its value at $\theta = 0°$.

Figure 3.12 shows the growth rate as a function of θ relative to the growth rate at $\theta = 0°$ for two different ratios of wind and wave speed. For the slow-wave case, the angular distribution is close to $\cos^2 \theta$. This resembles the finding that the growth-rate parameter is more or less independent of wave age. In contrast, the faster-wave case shows a narrower distribution since these waves enter the fast-wave regime already at smaller angles. Notice that for $\theta = 90°$ the waves are damped because, effectively, the wind is blowing against the waves then.

3.7.2 Reynolds number

It is interesting to extend the semi-analytical model to the case of low Reynolds numbers so as to allow comparison with the results of chapter 2. We have done this by making three modifications:

- the mean velocity profile $U(z)$ following from equations (2.11) and (2.12) is used instead of (3.6);

- the inner region depth kl is defined as in equation (2.13);

- the viscous contribution is taken into account in the expression for the wave-induced shear stress. This implies that (3.42) becomes

$$\widehat{\tau}_{13} = (2\kappa z u_* f_D(z) + \nu)\, \frac{\partial \widehat{u}}{\partial z} \mathrm{e}^{-z/l}, \qquad (3.62)$$

where we have assumed $\theta = 0°$ for convenience.
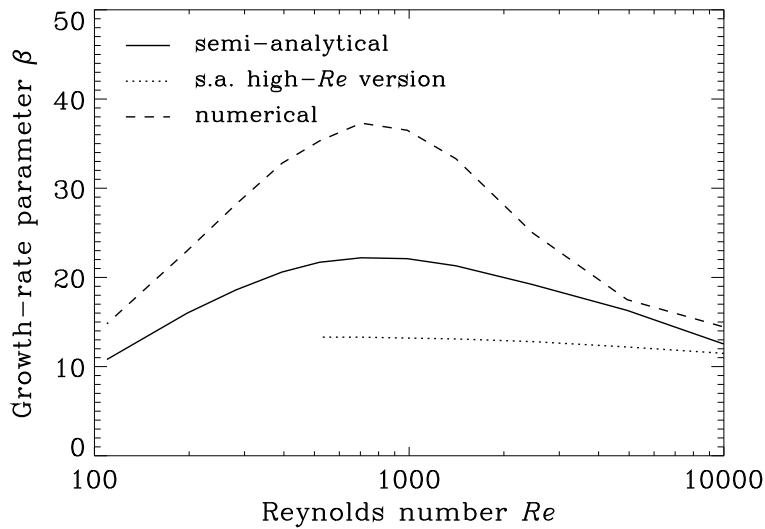
Figure 3.13: Growth-rate parameter as a function of the Reynolds number for waves moving slowly compared to the wind speed. For the simulations a fixed value of the friction velocity, $u_* = 0.25 \text{ m s}^{-1}$, was used.

Figure 3.13 shows the growth-rate parameter for slowly moving waves calculated by the low-*Re* version of the semi-analytical model. For Reynolds numbers of around 10^4, this version predicts the same value for β as the high-*Re* version. Also, there is little difference with the numerical model, as was already presented in figure 3.6. Towards lower *Re*, the growth-rate parameter increases. The predicted curve is qualitatively the same as following from the numerical model: β peaks around $Re = 800$. Nevertheless, the peak is much less pronounced. It is unclear why these differences are present. Probably, the present incorporation of viscous effects is somewhat too simple and needs revision.

3.8 Conclusions

A simplified model for the turbulent air flow over a surface wave propagating with arbitrary phase velocity and in arbitrary direction as compared to the wind has been presented. The main simplification is achieved by the division of the wave boundary layer into inner and outer regions, as suggested by Belcher and Hunt (1993). In the OR the wave-induced motion experiences inviscid undulation, whereas in the IR the motion is strongly affected by the turbulent shear stress.

The IR depth is relatively small ($kl \sim 0.1$) for all waves, except for those propagating with a phase velocity close to the wind speed, that is, the inverse wave-age parameter is $1 < U_k/c < 1.2$. In this narrow range the height of the IR is $kl \sim 1$. An important conclusion resulting from the analysis of the IR depth is that the critical height, the height where the wind speed equals the phase velocity of the wave, is almost always located inside the IR. This means that the singular behavior of the critical-layer dynamics is strongly suppressed by the turbulent stress for all waves, with exception of those with inverse wave age $U_k/c < 1.2$. However, when the ratio of wind to wave speed drops below this value, the critical height rapidly grows and, hence, its effect on the air-flow dynamics strongly diminishes.

The fact that the singular behavior of the critical-layer dynamics does not influence the inviscid OR, allows a simple description of the velocity in the OR, based on the approximate solution of the Rayleigh equation suggested by Miles (1957). The description of the IR is based on the zero-order solution (in terms of a kl-power expansion) solution of the vorticity conservation equation. A kl-order correction of the IR solution has an important physical meaning only for the real part of the vertical velocity. This component of the vertical motion, which is generated inside the IR due to the action of the shear stress, penetrates into the OR and generates the slope-correlated component of the air pressure. The pressure then penetrates into the thin IR and forms the energy and momentum flux between wind and waves. This is the non-separated sheltering mechanism of wave growth described by Belcher and Hunt (1993).

The results obtained by the semi-analytical model show an encouraging agreement with the numerical model presented in the previous chapter. The good agreement concerns both wave-induced velocity and shear-stress perturbations, and the growth-rate parameter. The predicted dynamics of the wave-induced air flow depends critically on the turbulence closure (e.g., Mastenbroek et al. 1996; Belcher and Hunt 1998). For example, an unmodified mixing-length closure would fail to correctly, and sufficiently, damp the wave-induced Reynolds stresses in the OR and would typically strongly overpredict the wave growth. We use a phenomenological approach and directly suppress the turbulent stress with height towards the OR.

Nevertheless, such an, admittedly rather crude, approach gives results that are in good agreement with those found by using a second-order Reynolds-stress closure scheme. The results of the semi-analytical model are generally consistent with laboratory observations performed by Hsu and Hsu (1983). These experimental data confirm the existence of outer and inner regions above waves.

In the case of a non-zero angle between wind and wave directions, two coupled equations have to be solved for the vorticity components Ω_1 and Ω_2. However, it is shown that the former equation has a negligible influence on the latter. Hence, if one is interested in the flow in the wave direction, it suffices to solve only the equation for Ω_2. The model results indicate that the growth-rate parameter depends mainly on the ratio of the component of the wind speed in the propagation direction of the wave to the phase speed of the wave. The numerical model shows the same feature, as was already concluded by Mastenbroek (1996). This implies that the growth rate γ of slowly moving waves is proportional to $\cos^2\theta$, which contrasts with the $\cos\theta$-dependence proposed in many papers (e.g., Plant 1982; Komen et al. 1994). For a wind–wave angle of 60^0, the formulations differ by a factor 2, which is clearly significant. Furthermore, faster waves, often the energy containing waves in the spectrum, have a narrower angular distribution of γ, which should be considered in wave prediction models.

The semi-analytical model has been modified to take into account viscous effects. Although the present model predicts a much weaker increase of the growth-rate parameter at low Reynolds numbers, qualitatively a similar dependence of β on the Reynolds number is found as calculated with the low-*Re* numerical model presented in the previous chapter.

Chapter 4

Sea spray in the marine surface layer

4.1 Introduction

In the previous chapters we have reported detailed investigations of the air-flow dynamics above water waves. In particular, the role of waves in air–sea exchange of momentum has received attention. Waves grow due to the wind, which means that they exert drag on the air flow, the so-called form drag. This downward transport of momentum is governed by organized wave-induced motions. The air flow is thus strongly coupled with the waves. In short: higher winds lead to higher waves, which cause a higher form drag. As a consequence, the exchange coefficient for momentum, or drag coefficient, is found to increase with wind speed, as is shown in figure 1.1.

For heat, moisture and other scalars, this transport mechanism is not present. The reason for this is that, at the surface, such scalars are not correlated with the wave motions. Hence, the wave-induced heat flux $-\langle \tilde{\theta}\tilde{w} \rangle$ will be small. Heat is transported mainly by molecular (near the surface) and turbulent diffusion. In this sense, waves have only an indirect effect on the exchange of heat and moisture, namely by modifying the turbulent diffusion. Thus, the exchange coefficients for heat and moisture are expected to have only little wind speed dependence, which is indeed confirmed by experimental observations (see figure 1.3).

Does this mean that the problem of heat and moisture exchange over the sea is settled? Not really: from wind speeds of 4 m s^{-1} waves start to break. With the breaking, sea spray droplets are ejected into the air (see chapter 1). The freshly produced droplets adjust to the ambient atmospheric humidity by evaporation (or condensation), which implies a sink (source) of energy, and a source (sink) of water

vapour for the atmosphere. In this way, sea spray may provide an efficient way to influence the balance of heat and moisture over the sea.

For numerical weather prediction it is important to know the magnitude and spatial variation of this influence, which is what we aim to assess in the present thesis. To this end, the impact of spray evaporation on the air–sea heat exchange must be estimated. This is a complicated task because spray brings along with it many complex physical processes, which are, at the least, not straightforward to model. At the same time, experimental investigations are hampered by the violent conditions present over the sea, particularly at the high wind speeds at which significant spray concentrations occur.

In section 4.2, a review of current experimental knowledge concerning sea spray is given. For a proper interpretation of this experimental evidence, a thorough understanding of sea spray physics is needed. In section 4.3, several aspects of this will be discussed in the context of spray models already presented in the literature. It is argued that some important aspects are, at the least, not fully understood. An example is the influence of the wave-induced air flow on spray transport, which is studied in section 4.4 using the spray model by Mestayer et al. (1996).

4.2 Experimental evidence

The key elements in understanding sea spray and its effects on the heat budget are the rate at which spray droplets are produced from the sea, the vertical fluxes of spray droplets, and the spray-mediated evaporation. Unfortunately, none of these quantities is directly measurable. Therefore, we must restrict ourselves to things that are measurable. These include droplet concentrations and turbulent heat fluxes. Those measurements may then be used to infer information on the above items.

Concerning concentrations of spray it must be noted that not only the total volume of droplets but also their radial distribution is highly relevant since their evaporation depends on radius. According to Andreas (1992), droplets with initial radii between 10 and 300 μm carry most of the volume flux. For smaller droplets, in particular the submicron aerosols, an extensive set of experimental observations exists. In contrast, it is difficult to measure concentrations of the larger droplets because there are relatively few of them.

To estimate the impact of spray on the heat balance, probably the most important input parameter is the rate of spray production. Many attempts have been made to derive this source function from droplet concentration spectra measured at some distance from the surface (e.g., Fairall et al. 1990; Smith et al. 1993; Wu 1993). The problem with such derivations is that models are needed to determine which part of the droplets initially formed reach the measurement height, and to what extent these

droplets have evaporated on their way. This introduces a large uncertainty in the resulting source function.

A major link between droplet measurements at some height and the production of droplets at the surface is the vertical transport of the droplets by turbulence. This upward vertical transport is balanced by gravitational settling:

$$-\overline{\rho_n' w'} = -V_f \rho_n, \tag{4.1}$$

where ρ_n is the mass concentration of droplets in a particular size bin n, and V_f is the terminal fall velocity of droplets in this bin (see Pruppacher and Klett 1978). Toba (1965) considered this balance with a simple turbulence closure

$$-\overline{\rho_n' w'} = K \frac{\partial \rho_n}{\partial z}, \tag{4.2}$$

with $K = \kappa u_* z$. Equating the right-hand sides of (4.1) and (4.2), and integrating from a reference height z_r to z, a power-law vertical profile of droplet concentration is obtained

$$\rho_n(z) = \rho_{nr} \left(\frac{z}{z_r} \right)^{-V_f(r)/\kappa u_*}. \tag{4.3}$$

Relation (4.3) is of course simplified in that complicating effects due to, for example, evaporation and wave-induced air flow are neglected, but it gives the basic properties of vertical transport. Furthermore, it illustrates that for the droplets of major interest, i.e. those with radii of more than 10 μm, a clear vertical gradient is present since these droplets have a non-negligible fall velocity V_f.

At the same time, as stated above, it is hard to make accurate observations of these larger droplets above the sea. More accurate measurements can be made under controlled conditions in the laboratory but it is not straightforward to extrapolate these results to field conditions.

In the following, we will shortly review the available experimental evidence concerning spray concentrations and heat fluxes, and discuss the problems that are encountered when one wants to derive source functions and evaporation rates from these measurements.

4.2.1 Production rates

As was discussed above, source functions have often been derived from spray measurements at some distance from the surface. Mestayer et al. (1996) noted that this approach, which they termed the above–down approach, is indirect since it deduces the surface source function from its consequences, namely the droplet concentrations in the air.

In principle, direct, or below–up, methods to estimate source functions are also possible. These should concentrate on measurements of bubble spectra in the ocean, and combining these with laboratory observations of the amount of spray production per bursting bubble and estimates of the whitecap coverage on the ocean as a function of, primarily, wind speed. Experimental results on most of the steps in this method have been presented (Monahan et al. 1982; 1986; Blanchard 1983; Resch and Afeti 1991; Wu 1992; Spiel 1994). However, these studies concern bubble-mediated (jet and film) droplets only. Because of experimental difficulties, extension of the method to spume and splash droplets is not easy. Moreover, validation with spray concentrations measured aloft has not been done.

All these problems and uncertainties hamper accurate predictions of spray production rates. Andreas (1998) collected a large number of source functions presented in the literature. He showed that the estimated volume fluxes of spray vary by as much as six orders of magnitude. There seems to be somewhat more consensus concerning the radial distribution: most functions predict a peak in the volume flux for radii between 10 and 200 μm. Obviously, the source functions also have in common a strong wind speed dependence. The production rate of jet droplets is generally reported to be proportional to the whitecap coverage, which in turn was estimated to be proportional to $U_{10}^{3.41}$ by Monahan and O'Muircheartaigh (1980), or to u_*^3 by Wu (1988). The spume-dominated source functions show much more variation in wind speed dependence (Andreas 1998), again because the experimental difficulties are largest for the spume droplets.

We can conclude that, whereas there is a reasonable understanding of the individual processes that govern the production of sea spray, the total spray generation function is poorly known.

4.2.2   Vertical distributions

Despite the difficulties involved with measuring vertical profiles of concentrations of large spray droplets, several authors have reported experimental work in this direction. It is generally reported that spray droplet concentrations are highest near the surface and decrease towards higher elevations (see the compilation of existing experimental data by Blanchard and Woodcock 1980). Measurements close above the sea surface were performed by Chaen (1973) and Preobrazhenskii (1973). They fitted the above power law and an exponential decay function, respectively, to their profiles.

Later experimental work (De Leeuw 1986; 1987) indicates that such fits of the vertical profiles cannot always be made. On the North Atlantic, De Leeuw (1986) found maxima in droplet concentration at 1–2 m above the surface. He argued that this was due to recirculation of droplets in the air flow above the wave troughs.

Alternatively, the elevated maxima might be caused by spume droplets, which are produced at the height of the wave crests (Monahan et al. 1986). At elevations higher than 2 m, De Leeuw (1986) observed a decrease of droplet concentrations with height. In other experiments, over the North Sea, the elevated maxima were less pronounced and not always observed (De Leeuw 1987). Also, the spray concentrations were often found to be constant or even slightly increasing with height.

Representative laboratory experiments concerning spray were performed during the HEXIST (Mestayer and Lefauconnier 1988) and CLUSE (Mestayer et al. 1990) campaigns, in the wind–water interaction tunnel at IRPHE in Luminy, France. Here, the droplets were not generated by breaking waves, as on the ocean, but by immersed aeration devices producing bubble plumes. The measured vertical profiles of droplet concentration show an exponential decay with height (Edson et al. 1996). However, the boundary layer thickness in the tunnel was only about 60 cm, so details such as the presence of elevated concentration maxima could not be verified.

4.2.3 Heat fluxes

The turbulent fluxes of latent and sensible heat over the ocean have been measured in many field campaigns (e.g., Large and Pond 1982; DeCosmo et al. 1996; Fairall et al. 1996; Eymard et al. 1999). As was noted in the introduction of this chapter, spray can influence the heat fluxes by evaporation. This should be visible in the heat exchange coefficients, for example through the appearance of a wind speed dependence. Nevertheless, while the number of spray droplets increases rapidly with wind speed, hardly any wind speed dependence of the neutral heat exchange coefficients was observed during the above field campaigns (see figure 1.3).

It must be noted that this does not necessarily mean that there is no significant evaporation of spray since we do not know how large the heat fluxes would have been in the absence of spray. Andreas and DeCosmo (1999) argued that the HEXOS data (DeCosmo et al. 1996) did contain a spray signal. They used the bulk flux algorithm by Fairall et al. (1996) as a reference and attributed differences with the fluxes measured during HEXOS to spray evaporation. Although their conclusions seem to depend heavily on the choice of this particular bulk flux algorithm, their results at least indicate that there can be evaporation of spray while the heat exchange coefficients do not show any wind-speed dependence.

It is also possible that the height of the measurements was, in general, too low to fully observe changes in the exchange coefficients. That is, the measurements were within the layer where the droplets were evaporating. We will return to this point, which was put forward by Andreas et al. (1995), in chapter 5.

Apart from the above two considerations, it must be concluded that spray evaporation is not significant at wind speeds below 18 m s^{-1}, at which the vast majority of

the measurements was performed. Andreas et al. (1995) distinguished two reasons for this. Firstly, spray production rates just might be too low. The uncertainty in estimates of source functions mentioned before leaves this possibility open. Secondly, negative feedbacks (see chapter 1) might considerably limit the evaporation of spray droplets.

Perhaps the only sign of effects of spray evaporation on the heat budget in the marine surface layer is given by measurements of the air–sea temperature difference during the passage of two tropical cyclones by Korolev et al. (1990). Their data show a cooling of the lower atmosphere by up to 5 °C at wind speeds of around 25 m s^{-1}. Fairall et al. (1994) suggested that at least part of this effect should be due to spray evaporation, for which the atmosphere is supplying the necessary heat.

In summary, the experimental evidence of sea spray is limited, both due to the violent conditions above the sea, in particular at high wind speeds, and due to the difficulty of measuring the low numbers of large spray droplets. To make a proper interpretation of these limited experimental data, a thorough understanding of sea spray physics and numerical models representing and coupling the various aspects of this physics are needed.

4.3 Sea spray physics and modelling

A complete discussion of all relevant physical processes related to sea spray would be beyond the scope of this thesis. Therefore, we limit ourselves to those aspects that are essential for assessing the role of spray in air–sea heat exchange. Additional attention will be given to wave-related issues, which are particularly important in the light of the present thesis. In the second part of this section, an overview of existing spray models is given. Although these models have a large number of common assumptions, they also differ in some respects, dependent on the specific goals the authors have set themselves. Three individual models are compared in more detail, on the basis of the aspects considered earlier. At the end of the section, general model results are reviewed, and it is shortly outlined how the modelling work relates to the available experimental data.

4.3.1 Aspects of spray physics

Below are some specific aspects of spray physics. For each aspect the implications for modelling are outlined.

- *radius and temperature evolution*
  Once airborne, spray droplets adjust to the ambient atmospheric conditions. This adjustment concerns both their temperature and their radius. Based on the

work of Pruppacher and Klett (1978), Andreas (1989; 1990) presented equations for the temperature and radius evolution of sea-water droplets released in specific atmospheric conditions. From this work it may be concluded (Andreas 1992) that spray droplets generally fully exchange sensible heat with the air (at least the droplets in the size range of a few to a few hundreds of micrometers, which have a potentially important effect on the heat balance). For purposes of modelling, it may thus be assumed that spray droplets instantaneously reach temperature equilibrium with the air, which has the advantage that the droplet temperature is not a variable in the model. On the contrary, spray droplets only partly exchange latent heat with the air, except perhaps those with radii less than around 10 μm.

- *salinity*
  The fact that sea spray droplets contain salt causes some complications for modelling. The salinity of a spray droplet increases when it evaporates. Hence, the saturation vapour pressure over its surface increases, which counteracts further evaporation. A spray droplet cannot completely evaporate but will reach an equilibrium radius depending on its initial radius and salinity, and on the atmospheric relative humidity. To take this into account in Eulerian models implies that, apart from the radius, also the salt content of a droplet must be introduced as a variable, which leads to a considerable increase in calculation times compared to the case of fresh water. In Lagrangian models, salinity hardly gives rise to complications.

- *atmospheric feedback*
  The presence of spray causes changes in the temperature, humidity, and turbulence structure of the atmosphere. These changes, in turn, influence the fate of the spray droplets. In general, such interactions cannot be neglected (see, e.g., Kepert et al. 1999; Van Eijk et al. 2001). For models this implies that the evaporating spray and the atmosphere must be allowed to respond to each other, which is, in particular for Lagrangian models, a complicated task.

- *wave-induced flow*
  As was demonstrated in the previous chapters, waves modulate both the mean air flow and the turbulence therein compared to flow over a flat or undulating, rigid, stationary surface. Thus, the transport of spray droplets above waves will be different from that over a flat surface. Some studies of this aspect have been made (Andreas et al. 1995; Mestayer et al. 1996), which have indicated a considerable impact. However, final conclusions cannot be made, because these studies have used unrealistically simplified descriptions of the air flow over waves.

- *inertial effects*
  A couple of complicating aspects are related to the non-negligible inertia of large spray droplets. Such droplets do not instantaneously adjust their velocity to the air flow. For example, after ejection, jet droplets initially move upwards. It will take some time for them to attain their terminal fall velocity. Another aspect is that the larger droplets are not able to respond to the smaller turbulent eddies in the atmosphere. This reduces their diffusion compared to a very small droplet. The thermodynamic consequence is that, when not reacting to the smaller eddies, the droplets are ventilated, which implies an increased exchange of sensible and latent heat with the surroundings compared to still air conditions. It seems that the inertial effects mentioned here, which can be quite important for the larger droplets, can be adequately parameterized both in Eulerian and Lagrangian models (see, e.g., Rouault et al. 1991; Edson et al. 1996).

- *density effects*
  Spray droplets contribute to the total density of the atmosphere. When spray loads are high, this might lead to a substantial deviation of the density from ρ_a. Furthermore, profiles of spray droplets are inherently stably stratified. This causes a destruction of turbulent kinetic energy, and, thus, reduces turbulent diffusion (see also Bintanja 2000). This aspect has not been given much attention in the literature but it is expected that, except perhaps for hurricane wind speeds, spray concentrations are too low for density effects to become significant (see Fairall et al. 1994).

- *initial conditions of droplets*
  To model the fate of droplets in the air, it is important to know the location relative to the wave where they are ejected and the initial velocity (direction and speed) with which they are ejected. For film and jet droplets, these initial conditions are fairly well known from laboratory studies (Resch and Afeti 1991; Spiel 1994). For spume droplets, the initial position is at the wave crest. However, the initial dynamics are unknown. Until experimental efforts in this direction will have been performed, the representation of their initial conditions in models will be impossible.

4.3.2   Spray models

The literature contains a large number of publications on sea spray models, of which we mention here Ling and Kao (1976), Stramska (1987), Rouault et al. (1991), Edson and Fairall (1994), Edson et al. (1996), Mestayer et al. (1996), Fitzgerald et al.

(1998), Kepert et al. (1999), and Van Eijk et al. (2001). These models explicitly take into account spray droplets and their interactions with the atmosphere, and allow for calculations of vertical distributions of temperature, humidity, and droplet spectra. Another approach consists of estimating the effects on the heat balance of a given amount and spectral distribution of spray droplets. Such simpler models were, among others, presented by Andreas (1992), Fairall et al. (1994), and Makin (1998). We will return to those in chapter 5.

Most of the former models are Eulerian surface layer models. These involve the solution of conservation equations for momentum, (potential) temperature, humidity, and droplet concentration. The droplets are normally divided into size bins, where transition between bins is possible when evaporation or condensation occurs. Other models treat the droplets in a Lagrangian way (Edson and Fairall 1994; Edson et al. 1996), calculating a large number of individual droplet trajectories, which are then averaged to obtain vertical concentration and evaporative flux profiles. The Eulerian models by Rouault et al. (1991), Mestayer et al. (1996) and Van Eijk et al. (2001) used a Lagrangian pre-processor to take into account effects of the wave-induced air flow and droplet inertia.

Some assumptions are common in all spray models (see, e.g., Van Eijk et al. 2001). These include properties of the air flow, for example: the air is incompressible, the Boussinesq approximation can be applied, the flow is horizontally homogeneous (in case of a 1D model), and the Coriolis force can be neglected. Further, many assumptions on the spray droplets are made, in order not to make the problem (unnecessarily) complicated. Such assumptions include: the droplets are spherical and non-cohesive, they do not break up or coalesce, and there are no chemical reactions. Finally, it is normally tacitly assumed that the air–droplet mixture can be considered as a continuum with Newtonian characteristics (see, e.g., Bintanja 2000). First, this means that the droplets must be smaller than the smallest turbulent length scale, the Kolmogorov scale, τ_k. In the atmosphere, $\tau_k \approx 1$ mm, so this condition is generally met. Second, droplet interactions must be negligible. The change in apparent viscosity due to such interactions is of the order of 1 % for a droplet volume concentration of 0.003 (Lumley 1978). Based on the source function of Andreas (1998), the volume concentration of spray droplets is estimated to be of the order of 10^{-6} at high wind speeds. Thus, the flow can indeed be considered as a continuum.

Apart from these basic assumptions, existing spray models differ in many respects, depending on their specific aims. In general, the dynamics are represented in a relatively simple way. The spray droplets make the problem complicated, and the full physics is either unknown or it is not feasible to represent it. Therefore, often many simplifications are made, while certain aspects, dependent on the aim of the study, are modelled in detail. In the following, three selected models are compared

to demonstrate this. These three models have been chosen because they are recent, and reasonably cover the variety of spray models presented in the literature,

4.3.3   Comparison of selected models

Property	EAMS	KFB	VTM
Eulerian (Eul) / Lagrangian (Lag)	Eul–Lag	Eul	Eul (Lag)
1-dimensional (1D) / 2-dimensional (2D)	1D/2D	1D	1D (2D)
Surface layer (SL) / boundary layer (BL)	SL	BL	SL
Turbulence closure	e–ε	G88	K-theory
Source function	A92	–	A92
Injection height	h_{ej}, A_s	A_s	surface
Radius range (μm)	2–200	1–500	10–250
Fresh / salt water	fresh	salt	salt
Instantaneous radius equilibrium	no	no	no
Instantaneous temperature equilibrium	no	yes	yes
Atmospheric feedback	yes	yes	yes
Effect of waves on turbulence	no	no	yes
Effect of waves on mean flow	no	no	yes
Effect of inertia on droplet vertical velocity	yes	no	yes
Effect of inertia on droplet turbulent diffusion	yes	yes	yes
Ventilation of droplets by air flow	yes	yes	no
Effect of droplet density on total density	no	no	yes
Effect of droplets on TKE	yes	yes	no
Initial conditions of spume droplets	no	no	no

Table 4.1: Comparison of three spray models: EAMS (Edson et al. 1996), KFB (Kepert et al. 1999), and VTM (Van Eijk et al. 2001). Further explanation: G88 is the turbulence model described in Galperin et al. (1988); A92 is the source function presented in Andreas (1992); h_{ej} is the ejection height of jet droplets; $A_s = H_s/2$ is the significant wave amplitude; 'yes' means that the specific feature is taken into account; 'no' that it is not.

Table 4.1 gives a more detailed overview of the properties of three selected models. The model by Edson et al. (1996) is a Eulerian representation of the flow with a Lagrangian description of the droplets. It is specifically aimed at a comparison with the CLUSE laboratory experiment (see page 71). Hence, fresh water was considered, and the model was developed in two dimensions, although 1D results were presented as well. The Lagrangian approach allowed a relatively easy explicit description of both the temperature and radius evolution of the spray droplets, and accurate mod-

elling of inertial effects. The surface was taken to be flat, and the droplets were released at a height h_{ej}, the ejection height of jet droplets as observed by Blanchard and Woodcock (1957), above the surface. In additional simulations, the droplets were released at the height A_s instead of h_{ej}, which should reflect the ejection level of spume droplets relative to the mean water surface. Results with a version of the model that explicitly took into account the air flow over the wavy surface, were presented in Andreas et al. (1995). Atmospheric feedback was accomplished by iteratively running the Eulerian and Lagrangian part of the model and, in every iteration, feeding the sensible and latent heat consumed or released by the spray droplets back into the Eulerian part.

Kepert et al. (1999) developed a Eulerian column model of the atmospheric boundary layer containing evaporating saline droplets. Modelling the whole atmospheric boundary layer facilitated the choice of boundary conditions and allowed them to investigate the mixing of, in particular, the smaller particles beyond the surface layer. They simplified modelling of the droplets' thermal evolution by assuming that the droplets instantaneously reach thermal equilibrium when they enter the air. All droplets were injected at the height of the significant wave amplitude. The issue of choosing a source function was avoided by presenting the spray-mediated latent heat flux relative to the potential latent heat flux, which is the flux that would be realized if all of the droplets produced from the ocean were evaporated in the atmosphere.

The model by Van Eijk et al. (2001), named SeaCluse, is a 1D Eulerian representation of the marine surface layer. In SeaCluse, specific attention is paid to wave effects. The model includes a 2D Lagrangian pre-processor, in which droplet trajectories in the mean air flow over the waves are calculated. After averaging, this yields the vertical distribution of droplets in the case of no evaporation and no turbulence. In the SeaCluse main model, these distributions are used as background profiles. Furthermore, in the main model, the wavy surface is represented by injecting droplets at the height of the instantaneous water surface.

4.3.4   Model results versus experiments

Production rates

Spray models use the source function as an input. In principle, they then give the possibility to judge whether a certain source function is realistic, within the limits of the model assumptions, by comparing calculations of the droplet concentration at a certain height with observations. This was done by Van Eijk et al. (2001). Using the source function of Andreas (1992) (henceforth A92), they obtained reasonable agreement between modelled and measured droplet concentrations at 10 m height

for radii of 15–30 μm and wind speeds up to 20 m s^{-1}. However, because of the considerable measurement errors, such comparisons cannot give more than a rough indication of the validity of a source function. In particular, the experimental data of larger droplets have poor statistics since there are only few of them.

Vertical distributions

The modelling studies found in the literature generally report a rapid decrease in concentration with height. Edson et al. (1996) found an approximately exponential decay, which was in good agreement with the CLUSE laboratory experiments. Van Eijk et al. (2001), who took into account the effect of waves on the air flow, obtained more or less constant droplet concentrations between the wave troughs and crests, while, at higher altitudes, their profiles appear to have the power-law shape of relation (4.3).

Heat fluxes

The predicted impact of spray on the heat fluxes depends heavily on the source function that is chosen. Using the A92 function, and for a wind speed of 18 m s^{-1}, Edson et al. (1996) reported little impact when the droplets were released at the height h_{ej}. On the contrary, when the droplets were released at the height A_s, representative of spume droplets, they stayed airborne for a much longer time, and the heat flux was significantly affected. This illustrates the sensitivity of the model to the initial conditions, which is a problem considering that the ejection height scale for spume droplets is only a rough estimate.

Kepert et al. (1999) showed that the droplet evaporation layer (DEL) can become as high as 70 m for droplets with $r \approx 60$ μm, at a wind speed of 25 m s^{-1}. Similarly, Van Eijk et al. (2001) obtained a DEL depth of 20–30 m for a wind speed of 20 m s^{-1}. As was hypothesized in section 4.2.3, this indeed suggests that in many experiments, with measurement heights of the order of 10 m, the contribution of evaporating spray to the heat fluxes may not have been fully measured.

Other model results

Apart from the limited comparisons with field observations, numerical models have frequently been used to make predictions beyond what is experimentally verifyable. Typical results concern evaporation efficiencies, i.e. to what extent do droplets of a particular size contribute to the heat fluxes, and interactions of the evaporating droplets with the surface-layer structure.

From their calculations at a wind speed of 25 m s^{-1}, Kepert et al. (1999) found that droplets with radii of up to around 50 μm generally reach their equilibrium radius. These findings are supported by the work of Van Eijk et al. (2001), who concluded that, given the A92 source function, the droplets in the 30–50 μm-range contribute most to the latent heat flux.

Spray evaporation leads to cooling and moistening of the surface layer, which causes the interfacial latent heat flux to decrease compared to the no-droplets case. Above the DEL the flux increases but not as much as would be possible in a fixed atmosphere. For the sensible heat flux the effects are opposite. This general picture is reproduced by all numerical models. However, the extent to which changes in the atmospheric structure give negative feedback to both interfacial and spray evaporation greatly varies between different studies. It has become clear that the importance of such feedback effects heavily depends on the production rate of droplets (e.g., Kepert et al. 1999).

In summary, a variety of models explicitly taking into account spray droplets and their interactions with the atmosphere have been presented in the literature. These models include detailed descriptions of relevant spray physics. Yet, verification of the model results is hardly possible because experimental data are scarce and often have large measurement errors. In this thesis, we are interested in effects of spray on the heat balance in the surface layer over the sea. The magnitude of such effects mainly depends on the spray generation function, which is poorly known. Hence, model predictions of these effects are highly dependent on the source function that is chosen. For use in numerical weather prediction models, simplified approaches are necessary, which give estimates of the contribution of spray to the air–sea fluxes within short calculation times. Such approaches should use results of more complicated numerical models as well as general empirical knowledge to simplify the problem. Necessarily, physical aspects that are of secondary importance will have to be neglected but this may be justified by considering that, anyway, the underlying source function provides the largest uncertainty. Of course, the most important features should be captured. In chapter 5, such a simplified model will be presented. The present chapter is ended with a short study in which the impact of the air flow on droplet distributions in the atmosphere is investigated. This will illustrate once more that the problem of sea spray in the marine boundary layer is sensitive to many processes, for which the physics is partly unknown.

4.4 Illustration: impact of wave-induced air flow on the dynamics of sea spray

After ejection into the air, spray droplets are transported through the atmosphere. The trajectories they follow depend on the combination of the instantaneous wind velocities they encounter and their fall velocity due to gravity. Over a flat surface the bulk effect of these competing processes can be represented by the balance equation (4.1), although modifications may be needed to take into account inertial effects (see page 74). Over a wavy surface, additional complications are present. Whereas the flow over a flat surface is characterized by a zero mean vertical velocity, the air over waves is moving up- and downwards dependent on the location relative to the wave. Such motions influence the transport of droplets and potentially lead to a modulation of spray concentrations compared to those over a flat surface.

Extending the work by Rouault et al. (1991), Mestayer et al. (1996) studied the dynamics of sea spray over waves using a numerical model named SeaCluse. They concluded that a mean circulating flow above the wave trough carries a large proportion of the droplets generated at the interface up to altitudes of a wave height above the surface. However, as they noted, these results were obtained with a fairly simplified description of the air flow. In the previous chapter, a semi-analytical model of the flow over waves was presented and shown to yield results in good agreement with measurements.

In the present study, the impact of the wave-induced flow on the transport of spray is investigated using both the original description by Mestayer et al. (1996), and the semi-analytical model for the air flow. In section 4.4.1, the SeaCluse model, which was already mentioned in table 4.1, is shortly outlined. Section 4.4.2 contains a comparison of model results for both underlying air-flow descriptions. Finally, a discussion and conclusions are given in section 4.4.3.

4.4.1 The model

The main purpose of SeaCluse is to describe the interactions between spray droplets and the scalar fields of water-vapour concentration and temperature in the marine atmospheric surface layer. The model computes along the vertical the horizontally averaged budgets of sensible heat and water vapour, and spray droplets concentrations. The spray droplets are divided into N size bins, and conservation equations are solved for each bin. Using Reynolds decomposition, these equations can be written as:

$$\frac{\partial \rho_n}{\partial t} = -\frac{\partial(\rho_n W_n)}{\partial z} - \frac{\partial\langle\tilde{\rho}_n\tilde{w}_n\rangle}{\partial z} - \frac{\partial\overline{\rho'_n w'_n}}{\partial z} + S_n \qquad n = 1\ldots N. \qquad (4.4)$$

Here ρ_n is the wavelength-averaged concentration of droplets in size bin n (units kg m^{-3}), and W_n is the mean vertical velocity; $\tilde{\rho}_n$ and $\tilde{w}_n$ are the wave-induced parts, and ρ'_n and w'_n the turbulent fluctuations of the droplet concentration and vertical velocity, respectively. S_n is a source-sink term representing generation and deposition at the water surface and transition between bins due to evaporation or condensation. Unlike Van Eijk et al. (2001), who employed Cartesian coordinates, we use the wave-following vertical coordinate z introduced in equation (2.16).

Apart from the source–sink term, the right-hand side of (4.4) contains a so-called macroscopic flux $\rho_n W_n$, a wave-induced flux $\langle \tilde{\rho}_n \tilde{w}_n \rangle$, and a turbulent flux $\overline{\rho'_n w'_n}$. For a flat surface, when the situation is stationary, when there is no evaporation or condensation, and when the droplets are assumed to have a mean vertical velocity equal to their terminal fall velocity, (4.4) reduces to (4.1). However, in the present study a wavy surface is considered, so the wave-induced flux cannot be neglected. Additionally, the hypothesis $W_n = V_f$ is not generally valid. Immediately after ejection, the droplets move upwards, and it takes some time before they attain their final fall velocity. This was first taken into account by Rouault et al. (1991), who modelled the macroscopic flux by a relaxation term of the form

$$\frac{\partial(\rho_n W_n)}{\partial z} = \frac{1}{C_1 \overline{T}_{\text{fly},n}} [\rho_n(z) - \rho_n^0(z)]. \tag{4.5}$$

Here $\overline{T}_{\text{fly},n}$ denotes the average flight time of the droplets in category n and $\rho_n^0(z)$ the concentration resulting from their transport in non-turbulent and non-evaporative conditions. The quantities $\overline{T}_{\text{fly},n}$ and $\rho_n^0(z)$ are obtained from a Lagrangian pre-processor, which is described below. The tuning constant C_1 was adjusted to 0.75 on the basis of comparison with laboratory observations. Mestayer et al. (1996) extended the model by Rouault et al. (1991) for the flow over waves and assumed that in this case the sum of the macroscopic and wave-induced flux can be represented with the same relaxation equation (4.5).

The general idea of the relaxation equation is as follows. The term $\rho_n / (C_1 \overline{T}_{\text{fly},n})$ is a good parameterization of the concentration sink due to the droplet removal by gravitational fall. On the other hand, $\rho_n^0 / (C_1 \overline{T}_{\text{fly},n})$ acts as a source term in (4.4) to restore the mean concentration profile due to both ejection and wave-induced flow. Finally, for stationary conditions and when the turbulence intensity is low, (4.4) leads to $\rho_n(z) \to \rho_n^0(z)$. A more detailed motivation of the relaxation equation can be found in Rouault et al. (1991).

The turbulent flux in (4.4) is modelled by means of eddy-viscosity theory

$$\overline{\rho'_n w'_n} = -(K_n + K'_n)\frac{\partial \rho_n}{\partial z}, \tag{4.6}$$

where K_n is the eddy-viscosity and K_n' is a 'counter-diffusivity' resulting because the droplets' inertia prevents them from following the turbulent motions exactly.

The pre-processor

In the pre-processor, spray droplets are ejected from the water surface into the air flow with a vertical velocity typical of jet droplets (Rouault et al. 1991; Blanchard 1989). During their flight they experience a drag force from the air and gravitational acceleration. Details on the equations used to describe the droplet motion can be found in Mestayer et al. (1996). To calculate the droplet motions in the air, the wind field must be prescribed. In the present study two wind fields are compared: the original SeaCluse wind field, and the wind field from the semi-analytical model presented in chapter 3.

The SeaCluse wind field is based on a postulated distribution of the horizontal velocity, from which the vertical velocity is calculated using the continuity equation. Mestayer et al. (1996) assumed the water surface to be described by a fifth-order Stokes wave. Here, a sinusoidal wave is considered, as given in equation (2.1), with $ak = 0.135$. The wave age is taken to be $U_{10}/c = 1.18$. These conditions correspond to a reasonably developed sea in case the wave is viewed as the component at the peak of the spectrum. Figure 4.1a shows the wind field predicted by SeaCluse. The streamlines are distributed symmetrically with respect to verticals through the crest or trough. Mestayer et al. already commented that this is an oversimplified representation of the flow field.

Figure 4.1b shows the streamlines predicted by the semi-analytical model. As was presented in chapter 3, this model yields predictions of the air flow that are in good agreement with experimental evidence (e.g., by Hsu and Hsu 1983). Hence, application of this wind field in SeaCluse is expected to lead to more realistic droplet trajectories.

4.4.2   Results

Droplet trajectories

Figure 4.2 shows several examples of droplet trajectories calculated by the pre-processor in a frame of reference moving with the wave. The smaller droplets, e.g., with a radius $r = 10$ μm, approximately follow the mean wind field. In the original model the circulating flow (figure 4.1a) lifts droplets ejected from the leeside of the crest up to above the critical height. There the horizontal wind speed is higher than the wave speed, so that the droplets are taken to the windward side of the wave, where they are transported back to the surface (figure 4.2b). Droplets released nearer
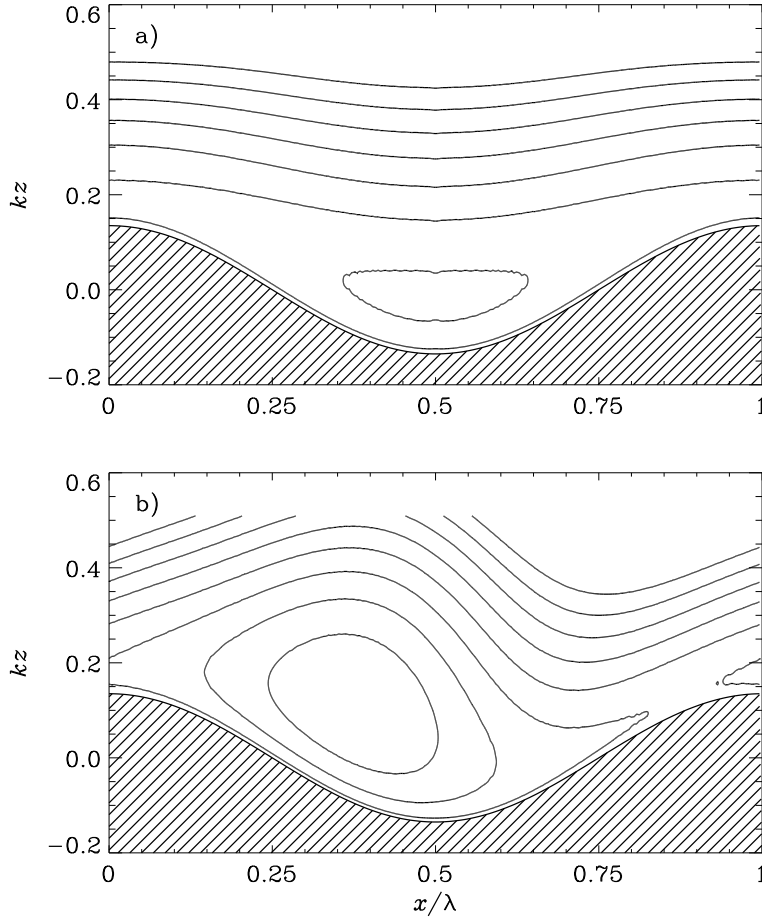
Figure 4.1: Contour plot of streamlines above a wave according to (a) the original SeaCluse, and (b) the semi-analytical model. The parameters for these plots are: $U_{10} = 20$ m s^{-1}, $c = 17$ m s^{-1}, and $ak = 0.135$. The wind is blowing from left to right.

to the crest are only transported backwards and are not captured by the wave rotor (figure 4.2a). Those released at the windward side of the wave fall back in the water immediately, because they feel a downward motion of the air (not shown). Droplets with radii up to 20–30 μm are still trapped by the circulating air flow. Figure 4.2c shows that for a 20-μm droplet the gravitational fall already becomes significant: the trajectory is not symmetrical anymore. For large droplets, the upward motions are too weak to carry them upwards (figure 4.2d). The semi-analytical model also predicts a circulating flow but the circulation is shifted to the leeside of the crest.
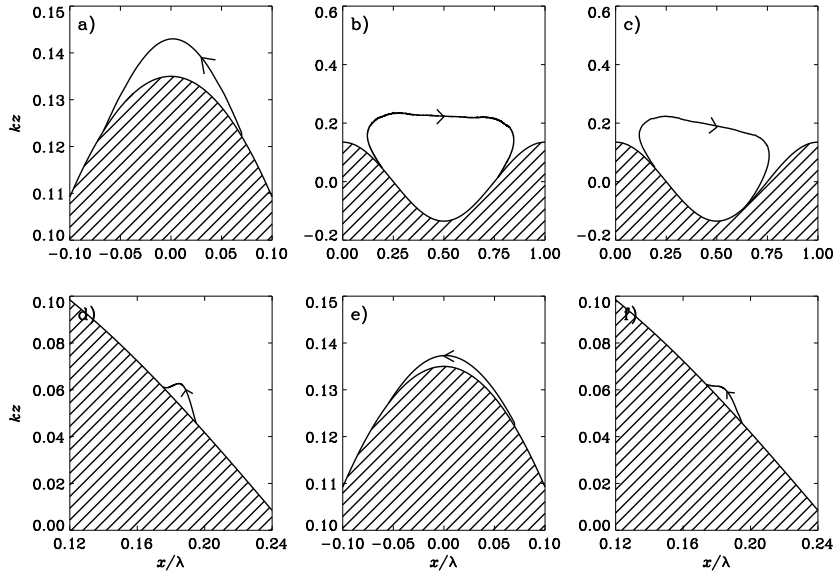
Figure 4.2: Droplet trajectories for different radii, locations of ejection, and air-flow models: (a)–(d), original wind field; (e)–(f), semi-analytical model; (a), (b), and (e), $r = 10$ μm; (c), $r = 20$ μm, (d) and (f), $r = 210$ μm.

This flow does not allow any droplets to reach far from the water surface. While the droplets released near the crest follow similar trajectories as in the original wind field (figure 4.2e), those ejected further from the crest stay close to the water surface (not shown). Since large droplets are insensitive to the air flow, both models yield similar trajectories for them (cf. figures 4.2d and f).

Flight times

Figure 4.3 shows the resulting flight times for small droplets. As was noted, droplets released on the windward side of the crest all quickly fall back into the water. For the droplets released on the lee-side, the resulting flight times depend strongly on the air-flow model. Whereas the original flow field leads to flight times of more than 1 minute, the semi-analytical model keeps the droplets airborne for only a few seconds. Note that the latter model yields maximum flight times at the locations $x/\lambda = 0.25$ and 0.75. The corresponding droplets move very close to the water surface and fall back when they reach the crest or trough, respectively.

The above illustrates that the use of a different model for the wind field yields considerably different droplet trajectories. However, only two characteristics from
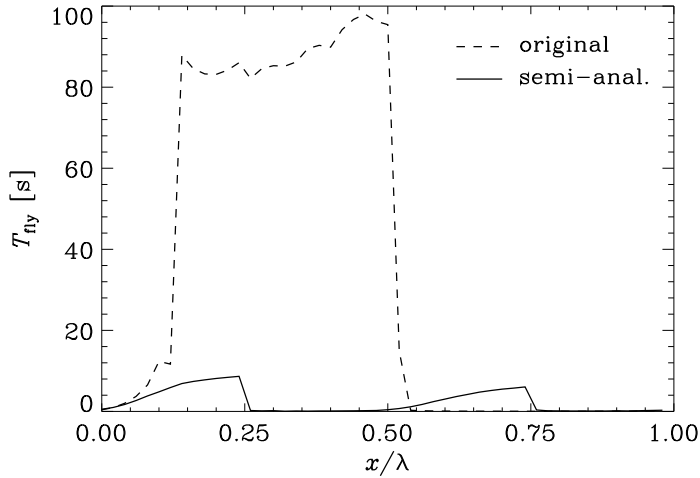
Figure 4.3: Flight time of 10-μm droplets as a function of the location of ejection.

the pre-processor results are used in the main program: the average flight time, $\overline{T}_{\text{fly},n}$, and the average vertical concentration, $\rho_n^0(z)$. These quantities are calculated by releasing droplets from many, uniformly divided, positions along the horizontal coordinate.

r [μm]	10	50	90	130	170	210	250
$\overline{T}_{\text{fly}}$, original [s]	29.7	5.4	0.79	0.65	0.59	0.52	0.48
$\overline{T}_{\text{fly}}$, semi-analytical [s]	1.36	0.72	0.61	0.58	0.54	0.49	0.45

Table 4.2: Average fight times for different radii following from the pre-processor.

Table 4.2 shows an overview of average flight times for different radii predicted by both wind-field models. Two characteristics are apparent, which were already illustrated by the trajectories in figure 4.2. First, larger droplets have shorter flight times. Second, the original wind field yields much longer flight times for the smaller droplets.

Vertical spray-concentration profiles

Vertical profiles of ρ_n^0 are presented in figure 4.4. The concentrations are divided by the surface flux to avoid the issue of choosing a source funtion. The dotted line

in panel a shows that, without turbulence, 10-μm droplets reach up to around 8 m above the instantaneous wave surface. The dash-dotted line, which is hardly visible, reflects that, when the semi-analytical model is used to calculate the air flow, the droplets stay very close to the water surface. For heavy droplets, it is not important which air-flow model is used. The dotted and dash-dotted lines in figure 4.4b almost coincide. Note that these profiles themselves have no real physical meaning. They only represent the part of the transport by the mean flow, and still have to be combined with turbulent diffusion.
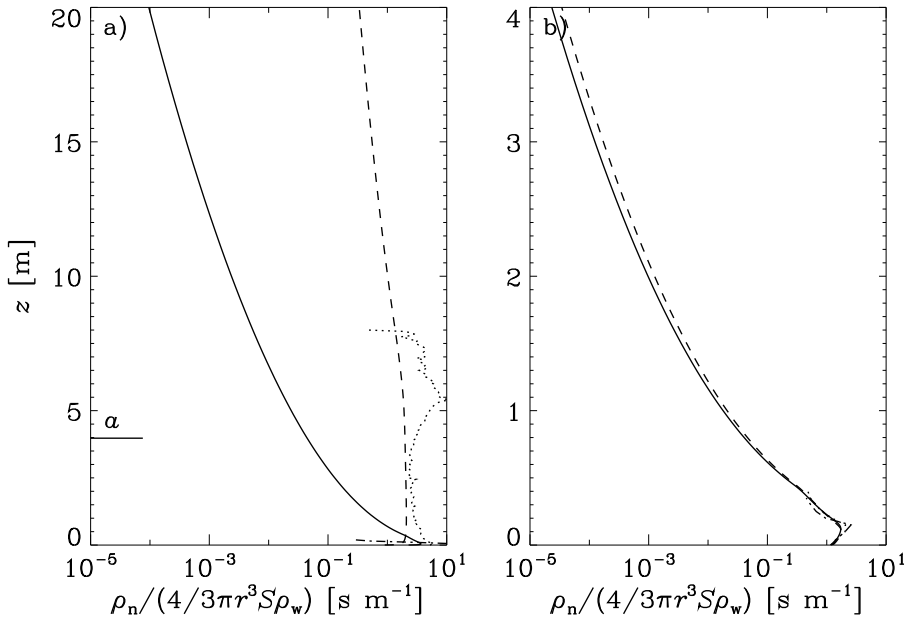

Figure 4.4: Vertical profiles of spray concentration ρ_n divided by the surface flux (S is the spray production rate, see section 5.2.4): (a) $r = 10$ μm, and (b) $r = 210$ μm. The meaning of the lines is: ———, semi-analytical; — — —, original. The 'no-turbulence' profiles, $\rho_n^0(z)$, from the pre-processor are also plotted: — · —, semi-analytical; · · ·, original.

When $\rho_n^0(z)$ and $\overline{T}_{\text{fly}}$ have been calculated with the pre-processor, computations with the SeaCluse main model can be made. Because in this study we are interested in the transport of spray, the complicating influence of evaporation on the vertical spray distributions is avoided by running the model in non-evaporative mode. In this case, the spray concentration profile, $\rho_n(z)$, results from a balance between the macroscopic and turbulent fluxes, as seen from (4.4).

The influence of the pre-processor results on $\rho_n(z)$ is clearly visible in figure 4.4. The dashed line in panel a shows that, for the original wind field, the concentration of 10-μm droplets remains more or less constant up to about 5-m height. This is related to the fact that droplets reach this height even without turbulence (see the dotted line). At higher elevations, the concentration decays, but relatively slowly. When the semi-analytical wind field is used, the decay of the concentration with height starts at a much lower height (see the solid line in figure 4.4a). The vertical gradient is also larger, which is due to the lower value of $\overline{T}_{\text{fly}}$. Larger droplets are much less influenced by the air flow in the pre-processor. Consequently, the resulting concentration profiles are almost identical for both air-flow models (cf. the dashed and solid lines in figure 4.4b). The vertical gradient for 210-μm droplets is much larger than for the 10-μm droplets, not only because $\overline{T}_{\text{fly}}$ is smaller, but also because larger droplets have a lower effective eddy viscosity due to their inertia.

4.4.3   Discussion and conclusions

In this study, typical values of, amongst others, the wind speed, the wave age, and the wave steepness have been chosen. The results could be extended by varying these parameters. However, the aim of the present section is mainly to illustrate the sensitivity of SeaCluse to the air-flow field used in its pre-processor. Hence, a detailed investigation for many conditions is beyond the scope of this work.

It is important to realize that, due to some severe model assumptions, which are partly necessary because the physics is just not known, the results must be viewed in their perspective. First, the use of the pre-processor supposes that droplet motions in the mean flow can be separated from those caused by turbulence. It is not clear how valid this assumption is, in particular for high-wind conditions, when turbulence is very strong. To resolve this issue, comparison with a completely Lagrangian model, which can assess the simultaneous influence of the mean wind and its turbulent fluctuations, would be useful. A second problem is that presently only jet droplets are treated in the model, whereas at higher wind speeds spume droplets are likely to constitute most of the surface volume flux of spray. Inclusion of spume droplets in the model was already recommended by Mestayer et al. (1996) but is hardly possible since little is known about the initial conditions of spume droplets. Third, the sinusoidal wave field is an oversimplification. In particular, at high wind speeds, the air flow over steep and breaking waves should be considered in order to predict realistic droplet trajectories.

Keeping in mind the limitations of the present modelling approach, the calculations presented in this section show that the air flow has a marked impact on the distribution of relatively small droplets, i.e. with radii below a few tens of micrometers. The original SeaCluse wind field is symmetrical with respect to verticals

through the wave crest or trough, and is characterized by a circulating flow above the wave trough. The small droplets ejected from the leeside of the crest enter in this circulating flow and spend a relatively long time in the atmosphere. De Leeuw (1986) hypothesized that such a rotor-like flow might be responsible for the maximum spray concentrations observed at a few meters height above the surface. The semi-analytical model also yields a region of circulating air flow around the critical height but displaced in upwind direction. When this wind field is applied in Sea-Cluse, droplets do not enter the rotor. Consequently, the resulting flight times are much lower and the vertical concentration decreases more rapidly with height. On the basis of these simulations it thus seems unlikely that the presence of a wave rotor can explain the measurements by De Leeuw (1986).

Chapter 5

Evaporating sea spray over the ocean: a simplified model for studying feedback effects

5.1 Introduction

In the previous chapter, it was argued that, in order to estimate the contribution of sea-spray evaporation to the air–sea heat fluxes for use in weather prediction models, simplified models are necessary. Such models should capture the most important aspects of spray physics.

An important effort in this direction was made by Andreas (1992), based on the detailed calculations of the temperature and radius evolution of spray droplets emitted in fixed ambient atmospheric conditions by Andreas (1989; 1990). This temporal evolution was parameterized by the identification of time scales indicating how quickly spray droplets of a given radius exchange heat and moisture with their environment. Subsequently, the time scales were combined with a parameterization of the residence time of droplets in the air and an estimate of the spray production function, which allowed to determine the amount of sensible and latent heat that is exchanged between the spray droplets and the atmosphere. This approach gives a good description of evaporating salt-water droplets residing in the air for a limited time. However, the atmosphere is represented as a box with a fixed uniform temperature and humidity. Hence, an error is made in determining the amount of evaporation, and the effect of spray-induced changes to the atmosphere are not taken into account (see figure 5.1a).

Fairall et al. (1994) simplified Andreas' time scale reasoning. They argued that those spray droplets that are in the radius range potentially contributing to the air-sea

fluxes have time to experience a complete temperature adjustment to the ambient atmosphere. In contrast, only a small radius adjustment is experienced. Based on these assumptions they developed a two-layer model of evaporating spray in the marine surface layer. In the lower layer, spray evaporation was assumed to be uniform with height while in the upper layer it was neglected. With a number of other assumptions and parameterizations they then derived explicit expressions for the exchange of sensible and latent heat between sea spray and the atmosphere. Such explicit relations are clearly very useful for inclusion in weather prediction models. On the other hand, the validity of some of the assumptions is questionable, in particular the assumption that the droplets' radius change is small for all droplet sizes (see, e.g., Van Eijk et al. 2001). Furthermore, as in the model by Andreas (1992), atmospheric feedback effects are not taken into account. Fairall et al. (1994) included such effects via a feedback factor, which was, rather crudely, estimated from numerical simulations by Rouault et al. (1991). Recently, Kepert et al. (1999) refined the parameterization of this feedback factor.
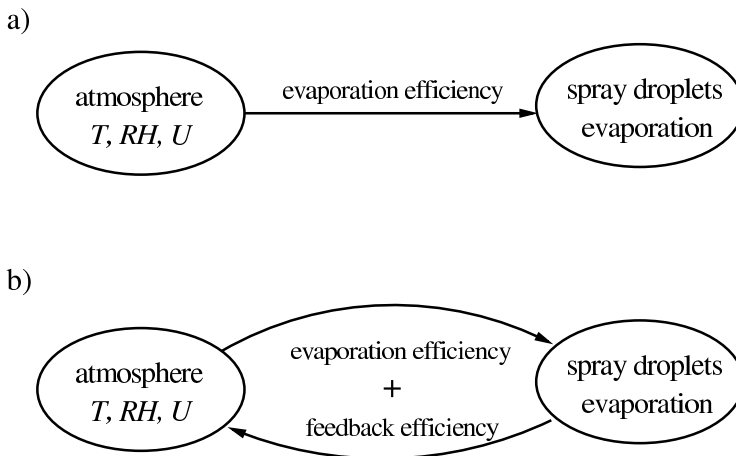
a)

b)

Figure 5.1: Outline of simplified models: a) without atmospheric feedback (e.g., Andreas 1992; Fairall et al. 1994); b) with atmospheric feedback (e.g., Makin 1998). *T* and RH are the temperature and relative humidity of the air, respectively.

Makin (1998) (hereafter M98) presented a model based on the balance equations of momentum, temperature, and humidity in the marine surface layer. An equilibrium vertical distribution of spray concentration was assumed, and the sources and sinks of heat due to these evaporating droplets were inserted in the model. The evaporation was treated similarly as in Fairall et al. (1994). The equilibrium spray distribution followed from the source function of Wu (1992), combined with an exponential decay of the droplet concentration with height. The dynamical part of the

model allows to take into account the effect of waves on the turbulence in the air. Clearly, atmospheric feedbacks can be considered with this approach (figure 5.1b).

In the present study, we elaborate on M98's model and aim at curing some of its deficiencies. Using a fixed vertical spray distribution is questionable but it constitutes the main simplifaction of the model, making its calculation time almost negligible. This feature is of primary importance in view of application of the model in numerical weather prediction. Hence, the fixed profile is retained. The review in chapter 4 has shown that an exponential decay with height is then an acceptable description. In M98's model the same decay length scale is used for all droplet sizes. As was illustrated in chapter 4, this assumption is invalid. Therefore, a fall-velocity formulation for the decay scale is employed in the present work. Another deficiency in M98's model is that it allows unlimited spray evaporation. This is cured by the introduction of an evaporation length scale. A final problem in M98 is that the source function by Wu (1992) is employed. This source function covers only the production of jet droplets, whereas both experiments and model studies indicate that most of the spray-mediated evaporation comes from spume droplets. The present study uses the source function by Andreas (1998), which covers the complete size range of droplets.

The focus in this chapter is on identifying and estimating the various feedbacks playing a role in the problem of spray evaporation. After Kepert et al. (1999), the non-interacting evaporation efficiency and the feedback efficiency (see figure 5.1) are distinguished in order to determine which proportion of the latent heat contained within the spray droplets is released in the atmosphere.

The remainder of this chapter is organized as follows. Section 5.2 contains a description of the spray model. Results of model simulations are presented in section 5.3. Concluding remarks can be found in section 5.3.

5.2 Description of the model

The model describes the stationary, fully developed, and horizontally homogeneous marine surface boundary layer. Using the Reynolds decomposition of flow variables into a mean and a fluctuating part and after horizontal averaging, the conservation

equations for mean momentum, heat and humidity can be written as

$$\frac{\partial u}{\partial t} \;=\; -\frac{\partial \overline{u'w'}}{\partial z} + \frac{1}{\rho_a}\frac{\partial \tau_w}{\partial z}, \tag{5.1}$$

$$\frac{\partial \theta}{\partial t} \;=\; -\frac{\partial \overline{\theta'w'}}{\partial z} + \frac{H_z - E_z}{\rho_a c_{pa}}, \tag{5.2}$$

$$\frac{\partial q}{\partial t} \;=\; -\frac{\partial \overline{q'w'}}{\partial z} + \frac{E_z}{\rho_a L_v}. \tag{5.3}$$

Here, u is the horizontal wind speed, θ the potential temperature, and q the specific humidity. The corresponding turbulent fluxes are $\overline{u'w'}$, $\overline{\theta'w'}$, and $\overline{q'w'}$, respectively. The horizontal averaging is performed in a wave-following vertical coordinate z as, for example, defined in equation (2.16), where h is now the top of the computational domain. The wave-induced stress τ_w describes the momentum flux caused by the presence of waves; L_v is the latent heat of evaporation of water, and c_{pa} the specific heat of moist air at constant pressure. Finally, E_z and H_z are the source terms for the transfer of latent and sensible heat, respectively, between spray droplets and the atmosphere. While the evaporation of spray leads to a source in (5.3), it is a sink in (5.2) because the heat needed for the evaporation is extracted from the air.

   Note that in the absence of spray (and waves) the turbulent fluxes of momentum, sensible heat, and latent heat are constant with height, and denoted as

$$\tau \;=\; -\rho_a \overline{u'w'}, \tag{5.4}$$

$$H_s \;=\; \rho_a c_{pa} \overline{\theta'w'}, \tag{5.5}$$

$$H_l \;=\; \rho_a L_v \overline{q'w'}, \tag{5.6}$$

respectively. The present work attempts to assess the changes to these fluxes due to waves and, in particular, evaporating spray.

   In this section, the different parts of the model will be outlined. First, the turbulence closure and the parameterization of the wave-induced stress are described. Then, the solution procedure is explained. The parameterization of the spray source terms is discussed at the end of the section.

5.2.1   Turbulence closure

For closure of the turbulent fluxes, eddy-viscosity theory is used:

$$-\overline{\phi'w'} = K_\phi \frac{\partial \phi}{\partial z}, \tag{5.7}$$

where $\phi = u, \theta$ or q. The approach in the coupled sea-surface–atmosphere model by Makin and Kudryavtsev (1999) is used here to obtain the eddy-viscosity coefficient

for momentum, K_u. They considered the conservation equation for turbulent kinetic energy (TKE), assuming a balance between production, related to both mean and wave-induced shear, and dissipation of TKE. This leads to

$$K_u(z) = \kappa z u_* \left(1 - \frac{\tau_w(z)}{\rho_a u_*^2} \right)^{1/4}, \tag{5.8}$$

The eddy-viscosity coefficients for heat and humidity are related to that for momentum via turbulent Prandtl and Schmidt numbers (we use $Pr_t = Sc_t = 1$):

$$K_\theta = K_u/Pr_t \qquad \text{and} \qquad K_q = K_u/Sc_t, \tag{5.9}$$

Atmospheric stability is taken into account by multiplying the eddy-viscosity coefficients K_ϕ by a stability function $\Phi_\phi(z/L)$, where L is the Monin-Obukhov length

$$L = -\frac{\theta_v u_*^3}{\kappa g \overline{\theta_v' w'}}, \tag{5.10}$$

Here, $\theta_v = \theta(1 + 0.61q)$ is the virtual potential temperature. Note that, due to the evaporation of spray, $\overline{\theta_v' w'}$ is not constant with height, so that L is a function of z. Standard stability functions are used (see e.g. Garratt 1992, p. 52). For $\zeta = z/L < 0$ (unstable conditions) these are given by

$$\Phi_u = (1 - 16\zeta)^{-1/4}, \tag{5.11}$$
$$\Phi_{\theta,q} = (1 - 16\zeta)^{-1/2}, \tag{5.12}$$

while for $\zeta > 0$ (stable conditions)

$$\Phi_{u,\theta,q} = 1 + 5\zeta. \tag{5.13}$$

5.2.2 Wave-induced stress

In chapters 2 and 3, models have been presented to calculate the growth rate of waves. Appendix B shortly outlines how the wave-induced stress at the surface, τ_w^0, can be related to the growth rate γ and the directional wave spectrum F. Makin and Kudryavtsev (1999) presented model calculations of the variation of the wave-induced stress with height, on the basis of which they parameterized the height dependence of $\tau_w(z)$ for a particular wave component with wavenumber k with the following function

$$f(k,z) = \exp\left(-\frac{z}{l(k)} \right) \cos\left(\frac{\pi}{2} \frac{z}{l(k)} \right). \tag{5.14}$$

Simplified model for studying feedback effects

Here, the inner region depth l is expressed as a function of k. Equation (B.11) in combination with (5.14) then gives

$$\tau_w(z) = \rho_w \int_0^\infty \int_0^{2\pi} \omega^2 \gamma(k,\theta) F(k,\theta) \cos\theta k \, d\theta f(k,z) \, dk. \tag{5.15}$$

The empirical wave-spectrum model by Elfouhaily et al. (1997) is used to evaluate $F(k,\theta)$ (see M98). The spectrum depends on the friction velocity and the wave age. For the latter, the simulations presented further on in this chapter all use a value $U_{10}/c_p = 0.83$, corresponding to a fully developed sea. The growth rate γ is parameterized as in Makin and Kudryavtsev (1999), which resembles the results from chapter 3 fairly well.

In the model, the wave-induced stress effectively leads to a suppression of the eddy viscosity near the surface. Exclusion of this term would lead to an overestimation of both momentum and heat exchange coefficients (see Makin 1999).

5.2.3   Solution

Equations (5.1), (5.2) and (5.3) are discretized on a grid extending from $z = z_0^l$ (see below) to $z = h$ with logarithmically spaced grid points. The equations require boundary conditions at the lower and upper boundary of the computational domain. In this study, fixed values are applied:

$$z = z_0^l: \qquad u = 0; \quad \theta = T_0; \quad q = 0.98 q_s(\theta_0) \tag{5.16}$$
$$z = h: \qquad u = U_h; \quad \theta = \theta_h; \quad q = \mathrm{RH}_h q_s(\theta_h), \tag{5.17}$$

where RH is the relative humidity. Note that, at the lower boundary, a salt-water correction is applied to q_s.

As described in M98, the lower boundary conditions are imposed at the height of the local roughness length, z_0^l. The approach of Makin et al. (1995) is adopted, in which all undulations of the water surface are considered to be waves, which are covered by the molecular sublayer. The instantaneous water surface can then be treated as smooth. The local roughness length is thus related to the scale of the molecular sublayer by

$$z_0^l = 0.1 \frac{\nu}{u_*^l(0)}, \tag{5.18}$$

where u_*^l is the local friction velocity

$$u_*^l(z) = u_* \left(1 - \frac{\tau_w(z)}{\rho_a u_*^2}\right)^{1/2}. \tag{5.19}$$

94

In this study, the upper boundary is located at $h = 100$ m. This height often exceeds the height of the surface layer but it is chosen to make sure that E_z (see section 5.2.4) is negligible at the top of the domain. A logarithmic discretization of the radius space between $r_{\min} = 2$ and $r_{\max} = 500$ μm is used to calculate the spray-mediated source term.

The momentum equation is solved for steady state conditions by iteratively calculating equations (5.1), (5.7), (5.8), and (5.15), in combination with equations (5.16)–(5.19), as described in Makin and Kudryavtsev (1999). Note that in this integral approach, the roughness or sea-surface drag does not have to be specified but comes out of the model as a result of the coupling between waves and the atmosphere. The heat and humidity equations are solved with an artificial time step using an implicit method. After each iteration of the momentum equation, the other equations are integrated for one time step, until all equations have reached equilibrium. With a proper choice of the time step this typically requires ten iterations.

5.2.4   Spray-mediated source terms

To complete the model, the spray-mediated source terms E_z and H_z in equations (5.2) and (5.3) have to be specified. At present, the latter of these terms, which denotes the exchange of sensible heat between spray droplets and the atmosphere, is neglected. Although, for completeness, it would be better to take H_z into account, it is argued in chapter 6 that H_z is at most 10 % of the interfacial sensible heat flux, which justifies neglecting it. The key part of the present model is the parameterization of E_z. This term is calculated on the basis of a fixed equilibrium vertical distribution of the (number) concentration of spray droplets, $n(r,z)$ (units m^{-3} μm^{-1}), which constitutes the main simplification of the model. The parameterization contains two height scales: z_f is the decay height scale of the concentration of droplets; z_e represents the decay height scale of the average size of the droplets due to evaporation.

The source term E_z is related to $E(r,z)$, the latent heat per unit volume needed to evaporate the spray droplets of a particular radius, according to

$$E_z(z) = \int_{r_{\min}}^{r_{\max}} E(r,z) \mathrm{d}r. \tag{5.20}$$

In turn, E can be expressed in terms of the rate of mass change of a single droplet, $\dot{m} = 4\pi r^2 \dot{r} \rho_w$ (units kg s^{-1}), by

$$E(r,z) = -L_v \dot{m}(r,z) n(r,z). \tag{5.21}$$

For a fresh-water droplet, $\dot{m}$ can be described by (Pruppacher and Klett 1978, p. 414 and 440)

$$\dot{m} = -4\pi \rho_a f_v D_v r (q_s - q), \tag{5.22}$$

95

where f_v is a ventilation factor, D_v the diffusivity of water vapor in air, and q_s the saturation specific humidity at the droplet temperature. The diffusivity of water vapor (units $m^2\ s^{-1}$) depends on temperature and pressure (Pruppacher and Klett 1978, p. 413)

$$D_v = 2.11 \times 10^{-5} \left(\frac{T}{T_r} \right)^{1.94} \left(\frac{p_r}{p} \right), \tag{5.23}$$

where $T_r = 273.15\ ^\circ K$ and $p_r = 1013$ hPa. In the present study, $p = p_r - \rho_a g z$ is used. The ventilation factor is the ratio of water mass fluxes from a droplet to the air for the cases of a moving and a motionless droplet. After Fairall et al. (1994), the empirical expressions in Pruppacher and Klett (1978, p. 443) are approximated by

$$f_v = 1 + 0.25 \left(\frac{2rV_f}{v} \right)^{0.5}. \tag{5.24}$$

The terminal fall velocity V_f of a droplet falling in still air is obtained from Andreas (1989; 1990)

$$V_f = \frac{2r^2 g(\rho_w/\rho_a - 1)}{9v \left[1 + 0.158(2rV_f/v)^{2/3} \right]}, \tag{5.25}$$

which is more accurate than the rough approximation used in M98, in particular for small droplets. It is assumed that the spray droplets instantaneously reach thermal equilibrium with their environment. Consequently, the droplets are maintained at the so-called evaporation temperature, which is close to the wet-bulb temperature, but includes corrections for salinity and droplet-curvature effects (Andreas 1995). In the model, these corrections are omitted, so, in equation (5.22), q_s is evaluated at the wet-bulb temperature.

In the previous chapter, vertical spray distributions, both experimentally measured and predicted with theoretical and numerical models, have been reviewed. Although a conclusive general description of the vertical concentration profile has not been established, an exponential decay with height appears to be acceptable and is adopted here. Hence, n is modelled as:

$$n(r,z) = n_0(r) \exp(-z/z_f). \tag{5.26}$$

Here, n_0 is the droplet concentration at the surface. The vertical decay length scale z_f is, in contrast to M98, taken to be dependent on radius, which is a well-established experimental and theoretical finding. The vertical decay scale is modelled as the product of the turbulent velocity scale κu_* and a droplet residence time scale τ_f, i.e. $z_f = c_f \kappa u_* \tau_f$, where c_f is a tuning constant of $O(1)$. For τ_f, the residence time scale as introduced in Andreas (1992) is used

$$\tau_f = \frac{H_{\text{sig}}}{V_f}, \tag{5.27}$$

where the significant wave height $H_{\text{sig}} = 4\langle\eta^2\rangle^{0.5}$ can be calculated from the wave spectrum (see appendix B). The choice of H_{sig} as a height scale is appropriate for spume droplets, since these form at the wave crests. For jet droplets, the ejection height seems to be a better height scale. However, these droplets quickly evaporate, so the evaporation time scale (see later, figure 5.3) determines their contribution to the evaporative fluxes and the exact parameterization of the residence time is not critical.

The droplet concentration at the surface is derived from the spray production rate $S(r)$ by assuming a balance between production and deposition

$$n_0(r) = \frac{S(r)}{V_d(r)}, \tag{5.28}$$

where V_d is the deposition velocity as given by Carruthers and Choularton (1986) (see Smith et al. 1993):

$$V_d = \frac{V_f}{1 - \exp\left[-\left(\frac{V_f}{C_D U}\right)\right]}, \tag{5.29}$$

with the values of C_D and U evaluated at 10-m height. Strictly speaking, the spray concentration should be related to the elevated height at which the droplets appear. In the model by Fairall et al. (1994), which also includes relation (5.28), this was not a problem since they assumed a constant droplet concentration with height. However, also for the present model, equation (5.28) seems to be acceptable, considering that $S(r)$ is poorly known. In the case that a significant proportion of the droplets evaporates, (5.28) is invalid, and n_0 must be lower than following from this balance equation. This is further discussed below equation (5.36).

M98 (and Fairall et al. 1994) calculated the spray-mediated vapor flux with relations as mentioned above. However, then an important aspect is missing. Due to evaporation, the droplets decrease in size, which in turn causes the evaporation rate to decrease. Andreas (1989; 1990) performed detailed calculations of the radius evolution of sea-salt aerosols ejected into air with a given temperature and relative humidity. He found that this can be well described by

$$r(t) - r_{\text{eq}} = (r_0 - r_{\text{eq}})\exp(-t/\tau_e), \tag{5.30}$$

where r_0 is the initial radius, r_{eq} the equilibrium radius a saline droplet will eventually reach, and τ_e the evaporation time scale. The latter denotes the time it takes for a droplet to go through $1 - e^{-1}$ of its potential radius change. It depends both on the initial radius of the droplet and on the properties of the air. Differentiation of (5.30) with respect to time gives

$$\dot{r}(t) = \dot{r}_0\exp(-t/\tau_e), \tag{5.31}$$

where $\dot{r}_0 = \dot{r}(0) = -\tau_e^{-1}(r_0 - r_{eq})$. Now, we assume that the average time a droplet has spent in the atmosphere is proportional to its height above the surface. This assumption allows to translate the decrease in evaporation rate with time, equation (5.31), to a decrease with height. The expression for the evaporation rate, (5.22), then becomes

$$\dot{m} = -4\pi\rho_a f_v D_v r(q_s - q) \exp(-z/z_e), \tag{5.32}$$

where the characteristic height scale for evaporation is $z_e = c_e \kappa u_* \tau_e$ with c_e a second tuning constant. The evaporation time scale, in turn, can be related to the initial radius change (see under equation (5.31), with $r_{eq} = 0$). It is estimated as

$$\tau_e = -\frac{4\pi r_0^3 \rho_w}{\dot{m}_{0,av}}, \tag{5.33}$$

where, for a particular radius, $\dot{m}_{0,av}$ is evaluated from (5.22) at the height below which half of the total vapor flux for this radius is generated. Since this height is not a priori known, it is based on the previous model iteration. The procedure aims to relate the evaporation time scale to the 'average' atmospheric conditions encountered by droplets of a certain initial radius.

One additional aspect needs to be considered. The model presented so far can lead to the predicted total spray evaporation rate E_r for a particular radius exceeding the potential evaporation rate $E_{p,r}$. Here

$$E_r = \int_0^h E(r,z)\mathrm{d}z, \tag{5.34}$$

and $E_{p,r}$ is the spray-mediated latent heat flux if all the droplets produced from the water surface evaporated to dryness (see Kepert et al. 1999)

$$E_{p,r} = \frac{4}{3}\pi r^3 \rho_w L_v S(r). \tag{5.35}$$

The inconsistency can be cured by simply adjusting E_r to $E_r' = \max(E_r, E_{p,r})$. However, we have chosen to apply a smoother filter

$$E_r' = \left(\frac{1}{E_{p,r}^2} + \frac{1}{E_r^2} \right)^{-1/2}, \tag{5.36}$$

which also has the desired properties that $E_r' \leq E_{p,r}$ and that $E_r' \approx E_r$ when $E_r \ll E_{p,r}$. If E_r has to be significantly reduced, it means that a large proportion of the droplets evaporates. In this case the balance equation (5.28) is not valid anymore; an additional sink due to evaporation should be added in the right-hand side. Thus, an adjustment of E_r is interpreted as a reduction in n_0 compared to what follows from equation (5.28).

Tuning

Before the parameterization for spray evaporation can be applied, the tuning constants c_f and c_e have to be determined. To this end, results obtained with the detailed numerical model by Kepert et al. (1999), which was discussed in chapter 4, are used. In their figure 14.10, the evaporation efficiency $E_r/E_{p,r}$ (see section 5.3) is plotted for varying radius for a potential evaporative flux of 1 W m^{-2}. The present model was run for the same atmospheric conditions with a spectrum of droplets with radii $2\ \mu\text{m} < r < 500\ \mu\text{m}$ such that $E_{p,r} = 1/(500-2)$ W m^{-2} μm^{-1}. Subsequently the two constants were tuned so that the predicted evaporation efficiency was close to that from Kepert et al.'s figure 14.10. The tuning resulted in $c_f = 1.1$ and $c_e = 0.4$, respectively. Figure 5.2 shows the result of the tuning procedure: the difference
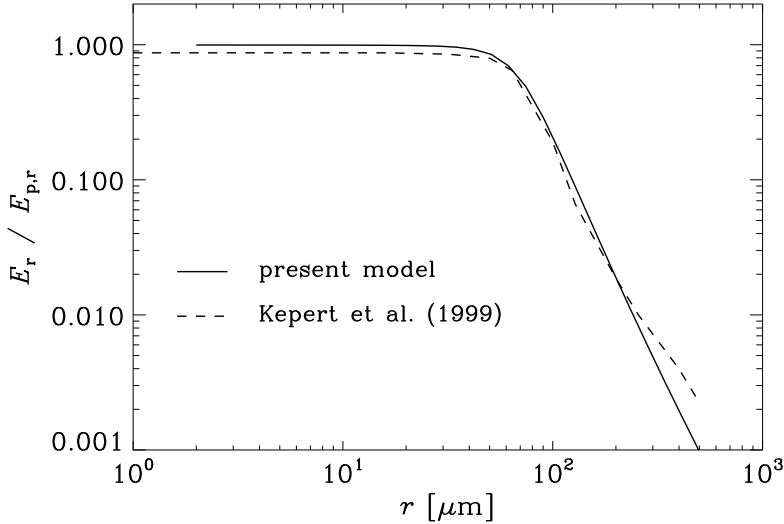

Figure 5.2: Evaporation effi ciency $E_r/E_{p,r}$ as a function of radius for this study and Kepert et al. (1999). The conditions are: $U_{10} = 25$ m s^{-1}, $T_0 = 27\ ^\circ$C, $T_h = 26\ ^\circ$C and RH= 80%. The total potential latent heat flux is 1 W m^{-2}.

between both curves is small, indicating that the model is able to reasonably reproduce the evaporation rates from a detailed numerical model which takes the major physical sea-spray processes into account.

Up to a radius of $r \approx 50\ \mu$m the droplets completely evaporate. Hence, in the present fresh-water model the evaporation efficiency is 1. In the model by Kepert et al. (1999), salinity is taken into account, so that droplets do not evaporate more

than half their size for these circumstances. Consequently, the evaporation efficiency cannot become higher than $1 - (1/2)^3 = 0.875$. For larger droplets, the evaporation efficiency decreases because of their limited residence time in the atmosphere. Because in this particular case only few droplets evaporate ($E_p = 1$ W m^{-2}), their influence on the atmospheric humidity and temperature is negligible. As a result, the decrease in efficiency cannot be related to negative feedbacks from the atmosphere. Such feedbacks receive attention in section 5.3.2.
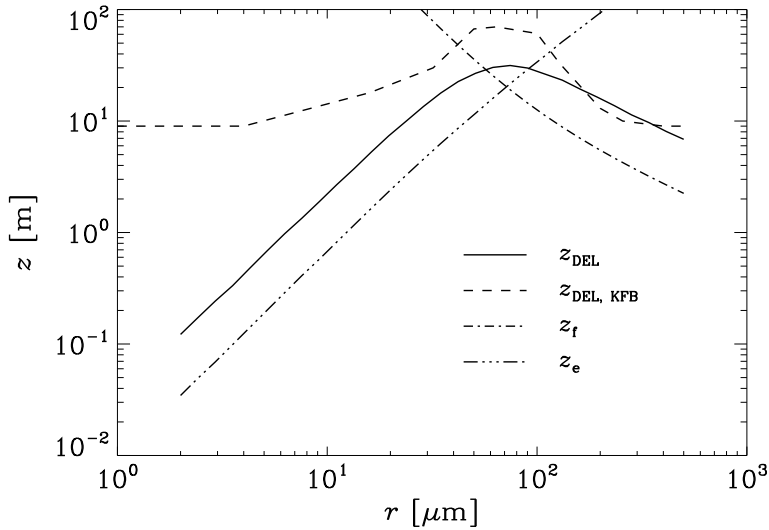

Figure 5.3: Height scales z_f and z_e, and DEL depth z_{DEL} as a function of radius for the same conditions as figure 5.2. The DEL depth predicted by Kepert et al. (1999) is also plotted.

Figure 5.3 shows the dependence of the various height scales on radius. For small droplets ($r < 50$ μm), z_e limits evaporation. These droplets have a long residence time and reach far above the surface, but quickly evaporate, so that at larger heights they are not thermodynamically active anymore. For large droplets ($r > 100$ μm), z_f limits evaporation. In this size range, the droplets have a relatively short residence time, and thus hardly time to evaporate (see figure 5.2). For droplets with radii $50 < r < 100$ μm, both height scales are of the same order. These droplets have time to evaporate a substantial part, but not all of their mass.

Kepert et al. (1999) defined the droplet evaporation layer (DEL) depth, z_{DEL} as the height below which 95 % of the total spray-mediated latent heat flux is formed. Figure 5.3 compares predictions of z_{DEL} presented by Kepert et al. (figure 14.11) with the present model. Although the latter produces a generally thinner DEL, the

dependence on radius is similar, except for small droplets, which have a much thinner DEL in our model. Both models give a maximum around 70-μm radius. The difference for small droplets is due to the fact that Kepert et al. released all the droplets at the height of the significant wave amplitude above the mean water surface. However, the smaller droplets are predominantly film and jet droplets, so the ejection height would probably be a more appropriate height to release them. In the present model, H_{sig} is used to determine z_f for all droplets but the droplets are assumed to be released at the surface.

In order to check whether the parameterization of E_z gives a good quantification of spray evaporation for a wider range of atmospheric conditions, more detailed comparison with advanced numerical models would be desirable. For the moment, we trust that the model is indeed general enough. Still, some parts are open for improvement. In particular, the salinity of the spray droplets should be taken into account. In case of a humid atmosphere this will certainly lead to lower evaporation rates.

5.3   Model simulations

The main input paramters to the model are the 10-m wind speed, the relative humidity of the air, and the temperature of the air, while the air–sea temperature difference is additionaly important for stability effects. In this section, results of model simulations are presented and the dependence on the above parameters is illustrated. The main goal of the modelling work is to quantify the net effect of spray on evaporation from the sea surface. To this end, partly following Kepert et al. (1999), several latent heat fluxes are distinguished, reflecting the successive proportions of the potential flux that finally determine the effect on the atmosphere.

The potential spray evaporation rate E_p is obtained by integrating $E_{p,r}$, equation (5.35), over radius, from r_{min} to r_{max}. Similarly, the actual spray-mediated latent heat flux is found by integration of E_r, equation (5.34). Two cases are distinguished. First, the atmosphere does not respond to the evaporating droplets (cf. figure 5.1a). The resulting spray-mediated latent heat flux is termed Q_{ln}. In the second case, atmospheric feedback is taken into account (cf. figure 5.1b). The corresponding flux, termed Q_{li}, may then also be obtained from the divergence of the turbulent flux (provided that spray evaporation is negligible at the top of the model domain)

$$Q_{li} = \rho_a L_v \left(\overline{q'w'}_h - \overline{q'w'}_0 \right). \tag{5.37}$$

The final change in the latent heat flux at the top of the surface layer, compared to the situation without spray, is denoted by Q_l:

$$Q_l = \rho_a L_v \left(\overline{q'w'}_{h,\text{spray}} - \overline{q'w'}_{\text{no spray}} \right). \tag{5.38}$$

Associated with these fluxes are the following fractions: the non-interacting evaporation efficiency $\alpha_n = Q_{ln}/E_p$, the feedback factor $\alpha_f = Q_{li}/Q_{ln}$, and the realization factor $\alpha_r = Q_l/Q_{li}$. The latent heat flux realized at the top of the surface layer in the presence of spray H_l^s can now be written as

$$H_l^s = H_l + Q_l = H_l + \alpha_r Q_{li} = H_l + \alpha_r \alpha_f Q_{ln} = H_l + \alpha_r \alpha_f \alpha_n E_p. \qquad (5.39)$$

This states that the product of the three factors introduced in this section determines what fraction of the potential evaporative flux is finally felt by the atmosphere above the droplet evaporation layer.

5.3.1   Simulations without atmospheric feedback

A key input for any spray model is the spray source function. In our model this determines the surface concentration of droplets n_0 (see equation (5.28)). M98 based n_0 on the source function by Wu (1992), which considers only jet droplets. Thus, it probably underestimates the production at larger radii, which predominantly consists of spume droplets. In the present study, the surface concentration is derived from the spray production function presented by Andreas (1998) (hereafter A98). Figure 5.4
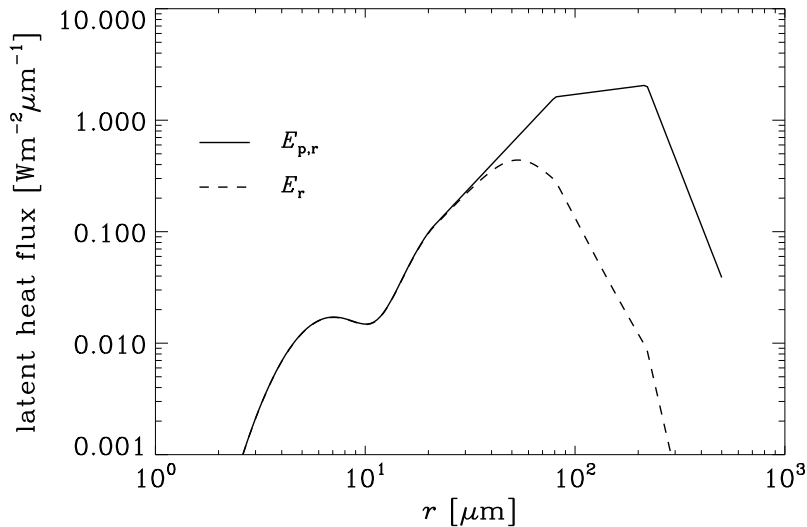

Figure 5.4: Model prediction of the spray evaporation rate E_r as a function of radius $(---)$. The solid line shows the A98 source function expressed in potential spray evaporation $E_{p,r}$ (———). The conditions are: $U_{10} = 20$ m s^{-1}, $T_0 = 15$ °C, $\theta_h = 13$ °C, and RH$_h = 80$ %.

shows this function for a wind speed of 20 m s^{-1} expressed in potential evaporation (solid curve). The (spume) droplets with radii between 100 and 200 μm carry most of the mass but according to the model these droplets evaporate only a small fraction (cf. the dashed curve) due to their limited residence time in the atmosphere. For these particular atmospheric conditions, the 50–60-μm droplets contribute most to the spray-mediated latent heat flux. Although the even smaller (mainly jet) droplets, with radii up to 30 μm, completely evaporate, their contribution to the total flux is almost negligible because they have little mass. In general, the droplets in the intermediate radius range, 30–100 μm, are the main contributors to the total spray-mediated latent heat flux, as was also concluded by, for example, Andreas (1992) and Van Eijk et al. (2001). To what extent these droplets can evaporate, depends on the relative magnitudes of z_f and z_e.
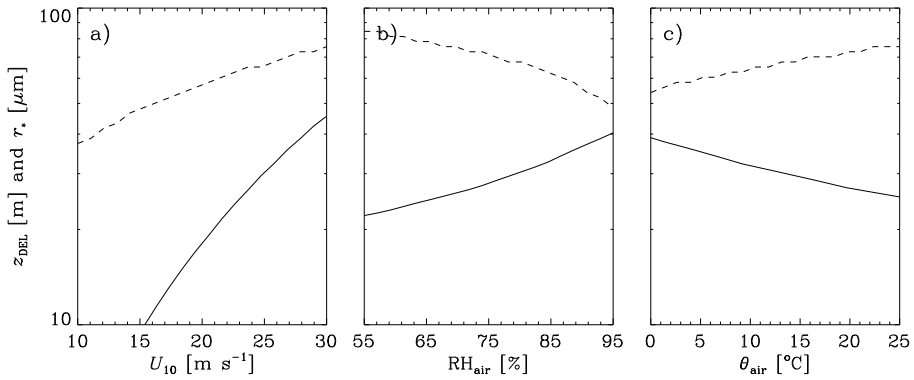

Figure 5.5: Depth of the droplet evaporation layer z_{DEL} (——) and radius r_* at which the DEL depth has a maximum ($- - -$) as a function of a) wind speed, b) relative humidity of the air, and c) temperature of the air. While in each plot one parameter is varied, the others are kept fixed at $U_{10} = 25$ m s^{-1}, RH$_h$ = 80 %, θ_h = 13 °C, respectively. For all runs, the air–sea temperature difference is $\theta_h - T_0 = -2$ °C.

Insight in the effects of these height scales is given in figure 5.5, which shows, for various conditions, the depth of the DEL, here related to the total spray evaporation. Figure 5.5 also shows r_*, the radius with maximum DEL depth

$$z_{\mathrm{DEL}}(r_*) = \max_{r} [z_{\mathrm{DEL}}(r)]. \tag{5.40}$$

The characteristic features in this figure can be explained by evaluating the consequences for the z_f- and z_e-curves in figure 5.3 of changes in the atmospheric conditions. Both z_f and z_e are proportional to u_*. Moreover, z_f is also proportional to H_{sig}, that is to U_{10}^2 in the case of a fully developed sea, which is assumed here. Hence,

the effect of increasing wind speed (figure 5.5a) is a strong growth of z_{DEL}. Also, for increasing wind speed, the maximum DEL depth occurs at a larger radius because z_f increases faster than z_e. The effect of a higher relative humidity (figure 5.5b) is an increase in z_e because the droplets evaporate more slowly. This leads to a higher z_{DEL} and a lower r_*, respectively. A higher air temperature allows faster evaporation, thus a lower z_e, resulting in a thinner DEL, with the maximum depth reached at a higher radius (figure 5.5c). Note that the quantities in figure 5.5 are insensitive to the water temperature. The features described above can help to explain the resulting spray-mediated fluxes.
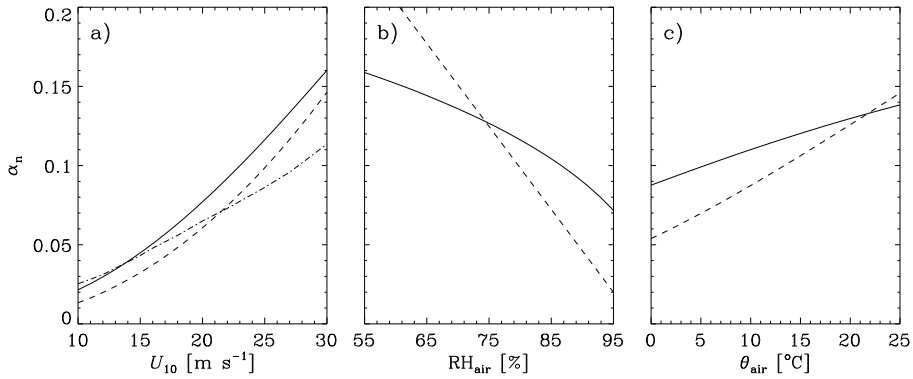

Figure 5.6: As figure 5.5 but here the non-interacting evaporation efficiency α_n is plotted: ——, present model; $---$, Fairall et al. (1994) corrected for the A98 source function (see text); $-\cdot-$ (panel a only), Andreas (1998).

Figure 5.6 shows the non-interacting evaporation efficiency α_n, defined below equation (5.38), as a function of various parameters. A large dependence of α_n on wind speed is observed. Stonger winds cause longer residence times, so that a larger fraction of the spray can evaporate (figure 5.6a). Evaporation is also enhanced in a dry and warm atmosphere (figures 5.6b and c) because the quicker evaporation allows larger droplets to lose a substantial part of their mass. Note that these curves are qualitatively the same as the r_*-curves in figure 5.5. The produced volume flux increases with radius up to $r \approx 200\,\mu$m (figure 5.4). A higher r_* is similar to moving the peak of the dashed curve in figure 5.4 to the right, which also implies a higher evaporation rate.

As was mentioned in the introduction, Fairall et al. (1994) derived explicit expressions for what would be termed the non-interacting spray-mediated heat fluxes

in the present context. They considered both the fluxes of sensible and latent heat

$$Q_{sn} = 6.4 \times 10^{-8} U_{10}^{3.4} \Gamma \rho_a c_{pa} (T_0 - T), \tag{5.41}$$

$$Q_{ln} = 7.2 \times 10^{-9} U_{10}^{5.4} \Gamma B(T) \rho_a L_v (q_s(T) - q), \tag{5.42}$$

where T and q are the temperature and specific humdity of the air, respectively, at a certain reference height z_r. The function Γ corrects for the difference between this reference height and the depth of the droplet evaporation layer, which Fairall et al. estimated as $z_{\text{DEL}} = 0.015 U_{10}^2$:

$$\Gamma = 1 - \frac{C_E^{1/2}}{\kappa} \ln \frac{z_r}{z_{\text{DEL}}}, \tag{5.43}$$

The function B reflects the fact that, while evaporating, the spray droplets are maintained at the evaporating temperature, which is the wet-bulb temperature corrected for salinity and droplet curvature effects, rather than at the air temperature (Andreas 1995):

$$B(T) = \left(1 + \frac{\varepsilon L_v^2}{R_a c_{pa} T^2} q_s(T)\right)^{-1}. \tag{5.44}$$

Here $\varepsilon = 0.622$ and R_a is the gas constant for dry air.

The evaporation efficiency following from the Fairall et al. (1994) model is also plotted in figure 5.6. To make a fair comparison, the A98 source function has been used in their model rather than the one on which (5.42) is based. This has been accomplished by correcting their equations (5) and (14) for the A98 source function. The parameterization then yields a very similar variation of the evaporation efficiency with wind speed compared to the present model predictions (figure 5.6a). In contrast, the dependencies on relative humidity and temperature are different (figures 5.6b and c). These differences are caused by the property of the Fairall et al. model that the spray-mediated latent heat flux can exceed the potential one, which will in particular happen at the smaller radii. Hence, in conditions favourable for evaporation, that is a dry and warm atmosphere, the model will probably overpredict α_n. On the other hand, for cool and moist conditions, the present model predicts higher evaporation efficiencies. The reason for this is that it will react to such conditions by increasing the DEL depth, so that still relatively large spray-mediated fluxes are possible.

Andreas (1998) used the model presented in Andreas (1992) in conjunction with his newly developed source function to estimate values of Q_{ln}. Some of his results (see his figure 5) are shown in figure 5.6a by the dash-dotted curve. They exhibit a smaller increase of α_n with wind speed. Part of the difference (but not all) can be explained by the present model not taking into account salinity. As a result, droplets

can completely evaporate. The saline droplets in the Andreas (1998) model will not shrink below half of their initial radius for RH = 80 %. As the wind speed, and thus the droplet residence time, increases, larger droplets will be able to evaporate most of their mass. These larger droplets contribute more to the total spray production (cf. figure 5.4), and thus the fact that they do not completely evaporate becomes more important. At higher relative humidities the present model will overestimate spray evaporation even more because the limiting effect of salinity becomes more important. Another aspect is that Andreas (1998) considers the atmosphere as being homogenous, whereas here the wind speed, temperature and relative humidity vary with height as in a realistic surface layer. Hence, the Andreas model neglects the fact that close to the water surface, where many droplets are present, the conditions for evaporation are less favourable. This then leads to an overestimation of α_n, in particular at low wind speeds, when the droplets stay closer to the surface.

5.3.2   Atmospheric feedback

Through their evaporation, the spray droplets modify the vertical profiles of temperature and humidity. This induces a negative feedback on both the interfacial and spray evaporation. While, so far, this feedback has been neglected, it is now taken into account. Figure 5.7 shows typical effects of the evaporating spray on the atmosphere. Due to the evaporation of spray, the profiles of temperature and humidity deviate from the usual logarithmic ones (figures 5.7a and b). The surface layer becomes cooler and moister. Due to the imposed fixed temperature at the top of the domain, the temperature profile even has a positive gradient above a height of around 10 m. This corresponds to a negative value of the sensible heat flux (figure 5.7c). While the heat fluxes are constant with height in the absence of spray, the evaporation of spray causes a strong height dependence. Near the surface, the sensible heat flux is enhanced due to spray-induced cooling. Likewise, the latent heat flux decreases near the surface. At the top of the domain, the net effect of spray evaporation is visible: an enhanced latent and reduced sensible heat flux. As was noted, the sensible heat flux changes sign compared to the no-spray case.

From figure 5.7d the spray-mediated heat flux Q_{li}, defined in equation (5.37), is read to be 143 W m^{-2}. If atmospheric feedback were neglected, this would have been $Q_{ln} = 161$ W m^{-2} (not visible in figure 5.7). The ratio α_f characterizes the negative feedback on spray evaporation due to spray-induced changes in the temperature, humidity and turbulence structure of the surface layer. This feedback factor equals 0.89 for the present case. Additionally, the realization factor α_r, determining which proportion of Q_{li} is realized at the top of the model domain, can be inferred from figure 5.7d: $\alpha_r = 0.83$.

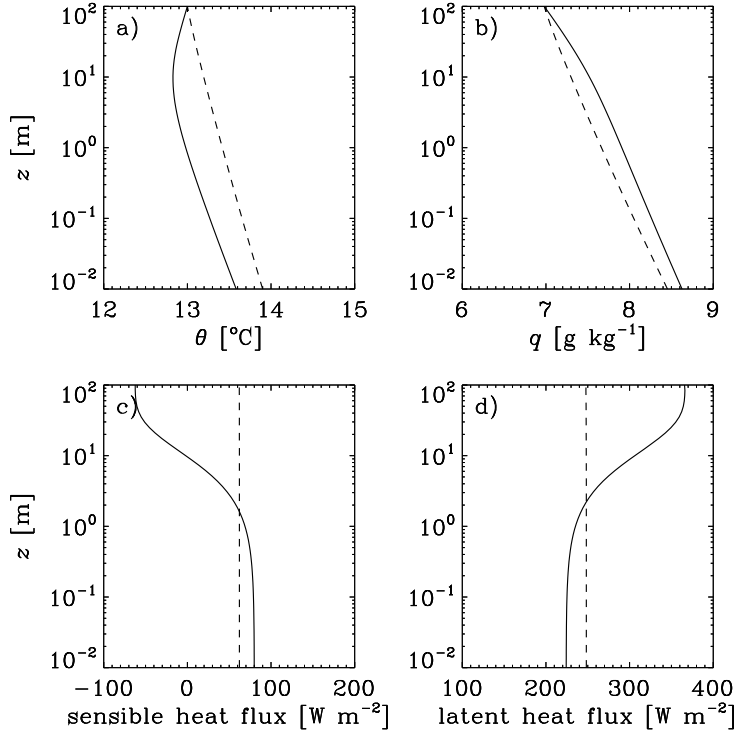Apart from for the latent heat flux, the realization factor can also be defined for

Figure 5.7: Vertical profiles of a) temperature, b) specific humidity, c) sensible heat flux $\rho_a c_{pa} \overline{\theta' w'}$, and d) latent heat flux $\rho_a L_v \overline{q' w'}$: $---$, without spray; ——, with spray. For this case, $U_{10} = 25$ m s^{-1}, $T_0 = 15$ °C, $\theta_h = 13$ °C, and RH$_h = 80$ % were used.

the sensible heat flux:

$$Q'_l = \rho_a c_{pa} \left(\overline{\theta' w'}_{h,\text{spray}} - \overline{\theta' w'}_{\text{no spray}} \right), \tag{5.45}$$

and $\alpha'_r = Q'_l / (-Q_{li})$. If stability effects are neglected, then $\alpha'_r = \alpha_r$. However, when stability is taken into account, the value for the sensible heat flux is typically somewhat higher. For example, $\alpha'_r = 0.87$ is found from figure 5.7c. This implies that the total heat flux realized above the DEL has decreased compared to the no-spray case. The differences are small and become smaller with increasing wind speed. Therefore, they will not be considered furtheron, and reported values of α_r are related to the latent heat flux.

Figure 5.8 shows model predictions of α_f and α_r for a range of atmospheric conditions. The feedback efficiency is strongly related to Q_{ln} itself since a large spray-mediated flux will induce strong feedbacks. Hence the strong dependence
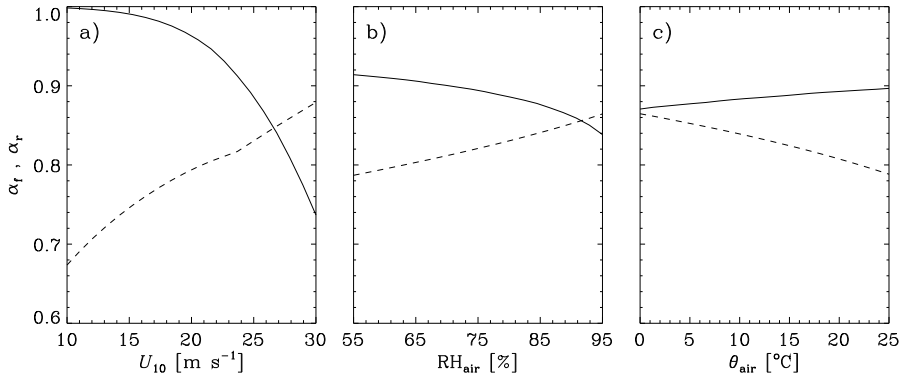
Figure 5.8: As figure 5.5 but here the feedback factor α_f (——) and the realization factor α_r (− − −) are plotted .

of the feedback factor α_f on wind speed (figure 5.8a). The variation with the other parameters is smaller. Figures 5.8b and c indicate that the feedback is reduced (larger feedback factor) when the atmosphere becomes warmer and drier.

The realization factor α_r is generally larger than 0.7, and increases with wind speed to around 0.9 for $U_{10} = 30$ m s^{-1}. It is largely determined by the depth of the DEL, which was shown in figure 5.5. At a high wind speed, a high relative humidity, and a low temperature, evaporation occurs over a deeper layer. Consequently, the reduction of the latent heat flux near the surface is relatively smaller, which implies a higher realization factor. The feature observed in the α_r-curve near $U_{10} = 23$ m s^{-1} in figure 5.5a is related to the transition from unstable to stable conditions above the DEL, and due to the non-smoothness of the stability functions on going from $\zeta < 0$ to $\zeta > 0$.

Fairall et al. (1994) introduced a feedback factor α to correct the fluxes in (5.41) and (5.42) for feedback from the atmosphere. They roughly estimated this factor, which equals $\alpha_f \alpha_r$ in the present notation, as 0.5. The feedback factor must ultimately go to zero when the spray production rates increase, since enormous amounts of spray will saturate the boundary layer by their evaporation, thus preventing further evaporation. This asymptotic behaviour is already visible in figure 5.8a, extrapolating the curves to higher wind speeds (which implies higher production rates). Nevertheless, the present results suggest that a constant factor is not a bad approximation, up to a wind speed of 30 m s^{-1}, and based on the A98 source function. The average value of α estimated from figure 5.8 is around 0.75.

At this point, a remark on the boundary conditions has to be made. Imposing fixed values for temperature and humidity at the top of the model domain, equa-

tion (5.17), limits the extent to which the vertical profiles can deviate from the shape they have in the case of no spray. A complete saturation of the surface layer, for example, is not possible even with infinite amounts of spray, because of the upper boundary conditions. Hence, negative feedback is limited and the factors α_f and α_r are probably overestimated, leading to higher realized spray-mediated fluxes than could be present in reality. This point was first made by Kepert et al. (1999). It does not seem to be possible to find other natural upper boundary conditions. Imposing fixed gradients has the same problem of presupposing a specific response of the atmosphere above the model domain to what happens in the surface layer. However, our aim is to use the flux predictions in an atmospheric model. Then, communication between the layer below the lowest level of the atmospheric model and the layers above is accomplished within the atmospheric model. Typically, an increased latent heat flux due to spray evaporation will lead to a higher relative humidity at the lowest atmospheric model level, which will in turn lead to a lower spray-mediated flux. In this way, negative feedback as mentioned above is realized within the atmospheric model. Thus, the present boundary conditions appear to be appropriate.

Figure 5.9 shows model predictions of H_l and Q_l. The latent heat flux is often described by a bulk parameterization

$$H_l = \rho_a L_v C_E U_{10}(q_0 - q_{10}), \tag{5.46}$$

where C_E is the heat exchange coefficient. According to figure 5.9a, H_l is approximately linearly dependent on U_{10}. This is equivalent to C_E being almost independent of wind speed. Note that this feature is consistent with both field measurements and theory (see chapter 1). The variation of H_l with the other parameters is explained by their influence on the $(q_0 - q_{10})$ term. Note that for sufficiently stable conditions the latent heat flux is directed downward (figure 5.9c).

The evaporation of spray adds Q_l to the latent heat flux. Clearly, this contribution depends strongly on the wind speed, mainly because the spray generation function does. A warm and dry atmosphere is also favourable for spray evaporation but figures 5.9b and c show that the spray-mediated flux does not increase as fast as the no-spray flux when the humidity decreases and the temperature increases (compare the solid and dotted lines).

An important point illustrated by figure 5.9 is that it is not really possible to capture H_l^s with a bulk formulation as (5.46). If this were attempted, the exchange coefficient C_E^s would depend in an indistinct manner on all parameters in figure 5.9. It is also not possible to say in general at which wind speed the realized spray-mediated and direct fluxes become equal. For example, according to figure 5.9a this would be 28 m s^{-1}, whereas for an air–sea temperature difference of 1 °C, it would be 25 m s^{-1} (see figure 5.9d). In other words, the relative magnitudes of H_l and
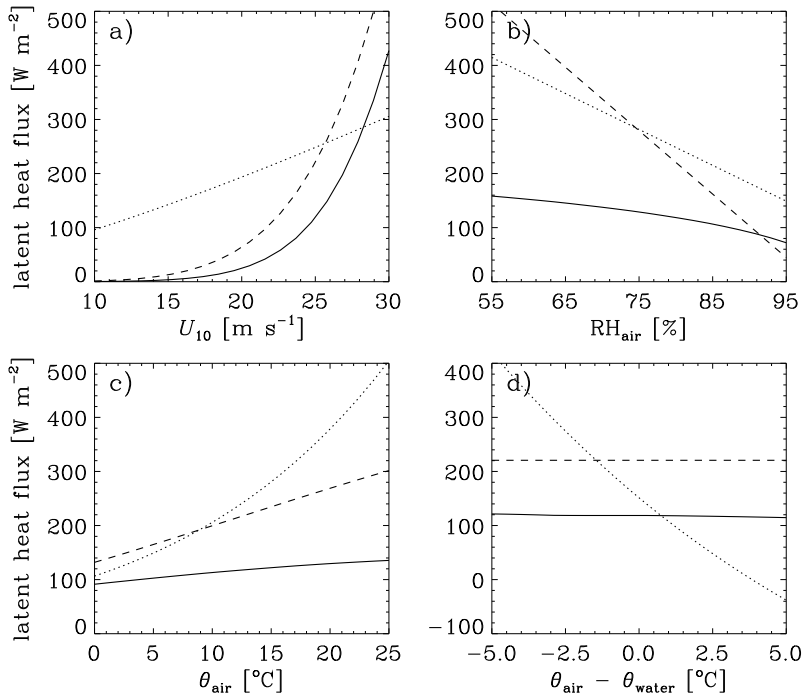
Figure 5.9: Latent heat flux in the absence of spray H_l $(\cdots)$, realized spray-mediated flux Q_l (——), and parameterization (5.42) multiplied with 0.5 $(---)$ as a function of a) wind speed, b) relative humidity of the air, c) temperature of the air, and d) air–water temperature difference. The conditions are as in figure 5.5

Q_l depend not only on wind speed but also on the air temperature and the air–sea temperature difference.

The predictions from the Fairall et al. (1994) parameterization, with $\alpha = 0.5$, are also plotted in figure 5.9. As was noted before, these are much higher than the present model results, mainly since they are based on a source function giving higher spray production rates. This points us to a major problem in spray research: the uncertainty in spray production rates.

In order to determine the sensitivity of the results to the spray production rate, figure 5.10 shows the effect of multiplying the A98 generation function with a factor varying between 0.1 and 10, leaving the radial distribution unchanged. First of all it is noted that the non-interacting evaporation efficiency is independent of the source strength. The feedback factor decreases with increasing spray production, while the realization factor slightly increases. Since α_n is unchanged, the product of α_f
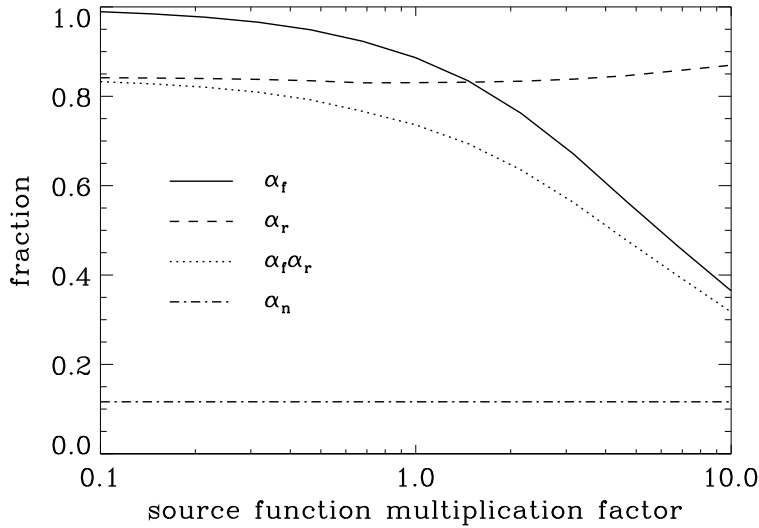
Figure 5.10: Effect of multiplying the A98 spray generation function on the fractions α_n, α_f, and α_r for the conditions as in figure 5.5.

and α_r gives the net effect of increasing the production rates on the realized spray-mediated heat flux. Suppose the production rates would be twice those of A98. Then, according to figure 5.10, the product $\alpha_f \alpha_r$ approximately changes from 0.74 to 0.65, which is a 12-% decrease. Hence, the increase in realized spray-mediated flux is not 100 % (as for the production rate) but 88 %. The fact that this difference is small means that the effect of atmospheric feedback is not very large here. Nevertheless, for even higher production rates, it becomes more and more important

The source function underlying Fairall et al.'s parameterization roughly has twice as many droplets as the A98 function. If we correct for this difference in figure 5.9 by changing the heat fluxes correspondingly, the present model predictions are much closer to Fairall et al.'s parameterization. Of course, as was discussed in section 5.3.1, differences remain, particularly in the dependence on relative humidity.

5.4 Summary and conclusions

In this chapter, a model was developed for air–sea exchange of heat and moisture in the presence of evaporating sea spray. The key part of the model is a parameteriza-

tion of the evaporation rate of an equilibrium vertical distribution of spray droplets. Advanced-numerical-model results presented by Kepert et al. (1999) were used to tune two empirical constants in the parameterization.

The model allows to investigate two-way interactions between spray droplets and the atmosphere. The atmospheric conditions determine which proportion of the spray will evaporate, which is expressed by the (non-interacting) evaporation efficiency. On the other hand, the evaporating spray causes the atmospheric conditions to change, which, in turn, influences the latent heat fluxes. This feedback has two aspects: the effects on the spray-mediated flux are reflected by the feedback factor; the effects on the interfacial flux are reflected by the realization factor. Typical values of the evaporation efficiency were found to be of the order of 0.1. The highest values occur when the wind speed is high and the air is dry and warm. The product of the feedback and realization factor was found to be around 0.75, fairly independent of the atmospheric conditions. However, this is based on the A98 spray generation function. For higher spray production rates, the feedback efficiency increases rapidly.

Concluding, the model appears to be a convenient tool for making quick estimates of the effect of evaporating spray on the air–sea heat fluxes. Future work should include taking into account the salinity of the spray droplets. Additionally, further tuning of the model for various atmospheric conditions is recommended.

Chapter 6

Impact of sea spray evaporation in a numerical weather prediction model

6.1   Introduction

The surface fluxes over the sea are important boundary conditions for atmospheric models. In many studies, the sensitivity of such models to the parameterization of surface momentum and heat fluxes has been investigated (e.g., Miller et al. 1992; Beljaars 1995). Whereas at moderate wind speeds the surface heat fluxes above the sea are reasonably known, during storm conditions a complicating factor is present in the form of sea spray. As was argued before, the fluxes might be significantly modified through the evaporation of spray droplets, which can, in turn, have effects on the atmosphere.

Especially, tropical cyclones might be sensitive to sea spray, not only because of the extreme wind speeds involved, but also because of the importance of the air–sea fluxes in their dynamics. Fairall et al. (1994) claimed that, without taking into account evaporating spray droplets, the boundary layer of a modeled tropical cyclone evolves in an unrealistic manner. Kepert et al. (1999) and Bao et al. (2000) investigated the impact of spray on the development of a simulated hurricane using a coupled atmosphere–ocean–wave model. They found that the hurricane intensity can substantially increase. Recently, Wang et al. (2001) reported only a moderate enhancement of the final intensity of a modeled tropical cyclone, whereas Andreas and Emanuel (2001) claimed a considerable intensification due to spray. In contrast to tropical storms, effects on midlatitude storms have received hardly any attention in the literature.

The goal of the present study is to assess the sensitivity of the atmosphere to sea spray evaporation over the midlatitude oceans. This is done using the numerical weather prediction (NWP) model HiRLAM (High Resolution Limited Area Model), which contains a comprehensive physics parameterization package for vertical diffusion, radiation, condensation, precipitation, and surface processes. For the purpose of this study, the impact of spray is included in the form of modified air–sea heat fluxes.

In the previous chapter, a simplified model for estimating the contribution of spray to the heat fluxes was presented. This could, in principle, be included in HiRLAM. However, for application in an NWP model it is of utmost importance to limit calculation times. Therefore, the present study will employ the bulk parameterization of the spray-mediated fluxes developed by Fairall et al. (1994). Although it was shown that these relations give somewhat different estimates than the simplified model, they seem to be sufficiently accurate for the purpose of testing the impact of spray in NWP. One must keep in mind that the largest uncertainty is the spray production function.

Two case studies of intense midlatitude storms are presented and the effects of spray evaporation on the simulations are analyzed. Although the wind speeds are not as extreme as in tropical cyclones, it is of interest to investigate whether still significant spray effects are present.

The remainder of this chapter is organized as follows. In section 6.2, the setup of the numerical simulations is outlined. This includes a description of the HiRLAM model and the inclusion of the effects of spray in it. The results of the case studies with HiRLAM are presented in section 6.3, along with a discussion. Finally, concluding remarks are given in section 6.4.

6.2   Model description

This section deals with the HiRLAM model, the parameterization of surface fluxes, and the effect of sea spray on these fluxes.

6.2.1   The NWP model

In this study we use the NWP model HiRLAM, a limited-area, hydrostatic, grid-point model, developed in a cooperation of several European meteorological institutes. We run the model on a domain covering Europe and the North Atlantic, with a horizontal resolution of 55 km and with 31 layers in the vertical. The lowest model level is located approximately 30 m above the surface. The model is driven by the

ECMWF (European Centre for Medium-range Weather Forecasts) global model; that is, lateral boundary conditions are taken from ECMWF analyses.

We use HiRLAM version 4.8.1, with the exception that the nonlocal, first-order turbulence closure scheme of Holtslag and Boville (1993) is employed for modeling vertical diffusion. The parameterization of the surface fluxes above the sea is described below. Important for determining these fluxes is the sea surface temperature (SST). The SST is analyzed using coarse-resolution satellite data in combination with buoy and ship measurements and is frozen during forecasts. For further detailed information on HiRLAM, the reader is referred to Källén (1996).

6.2.2 Surface fluxes

In HiRLAM, the surface fluxes above the sea are calculated from mean model parameters using Monin–Obukhov similarity theory. The resulting bulk formulations for the turbulent fluxes of momentum, sensible heat, and latent heat are:

$$\tau = \rho_a C_D U_{z_l}^2, \tag{6.1}$$
$$H_s = \rho_a c_{pa} C_H U_{z_l}(\theta_0 - \theta_{z_l}), \tag{6.2}$$
$$H_l = \rho_a L_v C_E U_{z_l}(q_0 - q_{z_l}). \tag{6.3}$$

Here U is the mean horizontal wind speed, θ the potential temperature, q the specific humidity, ρ_a the density of air, c_{pa} the specific heat of moist air at constant pressure, and L_v the latent heat of evaporation of water. The heat fluxes are defined positive in the upward direction. The subscript z_l denotes the lowest model level, while 0 refers to the water surface. The exchange coefficients C_i ($i = D, H, E$) are determined from their neutral counterparts C_{iN} with stability functions from Louis (1979).

The neutral exchange coefficients are given by:

$$C_{DN} = \frac{\kappa^2}{\ln^2(z_l/z_{0m})}, \tag{6.4}$$

$$C_{HN} = \frac{\kappa^2}{\ln(z_l/z_{0m})\ln(z_l/z_{0t})}, \tag{6.5}$$

$$C_{EN} = \frac{\kappa^2}{\ln(z_l/z_{0m})\ln(z_l/z_{0q})}, \tag{6.6}$$

where $\kappa = 0.4$ is the von Kármán constant, while z_{0m}, z_{0t}, and z_{0q} are the roughness lengths for momentum, temperature, and humidity, respectively. In HiRLAM, z_{0m} is calculated from the Charnock relation

$$z_{0m} = \alpha_c \frac{u_*^2}{g}, \tag{6.7}$$

115

where α_c is the Charnock constant, u_* the friction velocity, and g the acceleration due to gravity. The value $\alpha_c = 0.014$ is used over open sea, whereas $\alpha_c = 0.032$ is employed at grid points with a nonzero land-cover fraction, that is in coastal zones. The roughness lengths for sensible and latent heat are taken from Garratt (1992, p. 102):

$$\ln(z_{0m}/z_{0t}) = 2.48 Re_*^{1/4} - 2, \qquad (6.8)$$

$$\ln(z_{0m}/z_{0q}) = 2.28 Re_*^{1/4} - 2. \qquad (6.9)$$

The roughness Reynolds number is defined as $Re_* = z_{0m} u_* / \nu$, where ν is the viscosity of air. For low wind speeds, smooth-surface and free-convection regimes are included in the surface-flux parameterization. More details on the implementation can be found in Woetmann-Nielsen (1998).

6.2.3 The effect of spray on the surface heat fluxes

For the parameterization of the spray-mediated fluxes, the expressions (5.41) and (5.42) developed by Fairall et al. (1994) will be used. In addition to these 'non-interacting' fluxes, the atmospheric feedback needs to be taken into account. To this end, Fairall et al. introduced a factor α, such that $Q_l = \alpha Q_{ln}$ and $Q_s = \alpha Q_{sn}$. For this factor, which is the product of α_f and α_r (see chapter 5), they suggested a fixed value of 0.5. Bao et al. (2000) and Kepert et al. (1999) noted that α should decrease when spray evaporation increases, since higher evaporation rates enhance the negative feedback. It was shown in the previous chapter that this is indeed the case, but for the atmospheric conditions investigated there, a constant factor was appropriate. The present study uses the Fairall et al. parameterization, with $\alpha = 0.5$, rather than the $\alpha \approx 0.75$ found in chapter 5.

In figure 6.1, the spray-mediated flux estimates are plotted along with the no-spray (or direct) turbulent fluxes from (6.2) and (6.3) for more or less typical midlatitude conditions. A number of observations can be made from this figure. First, the latent heat flux over sea is normally much larger than the sensible heat flux. Second, the spray-mediated heat fluxes increase much more rapidly with wind speed than the direct fluxes. Whereas, at a wind speed of 15 m s^{-1}, Q_l is only 10 % of H_l, these fluxes are equally large for $U_{10} = 26$ m s^{-1}. Third, Q_s is small compared to H_s. Even at a wind speed of 30 m s^{-1}, and for an arbitrary choice of temperature and humidity (not shown in figure 6.1), Q_s is at most 10 % of the direct flux. For this reason, Q_s was neglected in the model presented in chapter 5.

Because the heat required for evaporation of the spray droplets is extracted from the air, the spray-mediated latent heat flux shows up as a sink in the boundary condition for sensible heat. Hence, the heat boundary conditions at the air–sea interface
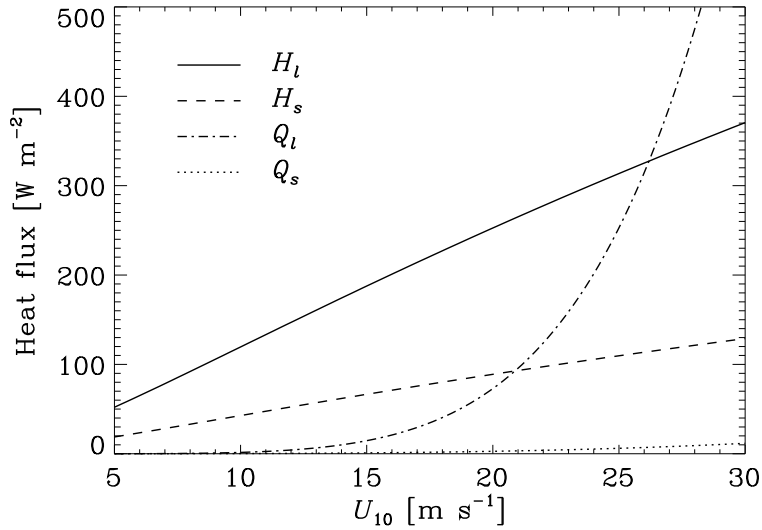
Figure 6.1: Typical magnitude of the direct and spray-mediated sensible and latent heat fluxes as a function of wind speed. The fluxes have been calculated for a water temperature of 15 °C, an air temperature (at 30-m height) of 12 °C, and an RH of 80%.

in the presence of spray become (see the previous chapter, or Fairall et al. 1994)

$$H_s^s = H_s + Q_s - Q_l, \tag{6.10}$$
$$H_l^s = H_l + Q_l. \tag{6.11}$$

These modified boundary conditions have been implemented in HiRLAM. Their impact is analyzed in the next section for two case studies of storm situations. Runs with original fluxes (H_s and H_l) will be referred to as reference runs, while those with modified fluxes will be termed spray runs.

Sea spray thus has the effect of redistributing energy from sensible to latent heat. On adding (6.10) and (6.11), we see that the total energy exchange between air and sea is, in principle, only changed by Q_s, which is small. However, the energy transport can be influenced indirectly by modifications of H_s and H_l due to, for example, changes in wind speed, temperature, and humidity at the lowest model level.

6.3 Results and discussion

In this section, two case studies with HiRLAM are presented, in which the sensitivity of the atmosphere to sea-spray-induced changes in the surface heat fluxes is studied. For both case studies, we have run the model for about four days, with a six-hour data-assimilation cycle, producing forecasts up to 48 hours.

6.3.1 Case 1

The first case concerns a storm on 1 January 1995. A low over southern Sweden and a high west of France cause strong winds over the North Sea from the north–northwest direction. The HiRLAM analysis at 1200 UTC is given in figure 6.2. The wind has been blowing with a more or less constant direction for almost 24 hours, reaching speeds of over 25 m s^{-1}. The SST of the North Sea varies between 6 $^\circ$ and 10 $^\circ$C. The advection of polar air makes the situation unstable: the air at 2-m height is on average $4 - 7$ $^\circ$C colder than the water. The air is also dry: the relative humidity varies mostly between 55 % and 75 %.
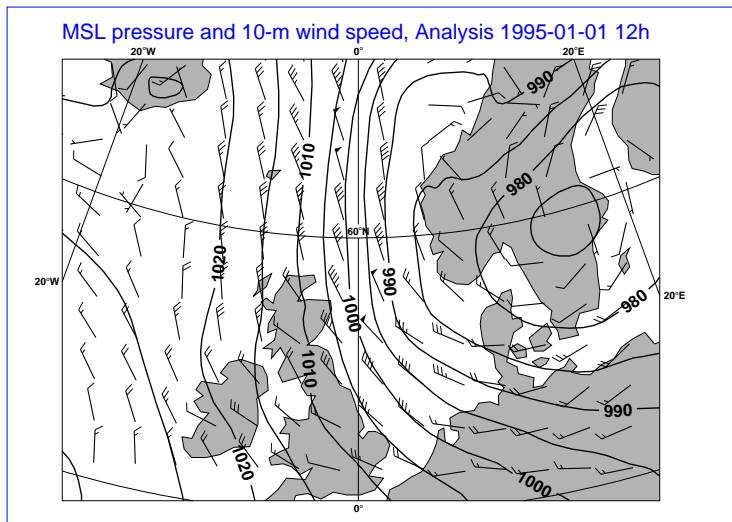

Figure 6.2: Mean-sea-level isobars and 10-m wind speed flags from the HiRLAM analysis (reference run) at 1200 UTC 01 January 1995. Meaning of the wind speed flags: half barbs correspond to 5 kts, full barbs to 10 kts, and closed 'triangles' to 50 kts (1 kt ≈ 0.514 m s^{-1}); barbs/triangles are located on the side of the wind direction.
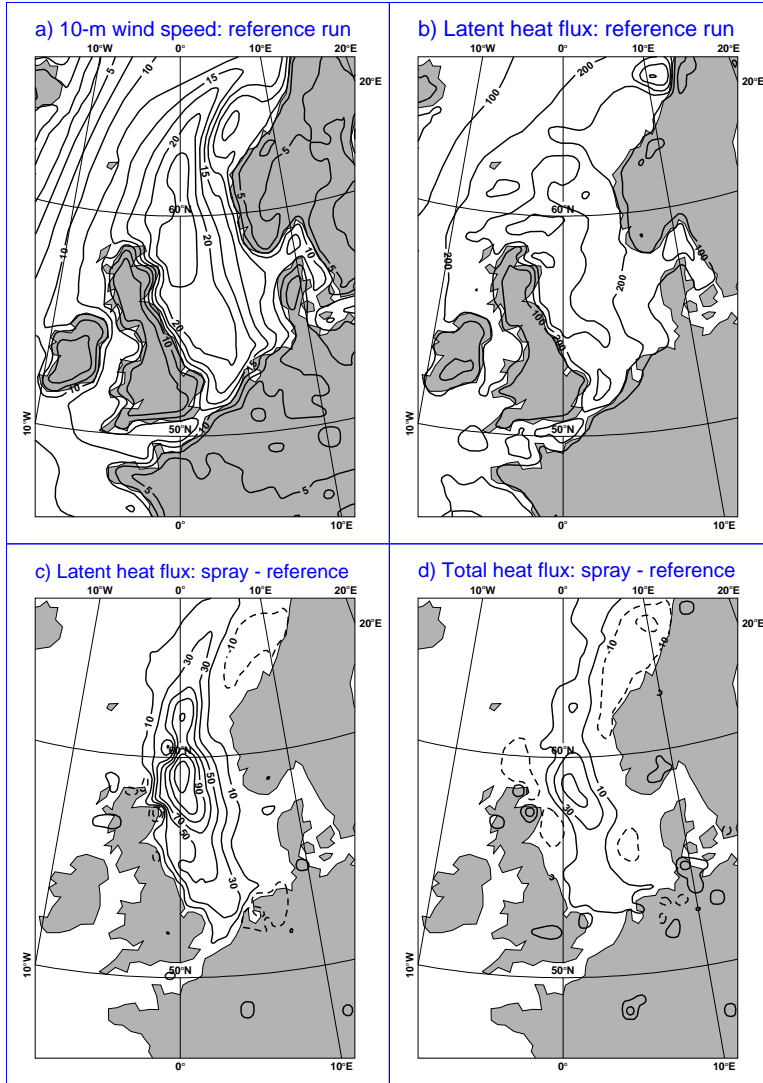
Figure 6.3: Contour plots of wind speed and heat fluxes from the 12-h forecast valid at 1800 UTC 01 January 1995: (a) 10-m wind speed from reference run, (b) surface latent heat flux from reference run, (c) latent heat flux difference (spray − reference), and (d) total (latent plus sensible) heat flux difference. Contour intervals are (a) 2.5 m s^{-1}, (b) 100 W m^{-2}, (c) 20 W m^{-2}, and (d) 20 W m^{-2}.

119

Figure 6.3 shows forecasts of wind speed and surface heat fluxes during the storm. The effect of spray on the latent heat flux is visible in figure 6.3c. Clearly, the major impact is found in the high-wind-speed regions (cf. figure 6.3a). The latent heat flux is enhanced with up to 140 W m^{-2}, which is a 40 % increase compared to the reference run (figure 6.3b). Notice that, although the spray-mediated flux Q_l is always positive, the difference between spray and reference run can be negative. This is, for example, the case in the area west of Norway, where the wind speed is very low (figure 6.3a). In this area, the air has been moistened at previous times when the wind speed was high. This has resulted in a decreased direct flux at the time displayed in figure 6.3, while the local spray-mediated flux is negligible.

Model predictions of several near-surface quantities for a particular location in the northern North Sea are presented in figure 6.4. The wind speed at this location reaches 25 m s^{-1}. During the whole period, the stratification is unstable, that is, upward heat fluxes. Due to spray, the latent heat flux is enhanced by more than 100 W m^{-2} (figure 6.4b) in the storm period. Likewise, the sensible heat flux decreases. These modifications lead to a cooler and moister lowest model level. In the model runs, the SST is kept constant during forecasts and is the same in the spray and reference runs. Therefore, figure 6.4c actually shows variations in lowest model level temperature. Note that in figure 6.4d, the relative humidity is plotted, which increases not only due to the higher specific humidity but also due to the lower saturation specific humidity caused by cooling.

The wind speed is slightly reduced due to sea spray (see figure 6.4a, in particular on 1200 UTC 01 January 1995), which is explained as follows. In the spray run, the region close to the surface is more unstable than in the no-spray run. Hence, the wind feels the surface more strongly. Higher aloft, the vertical temperature profile is stabilized. This means that less momentum is exchanged with higher levels. Those effects lead to a decrease in wind speed at the lowest model level and also at 10-m height.

The difference in the total heat flux between the spray and reference runs at the same location is analyzed in figure 6.5. Part of this difference is caused by the spray-mediated sensible heat flux Q_s, plotted with long dashes. It is observed that Q_s is generally small, reaching a maximum of around 10 W m^{-2}. The other curves in figure 6.5 show the contributions of the various parameters in equations (6.2) and (6.3) to modifying $H_s + H_l$. The partitioning into flux contributions was achieved by calculating the linear increments to the total flux due to changes in every single parameter. Figure 6.5 shows that the cooling due to spray leads to a higher direct heat flux, whereas the moistening reduces it (dashed and dash-dotted lines, respectively). Clearly, these effects do not cancel, which implies that the equivalent potential temperature at the lowest model level has changed. The inclusion of spray leads to a
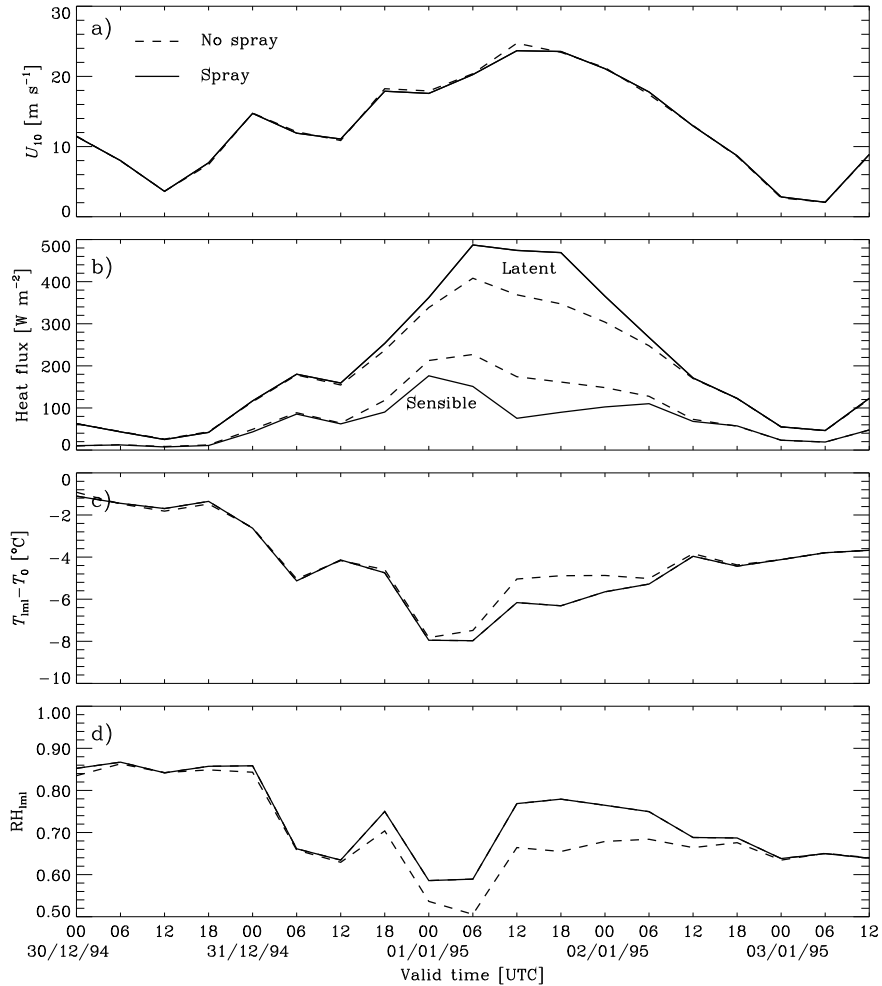
Figure 6.4: Model predictions of near-surface quantities at location (59°N,1°E) for reference (dashed line) and spray (solid line) runs: (a) 10-m wind speed, (b) surface heat fluxes, (c) difference between lowest model level (lml) temperature and SST, and (d) relative humidity at lml. The model output is taken from 12-h forecasts with valid time (time at which the forecast is valid) from 0000 UTC 30 December 1994 to 1200 UTC 3 January 1995.

121
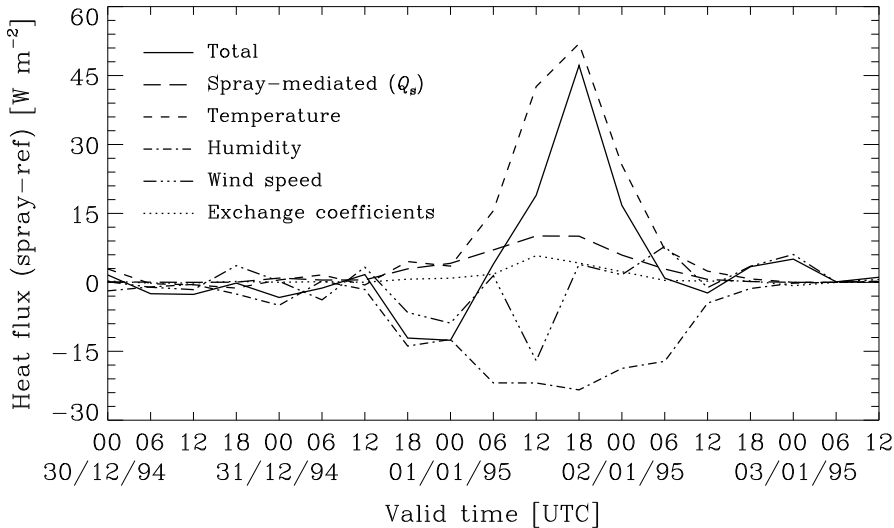
Figure 6.5: Difference in heat flux between spray and reference runs at location (59 °N,1°E): the total heat flux difference consists of the spray-mediated sensible heat flux Q_s, and differences in the direct fluxes due to changes in temperature, specific humidity, wind speed, and exchange coefficients, respectively.

decrease in wind speed, as was noted before. This in turn causes a lower direct heat flux (dash-dot-dot-dotted line). Finally, the dotted line shows the joint effect of changes in C_H and C_E. With spray, the near-surface layer is more unstable, so that the exchange coefficients are larger. This implies larger direct heat fluxes, but the effect is only small (dotted line).

Thus, while the main effect of spray is a redistribution of the energy flux from sensible to latent, the total flux can change due to indirect effects. This is also seen in figure 6.3d, where the total heat flux is significantly larger in the spray run. At the location of figure 6.5, the change in total heat flux is negative in the first part and positive in the second part of the storm. Averaging both in space and in time, we find no change in the total flux, except for the Q_s-contribution.

The time series shown in figure 6.4 are typical for locations in the North Sea. The changes due to spray can be considerable. To check whether these effects are also present in observations, we have compared model predictions of 2-m temperature and humidity against all available observations over the sea in the area (50°N–70°N,10°W–10°E). The inclusion of spray reduces the temperature bias from 0.78 to 0.49 °C, while the bias in humidity increases from 0.27 to 0.41 g kg^{-1}, averaged over the four days of the run. This change in bias is, of course, due to the storm

period. In contrast, the standard deviation remains at the same level of 1.5 °C and 0.67 g kg^{-1}, respectively. Moreover, if we select only those observations taken at high wind speeds, then the standard deviation also remains unchanged. Thus, no improvement of the skill of the model is noticed in this sense. It is probably difficult anyway to reach an improvement of the standard deviation because of the coarse resolution of the SST field that is used in HiRLAM. The 2-m temperature and humidity are tightly coupled to the SST. Hence, they also suffer from lack of spatial variation.

Figure 6.6 shows cross sections of the difference in temperature and specific humidity between the spray and reference runs. Below 850 hPa, the atmosphere is cooled by up to 1.5 °C due to spray evaporation. At the lower levels, the air is moistened, which is consistent with the increased latent heat flux. However, around 800 hPa, drying is observed. The reason for this is that spray stabilizes the boundary layer, thus reducing its height, and the height at which the lowest clouds are formed. Hence, due to condensation, the humidity can become lower than in the reference run. At higher levels, where the clouds are also present in the reference run, the spray run is again moister. The additional water vapour, added to the atmosphere by spray evaporation, condensates, at least partly, between 750 and 500 hPa. The associated latent heat release leads to a general slight warming at these midlevels.

Such features are still visible when the air column has been advected over land. Figure 6.7 compares vertical profiles in De Bilt at the time when the largest differences between the spray and reference runs are present. In the spray run, the boundary layer is more humid as a consequence of the extra moisture fed into the air above the sea. The lower atmosphere is cooled, whereas at higher levels warming is observed, as noted above. Unfortunately, we cannot discriminate between the two runs on the basis of the observations. The discrepancy between model forecast and observations is much larger than the difference between both model runs, and the effect is too indirect to see whether the impact of taking into account spray evaporation is positive or negative.

The increased condensation at higher levels is expected to lead to enhanced rainfall. Figure 6.8a shows the total precipitation from a 24-h forecast. In the region with high wind speeds, precipitation rates are around 9 mm per day with a maximum of 14 mm. The spray run gives rise to an increase in rainfall with 1 to 2 mm over a large area, while the maximum increase is around 7 mm (figure 6.8b). Since 1 mm of water in 24 hours corresponds to a latent heat flux of around 30 W m^{-2}, these numbers indicate that the increase in precipitation is of the same order as the increase in latent heat flux from the sea (cf. figure 6.3c). Thus, for this case, most of the extra moisture added to the atmosphere returns as rain, which is expected when the stratification is unstable up to a sufficient height.
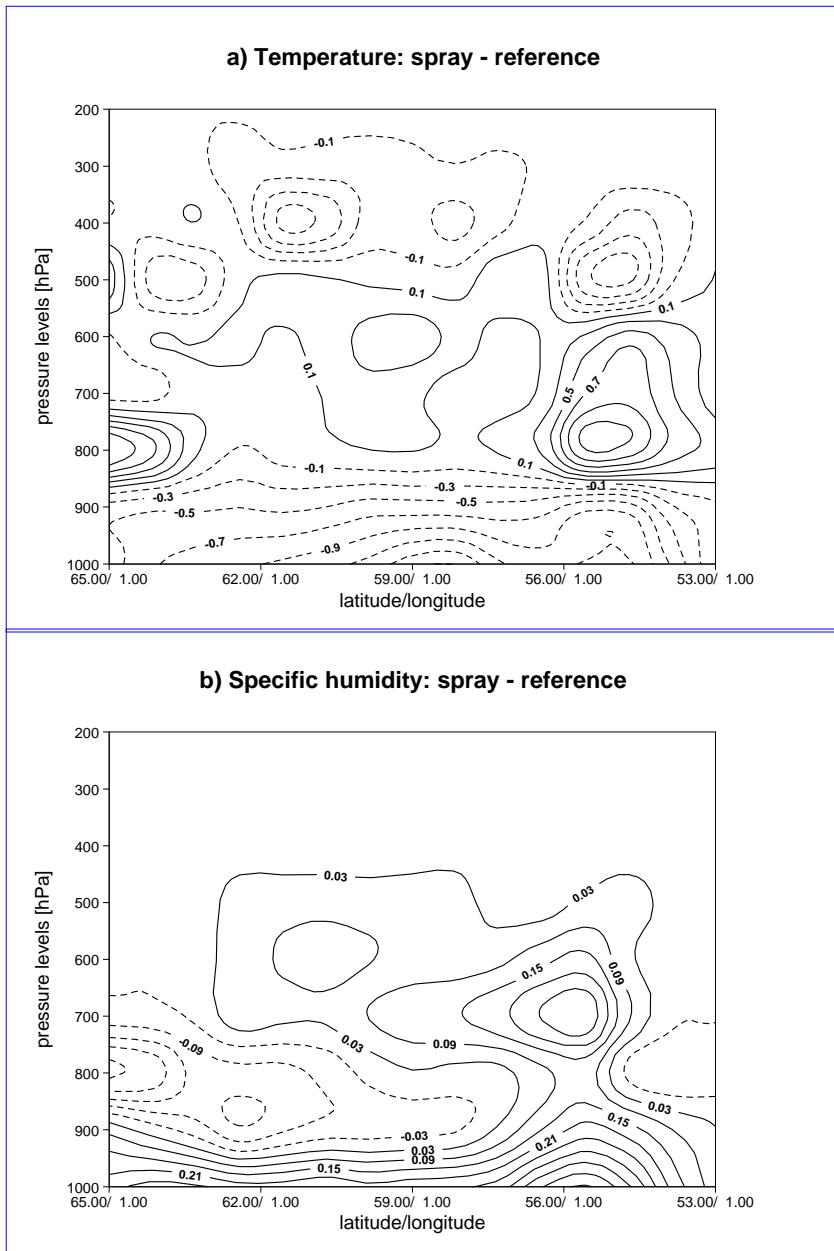
Figure 6.6: Cross sections between (65°N,1°E) and (53°N,1°E) of (a) temperature difference and (b) specific humidity difference between spray and reference runs. The model output is taken from the 12-h forecast valid at 1800 UTC 01 January 1995. Contour intervals are (a) 0.2 °C and (b) 0.06 g kg^{-1}.
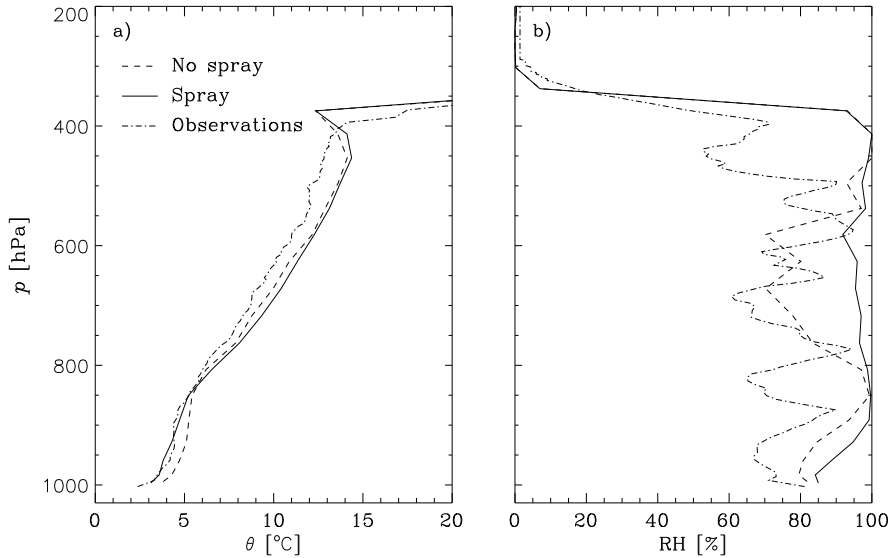
Figure 6.7: Comparison of (a) vertical potential temperature and (b) relative humidity profiles from 24-h forecast with radiosonde observations in De Bilt, The Netherlands (52.1°N,5.2°E), at 0000 UTC 02 January 1995: (solid line) spray run, (dashed line) reference run, and (dash-dotted line) observations.

6.3.2   Case 2

The second case, in January 1999, concerns a depression moving from south to east of Iceland. Figure 6.9 shows its development. According to the analyses, the minimum central pressure is reached on 1800 UTC 15 January, after a very fast deepening of 35 hPa in 18 hours. The accompanying wind speeds reach 30 m s^{-1}. The SST varies over a wide range, from near 0 °C in the north to 10 °C in the south.

Figure 6.10 shows the forecasts of wind speed and heat fluxes at the time when the depression has reached its maximum intensity. The highest latent heat fluxes are present in the southwestern part of the depicted area (figure 6.10b), since there the SST is high and the air is dry. The spray acts to increase the latent heat flux, with a maximum difference of over 200 W m^{-2} (figure 6.10c). As discussed before, the latent heat flux can locally be lower in the spray run than in the reference run, when a period with low winds follows a period with high winds. This is the case in the eye of the depression. From figure 6.10d, it again appears that the modifications of the latent and sensible heat flux do not necessarily cancel. Due to feedback effects, the
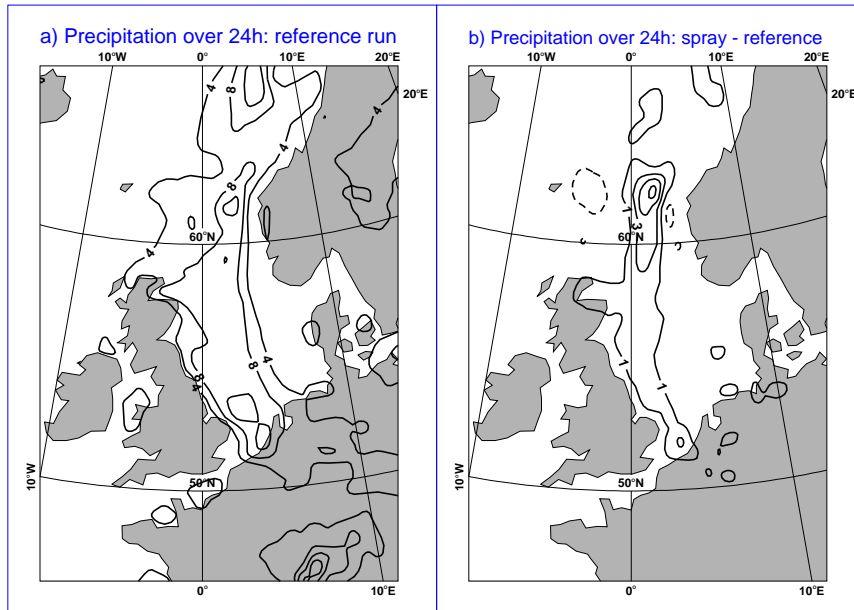
Figure 6.8: Cumulative precipitation from 24-h forecast valid at 0600 UTC 02 January 1995: (a) reference run and (b) difference between spray and reference runs. Contour intervals are (a) 4 and (b) 2 mm.

total heat flux increases in some regions, whereas it decreases in others.

Including sea spray can change the development of the depression. Figure 6.11a shows the pressure in the center of the depression as a function of time, as calculated in the reference run. The changes due to spray are presented in figure 6.11b. The analyses and 12-h forecasts both show that, during the deepening of the depression, the spray run has lower central pressures than the reference run. The effect is largest in the 12-h forecasts, where the maximum pressure difference is about 1.3 hPa. The analyses are less affected by spray, which is expected, since they tend to observations every six hours. After the minimum central pressure has been reached, the differences between spray and reference runs vanish. Similar results are obtained for longer forecast periods. We note that the location of the center of the depression is not significantly influenced by including spray.

In the forecast cycle, differences between forecasts are partly caused by differences in the analyses they start with. Thus, to make a cleaner comparison, we have
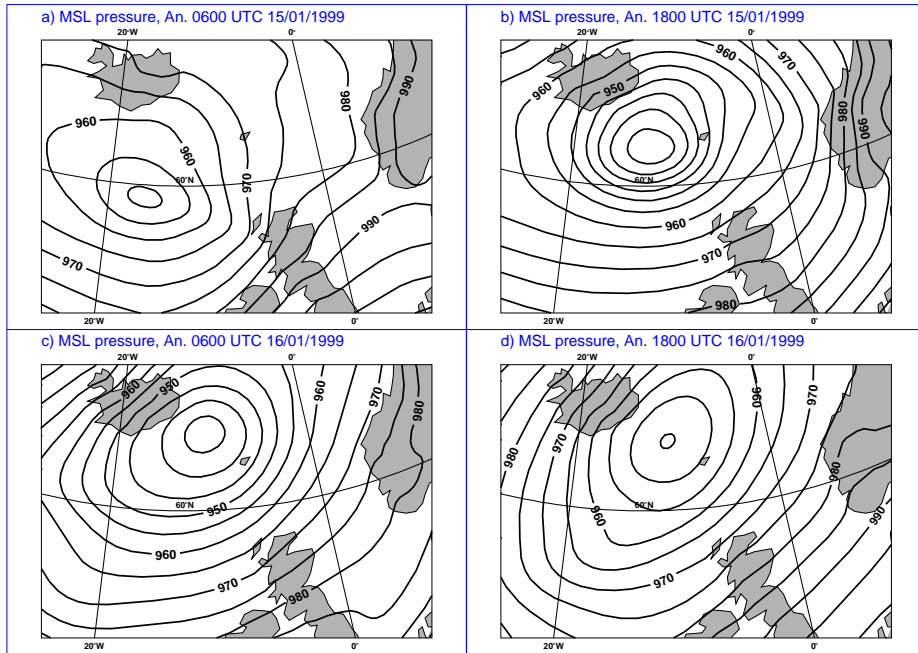
126

Figure 6.9: Mean-sea-level isobars from the HiRLAM analyses (reference version) at (a) 0600 UTC 15 January 1999, (b) 1800 UTC 15 January 1999, (c) 0600 UTC 16 January 1999, and (d) 1800 UTC 16 January 1999.

also made two separate pairs of forecasts (see figure 6.11), where the spray and reference runs begin with the same analysis. The forecasts started at 0000 UTC 15 January (s1) show the same picture of lower central pressures in the spray run. The difference is around 1 hPa when the depression has reached its minimum central pressure, remains there for about 12 hours, and then vanishes. The forecasts started at 1800 UTC (s2), which is near the time of maximum intensity, show no spray impact.

In principle, spray leads to stabilization of the boundary layer and destabilization of the surface layer, which results in lower wind speeds (see case 1). However, in this case, the deepening of the cyclone is accompanied by higher wind speeds. The maximum wind speed at the lowest model level increases by 2 %, from 36.8 m s^{-1} without spray to 37.5 m s^{-1} with spray, according to the s1 forecasts. As in case 1, precipitation rates are higher in the spray runs, which is consistent with the enhanced
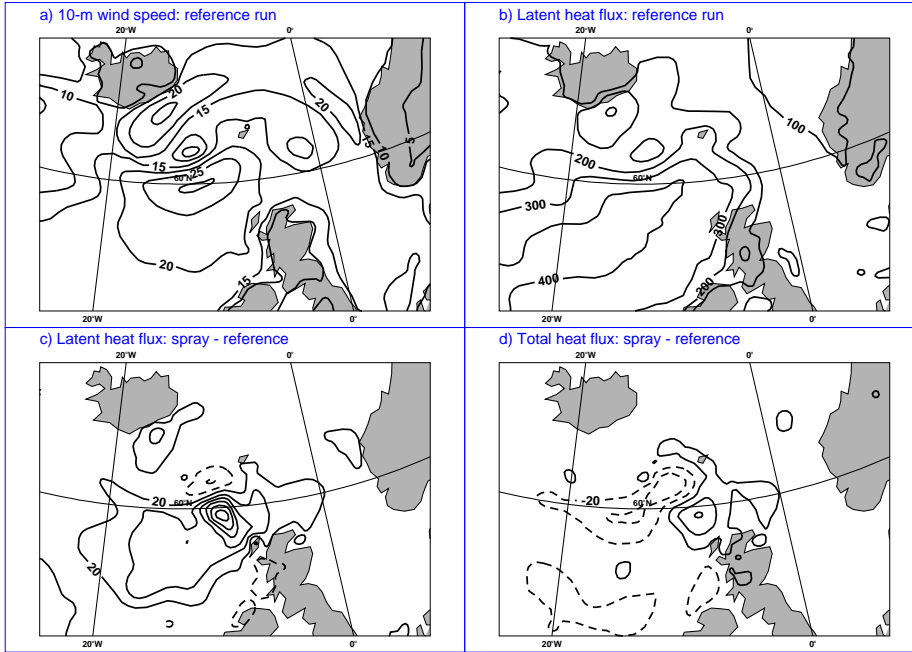
Figure 6.10: Contour plots of wind speed and heat fluxes from the 12-h forecast valid at 1800 UTC 15 January 1999: (a) 10-m wind speed from reference run, (b) surface latent heat flux from reference run, (c) latent heat flux difference (spray − reference), and (d) total (latent plus sensible) heat flux difference. Contour intervals are (a) 5 m s $^{-1}$, (b) 100 W m^{-2}, (c) 40 W m^{-2}, and (d) 40 W m^{-2}.

surface latent heat flux.

Earlier studies on the effects of sea spray evaporation have mainly focused on tropical cyclones. It is interesting to relate the present results to those studies.

Bao et al. (2000) investigated the impact of sea spray evaporation on the development of a hurricane using a coupled atmosphere–ocean–wave model. They took spray into account in a similar way as in the present study, but with an additional evaporation partitioning parameter β_e in relation (6.10):

$$H_s^s = H_s + Q_s - \beta_e Q_l. \tag{6.12}$$

They divided the spray-mediated latent heat flux into two parts: $Q_l = Q_{l1} + Q_{l2}$. For Q_{l1}, the heat required for evaporation is taken from the droplets; it corresponds to
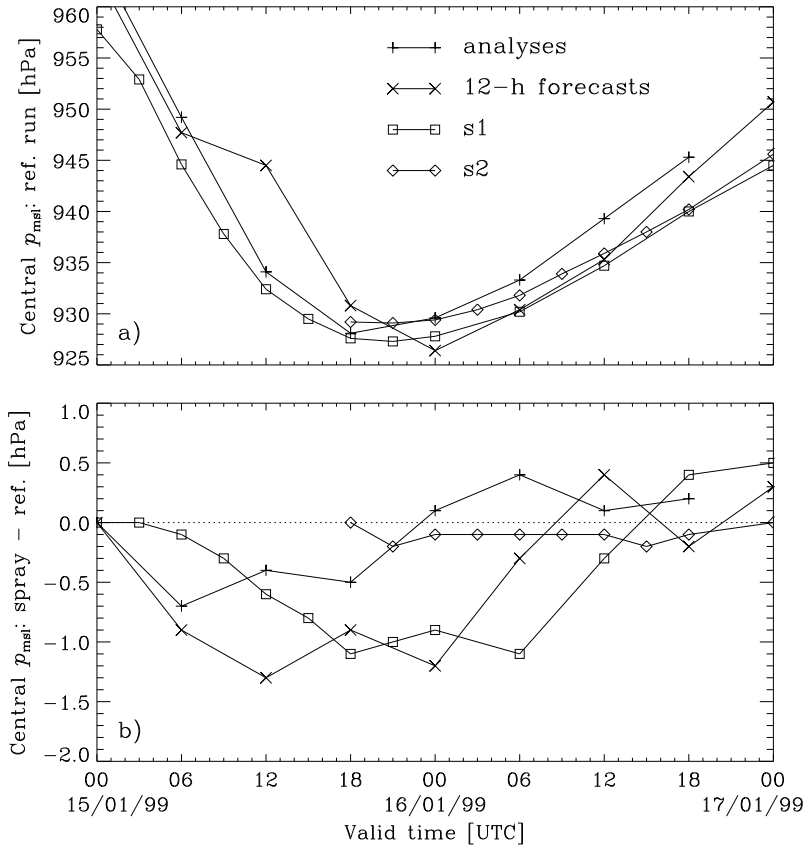
Figure 6.11: Mean-sea-level pressure in the center of the depression: (a) reference run and (b) difference between spray and reference runs. The plus and cross symbols refer to the forecast cycle, which was started on 0000 UTC 14 January 1999: pluses are analyses and crosses are 12-h forecasts. The squares and diamonds refer to the separate forecasts: squares (s1) started on 0000 UTC 15 January 1999; diamonds (s2) started on 1800 UTC 15 January 1999.

the cooling of the droplets from the air temperature to their evaporating temperature. For Q_{l2}, the necessary heat is provided by the air. The parameter β_e is then defined as $\beta_e = Q_{l2}/Q_l$. Bao et al. (2000) studied the cases of $\beta_e = 0$, 0.5, and 1. When $\beta_e = 1$, the impact of spray on the intensity of the cyclone is small, of the same order as in this study. In contrast, $\beta_e = 0$ leads to a much more intense cyclone. The reason for this is that the total heat flux increases enormously, thus fueling the cyclone. In our opinion, the parameter β_e should, however, be close to 1. With the assumption that all droplets reach the evaporating temperature T_{ev}, the part of the latent heat flux

termed Q_{l1} can be written in a similar way as equation (5.41):

$$Q_{l1} = \alpha \cdot 6.4 \times 10^{-8} U_{10}^{3.4} \Gamma \rho_a c_{pa} (T - T_{\text{ev}}).\qquad(6.13)$$

Since $T - T_{\text{ev}}$ is generally of the same order as $T_0 - T$, Q_{l1} is of the same order as Q_s and, consequently, much smaller than Q_l, implying $\beta_e \approx 1$.

Using a high-resolution tropical cyclone model, Wang et al. (1999) found that sea spray can substantially reduce the intensification rate of a cyclone in the early stage of its development, but that the final intensity is hardly affected. However, repeating their experiments with different initial conditions, Wang et al. (2001) observed no effect on the early intensification rate but found a moderate decrease of the final central pressure. They obtained an 8 % increase in maximum wind speed, which is larger than the 2 % we find. However, midlatitude and tropical cyclones have quite different spatial scales and forcing mechanisms. In particular, the latter are more sensitive to the air–sea fluxes for their dynamics.

In the present case study, including spray leads to a slight deepening of the depression. This effect seems to be systematic and was also observed in another case that is not presented here. Yet, a 2 % increase in maximum wind speed is not much. Probably, the slightly increased intensity can be explained by the generally small enhancement of the total surface heat flux due to the Q_s contribution by spray. It must, however, be noted that changes in surface pressure are rather indirect consequences, which must be viewed with caution.

6.4 Conclusions

In this study, the sensitivity of the atmosphere to sea spray evaporation is investigated using the limited-area NWP model HiRLAM. The effect of sea spray is taken into account via a modification of the surface heat fluxes, estimated with the bulk parameterization of Fairall et al. (1994). This modification mainly implies a redistribution of the energy from sensible to latent heat.

Two case studies of intense midlatitude storms are analyzed. The first case concerns a period with high wind speeds over the North Sea. The second case handles a rapidly deepening depression southeast of Iceland. In both cases, the surface heat fluxes are considerably affected by the presence of spray. The increase in latent and the decrease in sensible heat flux lead to a substantial cooling and moistening at the lowest model levels.

Indirect effects are reported as well. A large part of the additional moisture transported to the air returns as precipitation. The latent heat released with the formation of this precipitation leads to a slight warming at the higher levels. The depression in the second case study intensifies when sea spray is taken into account, but only

marginally. The reason for this is probably that spray only has a small systematic effect on the total air–sea energy flux.

It must be noted that verification of the results is difficult. The impact in the NWP model is relatively small and localized in time and space, and observations are not conclusive as to whether the impact is positive or negative. Moreover, most effects (e.g., the increase in precipitation and the slight intensification of a depression) are rather indirect. The physics modules in an NWP model have compensating errors. Thus, even if taking into account sea spray evaporation leads to better surface fluxes, then the model performance does not necessarily improve.

This study has attempted to give an indication of the typical impact of sea spray evaporation above the midlatitude oceans in numerical weather prediction. The results naturally depend on the parameterization of the contribution of spray to the surface heat fluxes. This in turn depends heavily on the amount of spray production, which is poorly known. Thus, the sensitivity of the atmospheric impact to the underlying spray production function needs further investigation. At the same time, measurements of air–sea heat fluxes and spray droplet distributions for wind speeds well above 20 m s^{-1} are needed to make more accurate estimates of the importance of spray evaporation.

Chapter 7

Summary and outlook

The main aim of this thesis is to investigate the role of wind waves and sea spray in the air–sea exchange of momentum and heat. This helps to improve parameterizations for the air–sea fluxes, which are important for use in weather and climate models. In this chapter, the main results of the present work are summarized and future perspectives are mentioned.

In chapter 2, the turbulent air flow over water waves is considered. In studies of this flow it is usually assumed that the effect of viscosity near the water surface is negligible, i.e. the Reynolds number, $Re = u_*\lambda/\nu$, is considered to be high. However, for the short waves in the spectrum this assumption is not valid, and these waves are particularly important for remote sensing applications. Therefore, a second-order turbulence closure that takes into account viscous effects is implemented and used to simulate the air flow. The numerical model shows reasonable agreement with laboratory measurements of wave-induced velocity profiles. The dependence of the dimensionless energy flux from wind to waves, or growth rate, on Re is also investigated. The growth rate of waves that are slow compared to the wind is found to increase strongly when Re decreases below 10^4, with a maximum around $Re = 800$. The numerical model predictions are in good agreement with analytical theories, direct numerical simulations, and laboratory observations. The modelling work suggests that low-Re effects at least partly explain the hitherto reported discrepancy between measured and model-predicted growth rates.

Regarding the many studies performed on the (uncoupled) flow over waves, it appears that this problem is now fairly well understood. Future work should therefore be directed towards the investigation of the coupled system of the wave spectrum, with all its length scales, and the air flow above. This can elucidate the various factors playing a role in the transfer of momentum across the air–sea interface and their interactions. As an example, Kudryavtsev and Makin (2002) showed that the air flow

over long surface waves influences the distribution of short waves along its surface, leading to a similar enhancement of the growth rate for the long wave as reported above. Further investigations should also recognize that air-flow separation associated with breaking waves is an important issue, and thus deal with more complicated flow geometries.

Numerical models as described above are computationally expensive. For applied studies it is often necessary to make quick calculations. Therefore, a semi-analytical model of the air flow over surface water waves is developed in chapter 3. The model is based on the subdivision of the air flow into inner and outer regions, as introduced by Belcher and Hunt (1993). It describes phenomenologically the basic feature of the wave boundary layer: the rapid distortion of turbulence in the outer region. Calculated wave-induced velocity and shear-stress profiles, as well as growth rates, show good agreement with the high-*Re* version of the numerical model used in chapter 2. Moreover, the predicted velocity profiles compare favourably with laboratory measurements.

The model allows to investigate the effect of the angle θ between mean wind and wave directions on the wave-induced air flow. Simulations show that the influence of the wind speed component transverse to the wave direction on the air flow, and hence on the growth rate of the waves, is small. This is confirmed by calculations with the numerical model. The growth rate of slowly moving waves (as compared to the wind speed) is then proportional to $\cos^2 \theta$, whereas, for faster waves, it has a narrower angular distribution.

Various processes occurring just above the sea surface can be studied using the semi-analytical model. An example is the transport of spray droplets in the marine surface layer. This is illustrated in chapter 4 by a short study on the impact of the wave-induced air flow on the vertical spray profiles in the SeaCluse (Mestayer et al. 1996) spray model. Using the present description of the air flow yields quite different spray distributions compared with the original description in SeaCluse, in particular for the smaller droplets. One of the handicaps of the approach is the combined Eulerian–Lagrangian character of SeaCluse. Therefore, it would be interesting to repeat the work by using a completely Lagrangian model of droplet transport above the waves. Secondly, the inclusion of spume droplets is important. A problem will be the lack of observational data on such spume droplets. Hence, it is not clear how to specify their initial conditions. Measurements in this direction appear to be necessary.

Chapter 4 also contains a review of research on sea spray. The review concerns both experimental and modelling work with a focus on those aspects that are relevant for estimating the effects of spray on the heat balance above the sea. It is argued that the main need is for more accurate predictions of the spray source function,

i.e. the, radius-dependent, amount of sea spray droplets produced from the water surface under given conditions. One way to proceed in estimating the source function is by combining (laboratory) observations of jet- and spume-droplet production with knowledge on wave breaking statistics. Another way consists of measuring spray droplet concentrations at some height above the surface and using models in order to infer the production rates leading to these concentrations. While the first option is hampered by scaling problems, both options are hindered by experimental difficulties measuring large droplets.

Considering these problems, it seems worthwhile trying to infer the presence of spray from its effect on the heat and moisture fluxes. A difficulty then is to separate direct and spray-mediated contributions. To this end, measurements of temperature, humidity, and heat-flux profiles should be performed. According to earlier studies (e.g., Kepert et al. 1999) as well as the present work (chapter 5), a vertical variation of the fluxes in the lower tens of meters above the surface due to evaporating spray should be present at high wind speeds. In combination with numerical models, such measurements have the potential for more accurate estimates of both the height scales at which spray droplets are thermodynamically active and the amount of spray droplets that are generated.

In chapter 5 a simplified model for evaporating sea spray in the marine surface layer is presented. The model, an extension of Makin's (1998) work, has specifically been designed in order to make quick estimates of the effective contribution of sea spray to the air–sea heat fluxes. To reach short calculation times, equilibrium vertical spray distributions based on empirical knowledge are assumed. On the other hand, two-way interactions between the evaporation of spray and the atmospheric temperature and humidity profiles are taken into account. First, the predicted spray-mediated heat fluxes are compared with existing estimates (Fairall et al. 1994; Andreas 1998), all neglecting atmospheric feedbacks, and the differences are explained. Subsequently, the influence of atmospheric feedbacks on the spray heat fluxes is assessed. This feedback efficiency is estimated to be fairly constant and not very large for a wide range of conditions. However, this is based on what at present appears to be the best guess for the source function (Andreas 1998). For higher production rates, the predicted feedback is rapidly enhanced. Note that the above does not imply that spray evaporation itself is unimportant. In fact, the contribution to the heat fluxes becomes significant from wind speeds of around 20 m s^{-1} on. Future work on the model should include a more detailed tuning and comparison with numerical models taking spray droplets of all sizes explicitly into account.

The spray model can be viewed as a comprehensive parameterization of the air–sea heat (and momentum) fluxes. It can be applied in a numerical weather prediction (NWP) model, providing boundary conditions above water surfaces. It thus allows

to investigate the impact of evaporating sea spray on weather forecasts, which is the final goal of this thesis. Chapter 6 contains two case studies of intense midlatitude storms performed with the NWP model HiRLAM, which is used for the operational weather forecasts at KNMI. These studies have not been carried out with the simplified model from chapter 5 but with the parameterization by Fairall et al. (1994) because the latter is even much more computationally inexpensive, and the differences are within the uncertainty of the source function.

A general consequence of evaporating spray is a significantly cooler and moister surface layer. This leads to stabilization of the boundary layer. Indirect effects are enhanced precipitation and associated mid-level latent heat release. The second of the case studies, which deals with a rapidly deepening depression, indicates that including spray causes a marginal intensification of the depression. The case studies give an indication of spray effects using a parameterization based on a particular source function and a simple description of atmospheric feedback. The sensitivity to these underlying assumptions was further tested by Van Zetten (2001), who, using a column version of HiRLAM, illustrated that spray impacts can vary significantly depending on the assumptions.

At present, indirect verification of parameterizations of the contribution of spray to the heat fluxes is difficult because of lack of measurements, representativeness errors, and compensating errors in the NWP model. Nevertheless, it seems to be possible to demonstrate signatures of spray evaporation in the future. To this end, higher-resolution models should be run for storm cases, carefully selected such that many measurements are available (e.g., during field campaigns).

Considering that spray effects in the mid-latitudes are relatively small, and only present in extreme events, it appears that such effects may, for the time being, safely be neglected in weather prediction. As soon as NWP models have evolved to a level that extreme events can be forecasted with good skill, the time has come to revisit sea spray.

Appendix A

Second-order turbulence closure schemes

A.1 The LRR model

In the LRR model, the terms in the right-hand sides of (2.14) and (2.15) are closed as follows. The production term needs no parameterization

$$P_{ij} = -\left(\overline{u_i' u_k'} \frac{\partial \bar{u}_j}{\partial x_k} + \overline{u_j' u_k'} \frac{\partial \bar{u}_i}{\partial x_k} \right). \tag{A.1}$$

The diffusion term reads

$$d_{ij} = -\frac{\partial \overline{u_i' u_j' u_k'}}{\partial x_k}, \tag{A.2}$$

where the triple correlation is modelled as

$$\overline{u_i' u_j' u_k'} = -c_s \frac{e}{\varepsilon} \left(\overline{u_i' u_l'} \frac{\partial \overline{u_j' u_k'}}{\partial x_l} + \overline{u_j' u_l'} \frac{\partial \overline{u_k' u_i'}}{\partial x_l} + \overline{u_k' u_l'} \frac{\partial \overline{u_i' u_j'}}{\partial x_l} \right). \tag{A.3}$$

The pressure–strain correlation,

$$\phi_{ij} = \overline{\frac{p'}{\rho} \left(\frac{\partial u_i'}{\partial x_j} + \frac{\partial u_j'}{\partial x_i} \right)}, \tag{A.4}$$

is modelled in two parts. For the first part, the Rotta hypothesis is used

$$\phi_{ij}^{(1)} = -c_1 \varepsilon a_{ij}, \tag{A.5}$$

where a_{ij} is the dimensionless stress anisotropy

$$a_{ij} = \frac{\overline{u_i' u_j'}}{e} - \frac{2}{3}\delta_{ij}. \tag{A.6}$$

The second part of ϕ_{ij} is called the rapid term. It is parameterized as

$$\begin{aligned} \phi_{ij}^{(2)} &= -\frac{c_2+8}{11}\left(P_{ij} - \frac{1}{3}P_{kk}\delta_{ij}\right) - \frac{30c_2-2}{55}e\left(\frac{\partial \bar{u}_i}{\partial x_j} + \frac{\partial \bar{u}_j}{\partial x_i}\right) \\ &\quad - \frac{8c_2-2}{11}\left(D_{ij} - \frac{1}{3}P_{kk}\delta_{ij}\right), \end{aligned} \tag{A.7}$$

where

$$D_{ij} = -\left(\overline{u_i' u_k'}\frac{\partial \bar{u}_k}{\partial x_j} + \overline{u_j' u_k'}\frac{\partial \bar{u}_k}{\partial x_i}\right). \tag{A.8}$$

For completeness, we note that another pressure correlation term is present in (2.14): the pressure-diffusion term. It is not explicitly modelled but assumed to be incorporated in d_{ij}. The dissipation, finally, is assumed to be isotropic:

$$\varepsilon_{ij} = \frac{2}{3}\delta_{ij}\varepsilon. \tag{A.9}$$

In equation (2.15), the diffusion term is closed through

$$\overline{\varepsilon' u_i'} = -c_\varepsilon \frac{e}{\varepsilon}\overline{u_i' u_k'}\frac{\partial \varepsilon}{\partial x_k}. \tag{A.10}$$

For the constants appearing in the LRR model, we use the same values as Mastenbroek et al. (1996): $c_s = 0.11$, $c_1 = 1.5$, $c_2 = 0.4$, $c_{\varepsilon 1} = 1.44$, $c_{\varepsilon 2} = 1.92$, and $c_\varepsilon = 0.267$.

A.2   The low-Reynolds-number model

The formulation of the second-order turbulence closure for low Reynolds numbers follows Craft and Launder (1996). Modifications include the neglect of terms that are not important for the flow we consider. A special feature of the closure is that no wall-normal vectors are used. To still be able to identify near-surface effects, the flatness parameter A is introduced. It is defined as

$$A = 1 - \frac{9}{8}(A_2 - A_3), \tag{A.11}$$

where $A_2 = a_{ij}a_{ij}$ and $A_3 = a_{ij}a_{jk}a_{ki}$ are the second and third invariants of the dimensionless stress anisotropy, a_{ij}, which was introduced in equation (A.6). $A = 1$ in isotropic turbulence and vanishes near a surface, where the turbulent fluctuations reduce to a two-component form.

The closure of the terms in the Reynolds-stress equations is as follows. The production term is as in (A.1). In the diffusion term, equation (A.2), an additional viscous contribution appears

$$d_{ij} = \frac{\partial}{\partial x_k}\left(\nu\frac{\partial \overline{u_i'u_j'}}{\partial x_k} - \overline{u_i'u_j'u_k'}\right).$$
(A.12)

The pressure–strain correlation is modelled as in Craft, Ince, and Launder (1996):

$$\phi_{ij}^{(1)} = -c_1\varepsilon^*\left[a_{ij} + c_1'\left(a_{ik}a_{kj} - \frac{1}{3}A_2\delta_{ij}\right)\right] - \varepsilon^*Aa_{ij},$$
(A.13)

$$\phi_{ij}^{(2)} = -0.6\left(P_{ij} - \frac{1}{3}P_{kk}\delta_{ij}\right) + 0.3a_{ij}P_{kk}$$

$$- \frac{0.2}{e}\left[\overline{u_k'u_j'}\,\overline{u_l'u_i'}\left(\frac{\partial \overline{u_l}}{\partial x_l} + \frac{\partial \overline{u_l}}{\partial x_k}\right) - \overline{u_l'u_k'}\left(\overline{u_i'u_k'}\frac{\partial \overline{u_j}}{\partial x_l} + \overline{u_j'u_k'}\frac{\partial \overline{u_i}}{\partial x_l}\right)\right]$$
(A.14)

$$- c_2[A_2(P_{ij} - D_{ij}) + 3a_{mi}a_{nj}(P_{mn} - D_{mn})],$$

where ε^* is the homogeneous dissipation rate, which is related to the kinematic dissipation rate ε by

$$\varepsilon^* = \varepsilon - 2\nu\left(\frac{\partial e^{1/2}}{\partial x_j}\right)^2.$$
(A.15)

The stress dissipation, finally, is taken to be:

$$\varepsilon_{ij} = f_\varepsilon 2\varepsilon\frac{\varepsilon_{ij}'}{\varepsilon_{kk}'} + (1 - f_\varepsilon)\frac{2}{3}\varepsilon\delta_{ij},$$
(A.16)

where

$$\varepsilon_{ij}' = \varepsilon\frac{\overline{u_i'u_j'}}{e} + 2\nu\left(\frac{\overline{u_l'u_n'}}{e}\frac{\partial e^{1/2}}{\partial x_l}\frac{\partial e^{1/2}}{\partial x_n}\delta_{ij} + \frac{\overline{u_l'u_i'}}{e}\frac{\partial e^{1/2}}{\partial x_j}\frac{\partial e^{1/2}}{\partial x_l} + \frac{\overline{u_l'u_j'}}{e}\frac{\partial e^{1/2}}{\partial x_i}\frac{\partial e^{1/2}}{\partial x_l}\right).$$
(A.17)

The coefficient f_ε manages the transition from isotropic dissipation in the fully turbulent part of the flow to anisotropic dissipation towards the surface. Following Launder and Li (1994) we take

$$f_\varepsilon = \exp(-20A^2).$$
(A.18)

139

Instead of (2.15), a similar equation is now solved for the homogeneous dissipation rate:

$$\frac{\partial \varepsilon^*}{\partial t} + \bar{u}_i \frac{\partial \varepsilon^*}{\partial x_i} = \frac{\partial}{\partial x_i}\left[\left(\nu \delta_{ik} + c_\varepsilon \overline{u_i' u_k'} \frac{e}{\varepsilon}\right)\frac{\partial \varepsilon^*}{\partial x_k}\right] + \frac{\varepsilon^*}{e}\left(c_{\varepsilon 1}\frac{P_{ii}}{2} - c_{\varepsilon 2}\varepsilon^* - c_{\varepsilon 2}'(\varepsilon - \varepsilon^*)\right)$$

$$+ c_{\varepsilon 3}\nu\overline{u_i' u_j'}\frac{e}{\varepsilon}\frac{\partial^2 \bar{u}_l}{\partial x_i \partial x_l}\frac{\partial^2 \bar{u}_l}{\partial x_j \partial x_l}. \tag{A.19}$$

The coefficients in the low-*Re* model are

$$c_s = 0.11, \qquad c_1 = (3.75 A_2^{1/2} + 1)A, \qquad c_1' = 0.7, \qquad c_2 = 0.6,$$

$$c_{\varepsilon 1} = 1.0, \qquad c_{\varepsilon 2}' = 1.0, \qquad c_{\varepsilon 3} = 1.75, \qquad c_\varepsilon = 0.18,$$

$$c_{\varepsilon 2} = \frac{1.92}{1 + 0.7 A_d A_2^{1/2}}, \qquad A_d = \max(0.2, A).$$

The constant $c_{\varepsilon 3}$ was used to tune the model such that it reproduces the law of the wall for a flat plate boundary layer. Its value is somewhat higher than mentioned in Craft and Launder (1996), which can be explained by the omission of their $c_{\varepsilon 4}$ term.

Appendix B

The wave-induced surface stress

The wave-induced stress (or momentum flux) at the surface τ_w^0 can be related to the growth rate γ. Consider first a monochromatic gravity-capillary wave with an elevation as given by (2.1). The mean energy per unit area, E, of such a wave is (e.g., Phillips 1977)

$$E = \tfrac{1}{2}\rho_w k^{-1}\omega^2 a^2,$$ (B.1)

while the mean momentum, M, is

$$M = E/c = \tfrac{1}{2}\rho_w \omega a^2.$$ (B.2)

The wave stress at the surface, τ_w^0, is given by

$$\tau_w^0 = \dot{M} = \gamma\omega E/c.$$ (B.3)

One usually assumes that the surface elevation in a wave field can be described as a superposition of many waves with random phase ϕ_n:

$$\eta(\mathbf{x},t) = \sum_n a_n \cos\left(\mathbf{k}_n \cdot \mathbf{x} - \omega_n t + \phi_n\right).$$ (B.4)

Under certain assumptions the elevation is then described statistically by a Gaussian distribution. The wavenumber spectrum $F(\mathbf{k})$ is defined as the Fourier transform of the autocovariance of this distribution

$$F(\mathbf{k};\mathbf{x},t) = (2\pi)^{-2} \int \langle \eta(\mathbf{x},t)\eta(\mathbf{x}+\boldsymbol{\xi},t) \rangle e^{-i\mathbf{k}\cdot\boldsymbol{\xi}} d\boldsymbol{\xi},$$ (B.5)

with inverse transform

$$\langle \eta(\mathbf{x},t)\eta(\mathbf{x}+\boldsymbol{\xi},t) \rangle = \int F(\mathbf{k};\mathbf{x},t) e^{i\mathbf{k}\cdot\boldsymbol{\xi}} d\mathbf{k}.$$ (B.6)

141

The wave-induced surface stress

The dependence of F on $\mathbf{x}$ and t is often omitted, as in most circumstances the spectrum varies on much larger scales than the wavelength of the longest waves. With $\boldsymbol{\xi} = 0$, (B.6) gives the mean square elevation

$$\langle \eta^2 \rangle = \int F(\mathbf{k}) \mathrm{d}\mathbf{k} = \int_0^\infty \int_0^{2\pi} F(k,\theta) k \mathrm{d}\theta \mathrm{d}k, \tag{B.7}$$

where, in the second equality, F is presented as a directional spectrum. The total energy density becomes

$$E = \rho_w \int \omega^2 k^{-1} F(\mathbf{k}) \mathrm{d}\mathbf{k}. \tag{B.8}$$

The mean momentum is

$$\mathbf{M} = \rho_w \int \omega \mathbf{k} k^{-1} F(\mathbf{k}) \mathrm{d}\mathbf{k}. \tag{B.9}$$

Next, it is assumed that the change of the spectrum due to the wind can be described by all wave components having their own growth rate, that is

$$\dot{F}(\mathbf{k}) = \omega \gamma F(\mathbf{k}). \tag{B.10}$$

Let the wind direction be given by $\theta = 0°$, then the wave-induced surface stress in wind direction can finally be written in terms of the directional spectrum as

$$\tau_w^0 = \rho_w \int_0^\infty \int_0^{2\pi} \omega^2 \gamma(k,\theta) F(k,\theta) \cos\theta k \mathrm{d}\theta \mathrm{d}k. \tag{B.11}$$

References

Andreas, E. L., 1989: Thermal and size evolution of sea spray droplets. CRELL Rep. 89–11, U. S. Army Cold Reg. Res. and Eng. Lab., Hanover, N. H.

Andreas, E. L., 1990: Time constants for the evolution of sea spray droplets. *Tellus*, **42B,** 481–497.

Andreas, E. L., 1992: Sea spray and the turbulent air–sea heat fluxes. *J. Geophys. Res.*, **97,** 11429–11441.

Andreas, E. L., 1995: The temperature of evaporating sea spray droplets. *J. Atmos. Sci.*, **52,** 852–862.

Andreas, E. L., 1998: A new sea spray generation function for wind speeds up to 32 m s^{-1}. *J. Phys. Oceanogr.*, **28,** 2175–2184.

Andreas, E. L. and J. DeCosmo, 1999: Sea spray production and influence on air–sea heat and moisture fluxes over the open ocean. In Geernaert, G. L., editor, *Air–sea exchange: physics, chemistry and dynamics*, pages 327–362. Kluwer Academic Publishers, Dordrecht.

Andreas, E. L., J. B. Edson, E. C. Monahan, M. P. Rouault, and S. D. Smith, 1995: The spray contribution to net evaporation from the sea: a review of recent progress. *Boundary-Layer Meteorol.*, **72,** 3–52.

Andreas, E. L. and K. A. Emanuel, 2001: Effects of sea spray on tropical cyclone intensity. *J. Atmos. Sci.*, **58(24),** 3741–3751.

Baldwin, B. and H. Lomax, 1978: Thin layer approximation and algebraic model for seperated turbulent flow. *AIAA paper*, pages 78–257.

Banner, M. L., 1990: The influence of wave breaking on the surface pressure distribution in wind–wave interaction. *J. Fluid Mech.*, **211,** 463–495.

References

Bao, J.-W., J. M. Wilczak, J.-K. Choi, and L. H. Kantha, 2000: Numerical simulations of air–sea interaction under high wind conditions using a coupled model: a study of hurricane development. *Mon. Wea. Rev.*, **128,** 2190–2210.

Belcher, S. E. and J. C. R. Hunt, 1993: Turbulent shear flow over slowly moving waves. *J. Fluid Mech.*, **251,** 109–148.

Belcher, S. E. and J. C. R. Hunt, 1998: Turbulent flow over hills and waves. *Ann. Rev. Fluid Mech.*, **30,** 507–538.

Beljaars, A. C. M., 1995: The parameterization of surface fluxes in large scale models under free convection. *Quart. J. Roy. Meteor. Soc.*, **121,** 255–270.

Bintanja, R., 2000: Snowdrift suspension and atmospheric turbulence. Part I: Theoretical background and model description. *Boundary-Layer Meteorol.*, **95(3),** 343–368.

Blanchard, D. C., 1963: The electrification of the atmosphere by particles from bubbles in the sea. In Sears, M., editor, *Progress in oceanography*, volume 1, pages 71–202. MacMillan, New York.

Blanchard, D. C., 1969: The oceanic production rate of cloud nuclei. *J. Rech. Atmos.*, **4,** 1–6.

Blanchard, D. C., 1983: The production, distribution, and bacterial enrichment of the sea-salt aerosol. In Liss, P. S. and W. G. N. Slinn, editors, *Air–sea exchange of gases and particles*, pages 407–454. D. Reidel, Dordrecht.

Blanchard, D. C., 1989: The size and height to which jet droplets are ejected from bursting bubbles in seawater. *J. Geophys. Res.*, **94,** 10999–11002.

Blanchard, D. C. and A. H. Woodcock, 1957: Bubble formation and modification in the sea and its meteorological significance. *Tellus*, **9,** 145–158.

Blanchard, D. C. and A. H. Woodcock, 1980: The production, concentration and vertical distribution of the sea-salt aerosol. *Ann. N. Y. Acad. Sci.*, **338,** 330–347.

Burgers, G. and V. K. Makin, 1993: Boundary layer model results for wind-sea growth. *J. Phys. Oceanogr.*, **23,** 372–385.

Carruthers, D. J. and T. C. Choularton, 1986: The microstructure of hill cap clouds. *Quart. J. Roy. Meteor. Soc.*, **112,** 113–129.

Chaen, M., 1973: Studies on the production of sea-salt particles on the sea surface. *Mem. Fac. Fish., Kagoshima Univ.*, **22,** 49–107.

Chalikov, D. V., 1978: The numerical simulation of wind–wave interaction. *J. Fluid Mech.*, **87(3),** 561–582.

Charnock, H., 1955: Wind stress on a water surface. *Quart. J. Roy. Meteor. Soc.*, **81,** 639–640.

Cohen, J. E., 1997: *Theory of turbulent wind over fast and slow waves*. PhD thesis, University of Cambridge.

Cohen, J. E. and S. E. Belcher, 1999: Turbulent shear flow over fast-moving waves. *J. Fluid Mech.*, **386,** 345–371.

Craft, T. J., N. Z. Ince, and B. E. Launder, 1996: Recent developments in second-moment closure for buoyancy-affected flows. *Dyn. Atmos. Oceans*, **23,** 99–114.

Craft, T. J. and B. E. Launder, 1996: A Reynolds stress closure designed for complex geometries. *Intl J. Heat and Fluid Flow*, **17,** 245–254.

De Leeuw, G., 1986: Vertical profiles of giant particles close above the sea surface. *Tellus*, **38B,** 51–61.

De Leeuw, G., 1987: Near-surface particle size distribution profiles over the North Sea. *J. Geophys. Res.*, **92,** 14631–14635.

DeCosmo, J., K. B. Katsaros, S. D. Smith, R. J. Anderson, W. A. Oost, K. Bumke, and H. Chadwick, 1996: Air–sea exchange of water vapor and sensible heat: The Humidity EXchange Over the Sea (HEXOS) results. *J. Geophys. Res.*, **101,** 12001–12016.

Donelan, M. A. and W. J. Pierson, 1987: Radar scatter and equilibrium ranges in wind-generated waves with applications to scatterometry. *J. Geophys. Res.*, **92,** 4971–5029.

Edson, J. B., S. Anquetin, P. G. Mestayer, and J.F. Sini, 1996: Spray droplet modeling 2: An interactive Eulerian–Lagrangian model of evaporating spray droplets. *J. Geophys. Res.*, **101,** 1279–1299.

Edson, J. B. and C. W. Fairall, 1994: Spray droplet modeling 1: Lagrangian model simulation of the turbulent transport of evaporating droplets. *J. Geophys. Res.*, **99,** 25295–25311.

Elfouhaily, T., B. Chapron, K. B. Katsaros, and D. Vandemark, 1997: A unified directional spectrum for long and short wind-driven waves. *J. Geophys. Res.*, **102,** 15781–15796.

References

Eymard, L., G. Caniaux, H. Dupuis, L. Prieur, H. Giordani, R. Troadec, P. Besse-moulin, G. Lachaud, G. Bouhours, D. Bourras, C. Guérin, P. Le Borgne, A. Brisson, and A. Marsouin, 1999: Surface fluxes in the North Atlantic current during the CATCH/FASTEX experiment. *Quart. J. Roy. Meteor. Soc.*, **125,** 3563–3600.

Fairall, C. W., E. F. Bradley, D. P. Rogers, J. B. Edson, and G. S. Young, 1996: Bulk parameterization of air–sea fluxes for Tropical Ocean Global Atmosphere Coupled-Ocean Atmosphere Response Experiment. *J. Geophys. Res.*, **101,** 3747–3764.

Fairall, C. W., J. B. Edson, and M. A. Miller, 1990: Heat fluxes, whitecaps, and sea spray. In Geernaert, G. L. and W. J. Plant, editors, *Surface waves and fluxes*, volume 1, pages 173–208. Kluwer Acad., Norwell, Mass.

Fairall, C. W., J. D. Kepert, and G. J. Holland, 1994: The effect of sea spray on surface energy transports over the ocean. *Global Atmos. Ocean Syst.*, **2,** 121–142.

Fitzgerald, J. W., W. A. Hoppel, and F. Gelbard, 1998: A one-dimensional sectional model to simulate multicomponent aerosol dynamics in the marine boundary layer, 1, Model description. *J. Geophys. Res.*, **103,** 16085–16102.

Galperin, B., L. H. Kantha, S. Hassid, and A. Rosati, 1988: A quasi-equilibrium turbulent energy model for geophysical flows. *J. Atmos. Sci.*, **45,** 55–62.

Garratt, J. C., 1992: *The atmospheric boundary layer*. Cambridge University Press.

Gathman, S. G. and A. M. J. Van Eijk, 1998: Electro optical propagation just above wave tops as predicted by ANAM, the advanced Navy aerosol model. In *AGARD Sensor Propagation panel specialist's meeting on EO propagation, Signature and System Performance under adverse meteorological conditions, considering out-of-area operations*, RTO-MP-1, pages 14–1 to 14–9. 16–19 March 1998, Naples, Italy.

Geernaert, G. L., 1999: Historical perspective. In Geernaert, G. L., editor, *Air–sea exchange: physics, chemistry and dynamics*, pages 1–24. Kluwer Academic Publishers, Dordrecht.

Gent, P. R. and P. A. Taylor, 1976: A numerical model of the air flow above water waves. *J. Fluid Mech.*, **77,** 105–128.

Gong, W., P. A. Taylor, and A. Dörnbrack, 1996: Turbulent boundary-layer flow over fixed aerodynamically rough two-dimensional sinusoidal waves. *J. Fluid Mech.*, **312,** 1–37.

Harris, J. A., S. E. Belcher, and R. L. Street, 1996: Linear dynamics of wind-waves in coupled turbulent air–water flow. Part 2. Numerical model. *J. Fluid Mech.*, **308,** 219–254.

Henn, D. S. and R. I. Sykes, 1999: Large-eddy simulation of flow over wavy surfaces. *J. Fluid Mech.*, **383,** 75–112.

Holtslag, A. A. and B. A. Boville, 1993: Local versus nonlocal boundary-layer diffusion in a global climate model. *J. Climate*, **10,** 1825–1842.

Hsu, C.-T. and E. Y. Hsu, 1983: On the structure of turbulent flow over a progressive water wave: theory and experiment in a transformed, wave-following coordinate system. Part 2. *J. Fluid Mech.*, **131,** 123–153.

Hunt, J. C. R., S. Leibovich, and K. J. Richards, 1988: Turbulent shear flow over low hills. *Quart. J. Roy. Meteor. Soc.*, **114,** 1435–1471.

Jacobs, S. J., 1987: An asymptotic theory for the turbulent flow over a progressive water wave. *J. Fluid Mech.*, **174,** 69–80.

Jeffreys, H., 1925: On the formation of water waves by wind. *Proc. R. Soc. Lond.*, **A 107,** 189–206.

Källén, E., 1996: *Hirlam documentation manual. System 2.5*. SMHI, SE–601 76 Norrköping, Sweden.

Kepert, J. D., C. W. Fairall, and J.-W. Bao, 1999: Modelling the interaction between the atmospheric boundary layer and evaporating sea spray droplets. In Geernaert, G. L., editor, *Air–sea exchange: physics, chemistry and dynamics*, pages 363–409. Kluwer Academic Publishers, Dordrecht.

Komen, G. J., L. Cavaleri, M. Donelan, K. Hasselmann, S. Hasselmann, and P. A. E. M. Janssen, 1994: *Dynamics and modelling of ocean waves*. Cambridge University Press.

Komen, G. J., V. N. Kudryavtsev, V. K. Makin, J. F. Meirink, and W. A. Oost, 1999: Can one discriminate between different wave generation theories on the basis of wind profile measurements? In Banner, M. L., editor, *The wind-driven air–sea interface*, pages 199–206. Sydney.

Korolev, V. S., S. A. Petrichenko, and V. D. Pudov, 1990: Heat and moisture exchange between the ocean and atmosphere in tropical storms Tess and Skip. *Meteorologiya i Gidrologiya*, **2,** 108–111.

References

Kudryavtsev, V. N. and V. K. Makin, 2001: The impact of air-flow separation on the drag of the sea surface. *Boundary-Layer Meteorol.*, **98,** 155–171.

Kudryavtsev, V. N. and V. K. Makin, 2002: Coupled dynamics of short wind waves and the air flow over long surface waves. Preprint 2001-23, KNMI, De Bilt, The Netherlands. (Submitted to *J. Geophys. Res.*).

Kudryavtsev, V. N., V. K. Makin, and J. F. Meirink, 1999: Turbulent air flow over sea waves: simplified model for applications. Scientific Report 99–02, KNMI, De Bilt, The Netherlands.

Kudryavtsev, V. N., V. K. Makin, and J. F. Meirink, 2001: Simplified model of the air flow above waves. *Boundary-Layer Meteorol.*, **100,** 63–90.

Kudryavtsev, V. N., C. Mastenbroek, and V.K. Makin, 1997: Modulation of wind ripples by long surface waves via the air flow: A feedback mechanism. *Boundary-Layer Meteorol.*, **83,** 99–116.

Large, W. G. and S. Pond, 1981: Open ocean momentum flux measurements in moderate to strong winds. *J. Phys. Oceanogr.*, **11,** 324–336.

Large, W. G. and S. Pond, 1982: Sensible and latent heat flux measurements over the ocean. *J. Phys. Oceanogr.*, **12,** 464–482.

Larson, T. R. and J. W. Wright, 1975: Wind-generated gravity–capillary waves: laboratory measurements of temporal growth rates using microwave backscatter. *J. Fluid Mech.*, **70,** 417–436.

Latham, J. and M. H. Smith, 1990: Effect on global warming of wind-dependent aerosol generation at the ocean surface. *Nature*, **347,** 372–373.

Launder, B. E. and S.-P. Li, 1994: On the elimination of wall-topography parameters from second-moment closure. *Phys. Fluids*, **6(2),** 999–1006.

Launder, B. E., G. J. Reece, and W. Rodi, 1975: Progress in the development of a Reynolds-stress turbulence closure. *J. Fluid Mech.*, **68,** 537–566.

Li, P. Y., D. Xu, and P. A. Taylor, 2000: Numerical modelling of turbulent airflow over water waves. *Boundary-Layer Meteorol.*, **95,** 397–425.

Lighthill, M. J., 1957: The fundamental solution for small steady three-dimensional disturbances to a two-dimensional parallel shear flow. *J. Fluid Mech.*, **3,** 1–13.

Ling, S. C. and T. W. Kao, 1976: Parameterization of the moisture and heat transfer process over the ocean under whitecap sea states. *J. Phys. Oceanogr.*, **6,** 306–315.

Liu, W. T., K. B. Katsaros, and J. A. Businger, 1979: Bulk parameterization of the air–sea exchange of heat and water vapor including the molecular constraints at the interface. *J. Atmos. Sci.*, **36,** 1722–1735.

Louis, J. F., 1979: A parametric model of vertical eddy fluxes in the atmosphere. *Boundary-Layer Meteorol.*, **17,** 187–202.

Lumley, J. L., 1978: Two-phase and non-Newtonian flows. In Bradshaw, P., editor, *Topics in applied physics*, pages 289–324. Vol. 12, Springer, New York.

Maat, N., C. Kraan, and W. A. Oost, 1991: The roughness of wind waves. *Boundary-Layer Meteorol.*, **54,** 89–103.

Makin, V. K., 1979: The wind field above waves. *Oceanology*, **19,** 127–130.

Makin, V. K., 1998: Air–sea exchange of heat in the presence of wind waves and spray. *J. Geophys. Res.*, **103,** 1137–1152.

Makin, V. K., 1999: A note on wind speed and sea state dependence of the heat exchange coefficient. *Boundary-Layer Meteorol.*, **91,** 127–134.

Makin, V. K. and V. N. Kudryavtsev, 1999: Coupled sea surface–atmosphere model. Part 1. Wind over waves coupling. *J. Geophys. Res.*, **104,** 7613–7623.

Makin, V. K., V. N. Kudryavtsev, and C. Mastenbroek, 1995: Drag of the sea surface. *Boundary-Layer Meteorol.*, **73,** 159–182.

Mastenbroek, C., 1996: *Wind–wave interaction*. PhD thesis, Delft Technical University, Delft, The Netherlands.

Mastenbroek, C., V. K. Makin, M. H. Garat, and J. P. Giovanangeli, 1996: Experimental evidence of the rapid distortion of turbulence in the air flow over water waves. *J. Fluid Mech.*, **318,** 273–302.

Meirink, J. F., V. N. Kudryavtsev, and V. K. Makin, 2002: Note on the growth rate of water waves propagating at an arbitrary angle to the wind. Submitted to *Boundary-Layer Meteorol.*

Meirink, J. F. and V. K. Makin, 2000: Modelling low-Reynolds-number effects in the turbulent air flow over water waves. *J. Fluid Mech.*, **415,** 155–174.

Meirink, J. F. and V. K. Makin, 2001: The impact of sea spray evaporation in a numerical weather prediction model. *J. Atmos. Sci.*, **58(23),** 3626–3638.

References

Mestayer, P. G., J. B. Edson, M. P. Rouault, C. W. Fairall, S. E. Larsen, G. De Leeuw, D. E. Spiel, J. DeCosmo, K. B. Katsaros, E.C. Monahan, and R. Schiestel, 1990: CLUSE simulations of the vapor flux modification by droplet evaporation. In Mestayer, P. G., E. C. Monahan, and P. A. Beetham, editors, *Modelling the fate and influence of marine spray, whitecap rep. 7*, pages 100–105. Mar. Sci. Institute, University of Connecticut.

Mestayer, P. G. and C. Lefauconnier, 1988: Spray droplet generation, transport and evaporation in a tunnel during the Humidity EXchange over the sea experiments In Simulation Tunnel. *J. Geophys. Res.*, **93,** 572–586.

Mestayer, P. G., A. M. J. Van Eijk, G. De Leeuw, and B. Tranchant, 1996: Numerical simulation of the dynamics of sea spray over the waves. *J. Geophys. Res.*, **101,** 20771–20797.

Miles, J. W., 1957: On the generation of surface waves by shear flow. *J. Fluid Mech.*, **3,** 185–204.

Miles, J. W., 1962: On the generation of surface waves by shear flow. Part 4. *J. Fluid Mech.*, **13,** 433–438.

Miller, M. J., A. C. M. Beljaars, and T. N. Palmer, 1992: The sensitivity of the ECMWF model to the parameterization of evaporation from the tropical oceans. *J. Climate*, **5,** 418–434.

Monahan, E. C., K. L. Davidson, and D. E. Spiel, 1982: Whitecap aerosol productivity deduced from simulation tank measurements. *J. Geophys. Res.*, **87,** 8898–8904.

Monahan, E. C. and I. G. O'Muircheartaigh, 1980: Optimal power-law description of oceanic whitecap coverage dependence on wind speed. *J. Phys. Oceanogr.*, **10,** 2094–2099.

Monahan, E. C., D. E. Spiel, and K. L. Davidson, 1986: A model of marine aerosol generation via whitecaps and wave disruption. In Monahan, E. C. and G. McNiocaill, editors, *Oceanic whitecaps*, pages 167–174. D. Reidel, Norwell, Mass.

Oost, W. A., C. M. J. Jacobs, and C. Van Oort, 2000: Stability effects on heat and moisture fluxes at sea. *Boundary-Layer Meteorol.*, **95,** 271–302.

Phillips, O. M., 1977: *The dynamics of the upper ocean*. Cambridge University Press.

Plant, W. J., 1982: A relationship between wind stress and wave slope. *J. Geophys. Res.*, **87(C3),** 1961–1967.

Preobrazhenskii, L. Y., 1973: Estimation of the content of spray-drops in the near-water layer of the atmosphere. *Fluid Mech.-Sov. Res.*, **2,** 95–100.

Pruppacher, H. R. and J. D. Klett, 1978: *Microphysics of clouds and precipitation.* D. Reidel, Norwell, Mass.

Resch, F. and G. Afeti, 1991: Film drop distributions from bubbles bursting in sea water. *J. Geophys. Res.*, **96,** 10681–10688.

Rouault, M. P., P. G. Mestayer, and R. Schiestel, 1991: A model of evaporating spray droplet dispersion. *J. Geophys. Res.*, **96,** 7181–7200.

Smith, M. H., P. M. Park, and I. E. Consterdine, 1993: Marine aerosol concentrations and estimated fluxes over the sea. *Quart. J. Roy. Meteor. Soc.*, **119,** 809–824.

Snyder, R. L., F. W. Dobson, J. A. Elliott, and R. B. Long, 1981: Array measurements of atmospheric pressure fluctuations above surface gravity waves. *J. Fluid Mech.*, **102,** 1–59.

Spiel, D. E., 1994: The sizes of the jet drops produced by air bubbles bursting on sea- and fresh-water surfaces. *Tellus*, **46B,** 325–338.

Stewart, R. H., 1970: Laboratory studies of the velocity field over deep-water waves. *J. Fluid Mech.*, **42,** 733–754.

Stramska, M., 1987: Vertical profiles of sea-salt aerosol in the atmospheric surface layer: a numerical model. *Acta Geophys. Polonica*, **35,** 87–100.

Sullivan, P. P., J. C. McWilliams, and C.-H. Moeng, 2000: Simulation of turbulent flow over idealized water waves. *J. Fluid Mech.*, **404,** 47–85.

Toba, Y., 1965: On the giant sea-salt particles in the atmosphere. II. Theory of the vertical distribution in the 10-m layer over the ocean. *Tellus*, **17,** 365–382.

Townsend, A. A., 1972: Flow in a deep turbulent boundary layer over a surface distorted by water waves. *J. Fluid Mech.*, **55,** 719–735.

Van Duin, C. A. and P. A. E. M. Janssen, 1992: An analytic model of the generation of surface gravity waves by turbulent air flow. *J. Fluid Mech.*, **236,** 197–215.

References

Van Eijk, A. M. J., B. S. Tranchant, and P. G. Mestayer, 2001: Seacluse: numerical simulation of evaporating sea spray droplets. *J. Geophys. Res.*, **106 (C2),** 2573–2588.

Van Gastel, K., P. A. E. M. Janssen, and G. J. Komen, 1985: On phase velocity and growth rate of wind-induced gravity–capillary waves. *J. Fluid Mech.*, **161,** 199–216.

Van Zetten, E., 2001: A study on the impact of sea spray evaporation in an atmospheric column model. Graduation thesis, Wageningen University, The Netherlands.

Wang, Y., J. D. Kepert, and G. J. Holland, 1999: The impact of sea spray evaporation on tropical cyclone intensification. In *Proceedings of the 23rd conference on hurricanes and tropical meteorology*, pages 26–29. Dallas, Amer. Meteor. Soc.

Wang, Y., J. D. Kepert, and G. J. Holland, 2001: The effect of sea spray evaporation on tropical cyclone boundary-layer structure and intensity. *Mon. Wea. Rev.*, **129(10),** 2481–2500.

Woetmann-Nielsen, N., 1998: Inclusion of free convection and a smooth sea surface in the parameterization of surface fluxes over sea. *Hirlam Newsletter*, **32,** 44–51. Available from: SMHI, SE–601 76 Norrköping, Sweden.

Wu, J., 1988: Variations of whitecap coverage with wind stress and water temperature. *J. Phys. Oceanogr.*, **18,** 1448–1453.

Wu, J., 1992: Bubble flux and marine aerosol spectra under various wind velocities. *J. Geophys. Res.*, **97,** 2327–2333.

Wu, J., 1993: Production of spume droplets by the wind tearing of wave crests: The search for quantification. *J. Geophys. Res.*, **98,** 18221–18227.

Yaglom, A. M., 1979: Similarity laws for constant-pressure and pressure-gradient turbulent wall flows. *Ann. Rev. Fluid Mech.*, **11,** 505–540.

Yelland, M., B. Moat, P. Taylor, R. Pascal, J. Hutchings, and V. Cornell, 1998: Wind stress measurements from the open ocean corrected for air-flow distortion by the ship. *J. Phys. Oceanogr.*, **28,** 1511–1526.

Zilker, D. P. and T. J. Hanratty, 1979: Influence of the amplitude of a solid wavy wall on a turbulent flow. Part 2. Separated flows. *J. Fluid Mech.*, **90,** 257–271.

Samenvatting

De rol van windgolven en zeespray
in lucht – zeewisselwerking

In de luchtlaag boven een wateroppervlak speelt zich een complex geheel van fysische processen af. Golven worden opgewekt en groeien door de wind. Als het hard waait en de golven te steil worden, breken ze. De hierdoor ingesloten lucht stijgt in de vorm van bellen weer naar de oppervlakte, wat resulteert in schuim. Als de bellen boven komen, lanceren ze waterdruppels (spray) de lucht in. Spray wordt ook gegenereerd als water rechtstreeks van golfkammen afwaait. In de lucht wisselen de druppels warmte en vocht uit met hun omgeving. De beweging van de druppels hangt af van het windveld en de turbulente fluctuaties daarin. Dit windveld wordt op zijn beurt beïnvloed door de golven.

In dit proefschrift worden deze processen gemodelleerd met als doel te onderzoeken welke rol golven en spray spelen in de uitwisseling van impuls en warmte tussen atmosfeer en zee. Kennis hierover is met name relevant voor weer- en klimaatmodellen, waarin die uitwisseling een belangrijke randvoorwaarde vormt.

Na een algemene inleiding in hoofdstuk 1 wordt in hoofdstuk 2 gekeken naar de turbulente stroming van lucht over golven. Hieraan is al veel onderzoek gedaan, vooral omdat de precieze structuur van die stroming bepaalt hoe snel de golven groeien. Gewoonlijk wordt aangenomen dat het effect van viscositeit vlakbij het wateroppervlak verwaarloosbaar is, ofwel dat het Reynoldsgetal hoog is. Voor korte golven is deze aanname echter niet terecht. Daarom hebben we de stroming gesimuleerd met een tweede-orde Reynoldsspanningsmodel (Mastenbroek et al. 1996) waarin viskeuze effecten in rekening zijn gebracht. De door dit model voorspelde windprofielen blijken redelijk goed overeen te komen met metingen in een golfgoot gedaan door Stewart (1970). Vervolgens is onderzocht hoe de groeisnelheid van de golven afhangt van het Reynoldsgetal. Voor lage Reynoldsgetallen blijkt de groei behoorlijk toe te nemen vergeleken met een model waarin viskeuze effecten niet worden meegenomen. Hiermee lijkt tenminste een deel van de tot dusverre bestaande

discrepantie tussen metingen en modellen verklaard te zijn.

Numerieke modellen, zoals hierboven gebruikt, verbruiken veel rekentijd. Voor toegepaste studies is het vaak nodig om snelle berekeningen te maken. Daarom wordt in hoofdstuk 3 een analytisch model van de stroming over golven beschreven. Het model is gebaseerd op schalingsprincipes van Belcher en Hunt (1993), die weergeven dat vanaf een bepaalde hoogte boven het wateroppervlak de turbulentie niet langer in evenwicht is met de lokale snelheidsgradiënt. Het model beschrijft dit verschijnsel op een sterk vereenvoudigde manier, maar levert toch vergelijkbare resultaten als het eerder beschreven numerieke model (zonder viskeuze effecten). Ook komt het berekende snelheidsveld goed overeen met metingen van Hsu en Hsu (1983). Voorts is gekeken naar golven die in een andere richting bewegen dan de wind. Het blijkt dat de component van de wind loodrecht op de golfrichting weinig invloed heeft op de golfgroei. De groeisnelheid van relatief langzame golven (in vergelijking met de windsnelheid) varieert dan als $\cos^2\theta$ (θ is de hoek tussen wind- en golfrichting), terwijl die van snellere golven sneller afneemt met de hoek.

In hoofdstuk 4 wordt de vereenvoudigde beschrijving van het windveld toegepast voor de bestudering van het transport van spraydruppels boven de golven. Hierbij wordt het spraymodel SeaCluse (Mestayer et al. 1996) gebruikt. De nieuwe beschrijving van de luchtstroming levert, vooral voor kleine druppels, een aanmerkelijk sneller met de hoogte afnemende evenwichtsconcentratie dan de oude formulering in SeaCluse. Helaas zijn er geen voldoende nauwkeurige metingen beschikbaar om dit te verifiëren. Hoofdstuk 4 bevat tevens een kort overzicht van de bestaande literatuur over zeespray. Dit overzicht betreft zowel experimentele als modelmatige studies en legt de nadruk op die aspecten die van belang zijn voor het effect van spray op de warmtebalans boven zee. Geconcludeerd wordt dat de voornaamste onzekerheid ligt in de bronfunctie, die aangeeft hoeveel spraydruppels van verschillende afmetingen, afhankelijk van de omstandigheden, worden gegenereerd.

Vervolgens wordt in hoofdstuk 5 een eenvoudig model gepresenteerd dat de verdamping van spray in de mariene oppervlaktelaag beschrijft. Het model, dat een uitbreiding is van dat van Makin (1998), is met name ontwikkeld om snelle schattingen van de effectieve bijdrage van spray aan de lucht–zee warmtefluxen te kunnen maken. Om rekentijd te besparen wordt een verticale evenwichtsverdeling van spray aangenomen, terwijl anderzijds de wisselwerking tussen de verdampende spray en het atmosferische temperatuur- en vochtveld wel gedetailleerd wordt beschreven. In eerste instantie worden berekeningen van de spray-geïnduceerde warmteflux zonder terugkoppeling uit de atmosfeer vergeleken met bestaande schattingen. Op basis hiervan lijkt spray vanaf windsnelheden van rond de 20 m s^{-1} tot een significante verhoging van de latente, respectievelijk verlaging van de sensibele warmteflux te leiden. Vervolgens wordt dieper ingegaan op de atmosferische terugkoppeling. Ge-

concludeerd wordt dat deze voor zeer uiteenlopende condities vrij constant en niet erg sterk is. De conclusie is echter gebaseerd op een bepaalde bronfunctie (Andreas 1998). Indien meer spray wordt gegenereerd, wordt de terugkoppeling ook snel belangrijker.

Het spraymodel kan gezien worden als een uitgebreide parameterisatie van de lucht–zee warmte- en impulsfluxen. Het kan worden toegepast in een numeriek weervoorspellingsmodel om zo de invloed van verdampende spray op de verwachtingen te onderzoeken, wat het uiteindelijke doel van dit proefschrift is. Hoofdstuk 6 beschrijft daartoe simulaties van twee zware stormen op gematigde breedte uitgevoerd met HiRLAM, het weervoorspellingsmodel dat op het KNMI wordt gebruikt voor het maken van de operationele verwachting. In deze studies is niet gebruik gemaakt van het model uit hoofdstuk 5 maar van de parameterisatie van Fairall et al. (1994), omdat deze nog veel minder rekentijd vergt en de verschillen ondergeschikt zijn aan de onzekerheid in de bronfunctie. Verdampende spray leidt tot een duidelijk koelere en vochtigere oppervlaktelaag en daarmee tot stabilisatie van de grenslaag. Indirecte gevolgen zijn een toename van de hoeveelheid neerslag en, daarmee samenhangend, vrijkomende latente warmte hoger in de atmosfeer. De tweede van de simulaties, die een zich snel uitdiepende depressie betreft, laat zien dat spray slechts een gering effect heeft op de ontwikkeling van de depressie. De waarschijnlijke reden hiervoor is dat de totale energieflux aan de oppervlakte nauwelijks wordt beïnvloed. Gezien het feit dat effecten van spray op gematigde breedten relatief klein zijn, en alleen aanwezig in extreem-weersituaties, kan voorzichtig gesteld worden dat zulke effecten voorlopig mogen worden verwaarloosd in weervoorspelmodellen.

Jan Fokke Meirink

Dankwoord

We zijn bijna aan het einde gekomen van dit proefschrift (hoewel waarschijnlijk velen het voorgaande grotendeels hebben overgeslagen) en ik maak graag nog even van de gelegenheid gebruik om wat mensen te bedanken die allemaal op hun eigen manier hebben bijgedragen aan de totstandkoming van dit boekje.

Allereerst wil ik mijn promotor Jurjen Battjes bedanken voor het in de gaten houden van de grote lijnen van het onderzoek. Het was nuttig dat je om verheldering en verantwoording vroeg als het project weer eens wat te ver van de oorspronkelijke doelstellingen dreigde af te dwalen.

Vladimir, als dagelijkse begeleider heb je een grote stempel op dit proefschrift gedrukt. Ik wil je bedanken voor je goede ideeën. Verder liet je me vooral erg vrij in mijn onderzoek. En als ik te lang dreigde door te ploeteren met details, spoorde je me aan om toch eens haast te maken met dat artikel. Een beetje druk in het deadline-loze (behalve die ene grote na vier jaar) bestaan van de oio kan geen kwaad!

Naast de golvenkant was er ook de spraykant van het project. Lex, hierin was jouw bijdrage onmisbaar. Hoewel het onderzoek soms een andere kant opging dan jij voor ogen had, hebben we altijd op een prettige manier samengewerkt. Ik heb genoten van je verhalen en ben je dankbaar voor de openhartige gesprekken over het leven in de wetenschap.

Next I would like to thank 'the other' Vladimir (Kudryavtsev). Your visits to KNMI were very inspiring for me. I admire the way you simply sit down and solve the problem. Chapter 3, which provides an important link in the thesis, would not have existed without you.

Eveline, ik ben erg blij dat je bij mij je afstudeeropdracht hebt gedaan en bewaar goede herinneringen aan onze regelmatige discussies over spray en andere zaken. Bert Holtslag wil ik bedanken voor de begeleiding vanuit Wageningen.

Verder hebben nog vele anderen geholpen bij het onderzoek. Ik wil hier noemen: Wim en Sander voor het leveren van commentaar op het concept van het spray-artikel, Gerard en Toon voor de HiRLAM ins en outs, Jeanette voor het op gezette tijden terug- en vooruitkijken en voor de nuttige tips, Gerrit Burgers en Gerbrand

Curriculum vitae

Jan Fokke Meirink werd geboren op 20 september 1974 in Hallum. Van 1986 tot en met 1992 doorliep hij het Stedelijk Gymnasium in Leeuwarden. Aansluitend volgde hij de studie Toegepaste Wiskunde aan de Universiteit Twente. Tijdens zijn stage deed hij onderzoek naar een model voor verbranding in gasturbines bij ABB in Baden, Zwitserland. Het afstudeeronderzoek werd uitgevoerd in opdracht van Gasunie en betrof de numerieke simulatie van de stroming door gaspijpen. Medio 1997 werd de studie met lof afgerond bij de vakgroep Mathematische Fysica. Van september 1997 tot en met september 2001 werkte hij in dienst van NWO als onderzoeker in opleiding bij de afdeling Applicaties en Modellen (tegenwoordig Research & Development Modellen) van het KNMI in De Bilt. De resultaten van het onderzoek staan beschreven in dit proefschrift. Sinds november 2001 werkt hij bij de afdeling Atmosferische Samenstelling van het KNMI aan de assimilatie van satellietmetingen van methaan in een atmosferisch chemie–transportmodel.

Epilogue

Once upon a time, when the dynamic effects of viscosity were still important and the threshold for the generation of spume droplets had not yet been reached, a small bubble was born in a tropical ocean.

The exotic bubble was in thermal equilibrium with its surroundings. Like an average child, it grew larger over time. But unfortunately, there was no stopping to the bubble's enormous growth rate, even though it was in the vicinity of a gigantic wave in a fully developed sea. Even the air flow could not stop the terrible disaster that was about to take place. The exotic bubble knew that there was only one person that could save him, Reynolds, but his moves were difficult to predict and even harder to be influenced. Then, just when the bubble was about to give up hope, the wind changed its angle, reducing the perturbation of the vertical velocity, caused by the presence of what appeared to be somewhat overwhelming. There, right before his eyes, came from the crude and turbulent sea, a huge roaring dinosaur, leaving the exotic bubble completely flabbergasted. The appearance of this highly unexpected creature caused an exchange of momentum. Wave-induced motions led to the breaking of the gigantic wave. With the breaking, sea spray droplets were ejected into the air. The exotic bubble was hit directly in the face and the unthinkable happened in a split second, although it appeared to last an eternity. The bursting bubble splashed apart, producing thousands of spray droplets, which were set loose into the open air...

Researchers over the world are now trying to capture what happened that day using spray models. However, the large number of assumptions clearly indicates that the mystery of the bursting bubble might never be uncovered.